Jean Hélder Marques Ribeiro

Analysis of Coherent Structures in Wall-Bounded Turbulent Flows Using Proper Orthogonal Decomposition

Análise de Estruturas Coerentes em Escoamentos Turbulentos com Presença de Paredes Através de Decomposição Ortogonal Própria

CAMPINAS
2017

Jean Hélder Marques Ribeiro

Analysis of Coherent Structures in Wall-Bounded Turbulent Flows Using Proper Orthogonal Decomposition

Análise de Estruturas Coerentes em Escoamentos Turbulentos com Presença de Paredes Através de Decomposição Ortogonal Própria

Dissertation presented to the School of Mechanical Engineering of the University of Campinas in partial fulfillment of the requirements for the degree of Master in Mechanical Engineering, in the area of Thermal and Fluids.

Dissertação apresentada à Faculdade de Engenharia Mecânica da Universidade Estadual de Campinas em preenchimento parcial dos requisitos para obtenção do título de Mestre em Engenharia Mecânica, na área de Térmica e Fluidos.

Orientador: William Roberto Wolf

Este exemplar corresponde à versão final da dissertação defendida pelo aluno Jean Hélder Marques Ribeiro, e orientada pelo Prof. Dr. William Roberto Wolf.

Assinatura do Orientador

_____

Campinas

2017

Agência(s) de fomento e nº(s) de processo(s): CAPES, 33003017
ORCID: http://orcid.org/0000-0002-8613-9593

Ficha catalográfica
Universidade Estadual de Campinas
Biblioteca da Área de Engenharia e Arquitetura
Luciana Pietrosanto Milla - CRB 8/8129

R354a

Ribeiro, Jean Hélder Marques, 1990-
Analysis of coherent structures in wall-bounded turbulent flows using proper orthogonal decomposition / Jean Hélder Marques Ribeiro. – Campinas, SP : [s.n.], 2017.

Orientador: William Roberto Wolf.
Dissertação (mestrado) – Universidade Estadual de Campinas, Faculdade de Engenharia Mecânica.

1. Turbulência. 2. Aerodinâmica. I. Wolf, William Roberto,1980-. II. Universidade Estadual de Campinas. Faculdade de Engenharia Mecânica. III. Título.

Informações para Biblioteca Digital

Título em outro idioma: Análise de estruturas coerentes em escoamentos turbulentos com presença de paredes através de decomposição ortogonal própria
Palavras-chave em inglês:
Turbulence
Aerodynamics
Área de concentração: Térmica e Fluídos
Titulação: Mestre em Engenharia Mecânica
Banca examinadora:
William Roberto Wolf [Orientador]
Marcelo Souza de Castro
Elmer Mateus Gennaro
Data de defesa: 31-03-2017
Programa de Pós-Graduação: Engenharia Mecânica

UNIVERSIDADE ESTADUAL DE CAMPINAS

FACULDADE DE ENGENHARIA MECÂNICA

COMISSÃO DE PÓS-GRADUAÇÃO EM ENGENHARIA MECÂNICA

DEPARTAMENTO DE TERMICA E FLUIDOS

DISSERTAÇÃO DE MESTRADO ACADÊMICO

Análise de Estruturas Coerentes em Escoamentos Turbulentos com Presença de Paredes Através de Decomposição Ortogonal Própria

Autor: Jean Hélder Marques Ribeiro

Orientador: William Roberto Wolf

A Banca Examinadora composta pelos membros abaixo aprovou esta dissertação:

Prof. Dr. William Roberto Wolf
Instituição UNICAMP

Prof. Dr. Elmer Mateus Gennaro
Instituição UNESP

Prof. Dr. Marcelo Souza de Castro
Instituição UNICAMP

A Ata da defesa com as respectivas assinaturas dos membros encontra-se no processo de vida acadêmica do aluno.

Campinas, 08 de Julho de 2016.

Acknowledgments

First and foremost, I want to express my deep gratitude and appreciation to my advisor, Prof. William Wolf, who taught me and made possible a considerable professional and personal growth in my life. His mentorship throughout the past two years has been paramount to the progress of this work and also in my own research maturity. For everything you have done for me, William, I thank you very much! Also, I am thankful to MSc. Luiz Augusto Schiavo, who has almost been a second advisor to me. From him I have learned from basic Fortran programming, Linux, to mathematics and nonlinear flows. Without our turbulence talks and his continuously encouragement, I would have never been able to finish this work.

I am thankful to Prof. Marcelo Castro and Prof. Elmer Gennaro (UNESP), who served in my dissertation committee. I am also grateful to Prof. José Roberto de França Arruda, Prof. Erik Franklin and Prof. Rogério Gonçalves from whom I had the opportunity of leaning in the graduate classes I attended during my Master's Degree. In addition, I want to express my sincere thanks and appreciation to Prof. André Cavalieri (ITA), from whom I have learned aeroacoustics and turbulence.

I have been very fortunate to work with the brilliant engineers and members of CFD Lab. To Tulio, thank you very much for everything I have learned with you, you are an amazing engineer and a great friend, it has been an honor to work with you. I am very thankful to get to know Bruno Backes, who is an inspiring engineer and person, I am specially thankful to him for finding me a good place to live in Campinas. To Renato Miotto, I want to thank you for the partnership and the many laughs we shared, thanks for the amazing catchphrase *Tudo cagado*. To Cristiano Pimenta, the father of the year, I want to express my good thoughts to your family and thank you for the amazing candies you and your wife brought to us. To Paulo Azevedo, the statistician, thank you for everything you taught me on Linux and Fortran, you are a great guy and it was very good working with you in the lab. To Walter Ramirez, thank you so much for the laughing, the many advices and the Spanish lessons, I miss you very much since you went away to Maryland, USA. To the new guys, Brener Lélis and Lucas Mascagni, thank you very much for the opportunity of working, playing soccer and sharing knowledge with you guys.

I want to thank CAPES and CNPq for providing fundings for my Master's Degree education. Also, I must thank to Embraer, for the funding the beginning of my Master's Degree and providing support for conference publishing and presenting. I must thank

to FAPESP for all support to the William Wolf Group this years. I am indebted to CENAPAD-SP, where the many computations from this work were run. The CENAPAD support was essential to the development of this work and many others from the group, I mus thank specially to Carlos Rebollo for the help in parallel programming.

I am indebted to Godzilla, Sauron and ICE. I know that people look at you and see only HD, RAM memory, processors and computer stuff, but I can see the heart and the feelings deep inside you. Sorry for pushing you guys so hard, you have been of utmost importance to me and to this work.

It is important to acknowlege my friends from Mech. Eng. Faculty, Nathan Maidana, Gabriel Meletti, Ednir Nigra, Marcão *The Myth*, Gabriel Oliveira, Saon Vieira, Eduardo Lima and Bruno Chimetta for their friendship and beers we shared. Thank you guys for the amazing stories, jokes and laughs, which I will always remember. Hope we can keep contact over the years to come.

Specially, I want to thank my graduate friends from other departments, Alfredo, Gil, José, Yuri and Darla, and from Electrical Eng. Faculty, Maria Luisa, Marcelo, Luís Fernando, Nereu, Diego and many others I have met because of you guys for making the many difficulties I had during these years so much easier to deal with. Also, I know the songs in my playlist will be always playing during the traditional weekend barbecues.

I want to thank the "21h o'clock" Thursday Soccer guys whom I know mainly by nicknames, Alface, Gauchão, Zola, Johnny, Borto, *nice guy* Natan, Neill, Mentira, Alcimar, for all the interaction and laughing in the past year.

As far as my personal beliefs are concerned, I must thank God for keeping me straight during the hard times in my Master's Degree, without Him, nothing in my life would be possible.

Last but not least, I want to thank my parents and my beloved girlfriend, but I will not force them to read this is a foreign language, so I ask for permission to write this in Portuguese: *Pai, muito obrigado por acreditar sempre em mim e me dar forças durante esses anos que estive em Campinas. Mãe, sem seu amor e carinho nada disso seria possível, me desculpe por ter estado longe, mas você estava sempre em meu coração. Obrigado a vocês dois por me mostrarem o real significado de amor em família. Emille, sei que foram anos difíceis para nós vivendo distantes um do outro, mas quero que saiba que em todo este tempo tive você em meu coração, te amo e sempre te amarei. Dedico esta dissertação a vocês, com todo meu amor.*

"Uuuuuhhhur Ahhhhhrrrrr Uuuuhhhrr Ahhhrrrgh"
Chewbacca (Star Wars, 1977)

Abstract

Proper orthogonal decomposition is employed for identifying coherent structures in wall-bounded turbulent flows. A large eddy simulation database of turbulent flows past a NACA0012 airfoil at Mach numbers $M_\infty = 0.115$ and 0.4, at 0 and 5 degs. angle of attack for Reynolds number $Re_c = 408000$ is employed in the present investigations. Analyses of different POD techniques are presented using the snapshot method, the spectral POD method (SPOD) and a Fourier-POD implementation combined with the SPOD. The latter technique is viable once the present turbulent flow has a homogeneous direction along the airfoil span. An assessment of different vector norms and filter functions employed in the correlation matrix is presented. The spectral POD technique is applied assuming periodic and non-periodic temporal signals. Results show that the SPOD method provides a better coupling of the modes, redistributing the energy among the POD eigenvalues and leading to an improved identification of coherent structures. The application of a Gaussian filter allows an enhanced control in the response of the SPOD when compared to a square-box filter. The assumption of periodic temporal signals in the construction of the correlation matrix provides further improvement in the coupling of POD modes and cleans their spectral content. Pressure based on kinetic energy norms are used and, for both norms, the first pair of POD modes are related to coherent structures responsible for airfoil tonal noise generation. However, the kinetic energy norm tends to reconstruct low-frequency structures in the flow field for higher POD modes while the pressure norm reconstructs high-frequency structures. The combination of Fourier decomposition with the SPOD method allows a clear identification of coherent structures for the specific Fourier modes along the airfoil span. The spectral content of the POD modes can be decoupled to each spanwise Fourier mode. For the coherent structures identified in the numerical database, the interaction between modes at different ranges of frequencies is identified. Coherent structures aligned with the airfoil span are shown to be related to tonal noise peaks, making it possible to identify the main aeroacoustic sources. Coherent structures aligned with the streamwise direction and diagonally aligned with the span are formed for all flow configurations due to the curvature of the airfoil and the adverse pressure gradient after the forced turbulence transition. For flows at 5 degs. angle of attack, only diagonal structures at high frequencies are present. At 0 degs. angle of attack, diagonal coherent structures at low frequencies are present affected by the weaker adverse pressure gradient.

Keywords: POD, LES, Turbulence, Coherent Structures, Airfoil Flow

Resumo

Decomposição Ortogonal Própria é aplicada para identificar estruturas coerentes em escoamentos turbulentos sobre um perfil NACA0012. A base de dados numérica é formada por escoamentos com números de Mach $M_\infty = 0.115$ e 0.4, e 0 e 5 graus de ângulo de ataque, para um número de Reynolds $Re_c = 408000$. Análises de diferentes técnicas de POD são apresentadas usando o método de *snapshots*, o método de POD espectral (SPOD) e a combinação Fourier-POD com o SPOD. Esta última análise é possível devido à direção homogênea na envergadura através da condição de contorno numérica de periodicidade do escoamento. Uma avaliação de diferentes normas vetoriais e funções filtro na matriz de correlação é realizada neste trabalho. A técnica de SPOD é aplicada assumindo sinais temporais periódicos e não-periódicos. Resultados mostram que o SPOD melhora o acoplamento dos modos, redistribuindo a energia ao longo dos autovalores e levando à uma melhor identificação das estruturas coerentes. Aplicação de um filtro gaussiano permite um melhor controle na resposta do SPOD comparado ao filtro quadrado. A hipótese de sinais temporais periódicos na matriz de correlação melhora o acoplamento dos modos e limpa seu conteúdo espectral. Normas de pressão e energia cinética são usadas neste trabalho e, para ambas, o primeiro par de modos é relacionado à estruturas coerentes responsáveis pela geração de ruído tonal. Entretanto, a norma de energia cinética tende a capturar estruturas de baixa frequência nos modos subsequentes, enquanto a norma de pressão captura estruturas de alta frequência. A combinação Fourier-POD permite uma melhor identificação das estruturas coerentes para cada modo de Fourier ao longo da envergadura. O conteúdo espectral dos modos de POD pode ser desacoplado para cada modo de Fourier. Foi possível identificar a interação entre modos em diferentes frequências nos dados numéricos. Estruturas alinhadas com a envergadura são relacionados ao ruído tonal na análise acústica, identificando as fontes sonoras. Estruturas alinhadas com o escoamento, ou na diagonal, são formadas em todas as análises devido à curvatura do perfil e ao gradiente de pressão adverso após a transição turbulenta. Para os casos com 5 graus de ângulo de ataque, apenas estruturas diagonais de alta frequência estão presentes. Afetados pelo gradiente de pressão mais fraco, estruturas diagonais de baixa frequẽncia estão presentes no perfil para 0 graus de ângulo de ataque.

Palavras-chave: POD, LES, Turbulência, Estruturas Coerentes, Escoamentos em Aerofólios

List of Figures

List of Acronyms

Latin Letters

a	POD mode temporal amplitudes
c	airfoil chord
kc	wavenumber based on airfoil chord c
C	correlation matrix
$\bar{C}$	filtered correlation matrix
E	total energy
F_i	dipole sources
G	Green's function
$H_0^{(2)}$	Heaviside function of 2nd kind and order 0
N_f	spectral filtering window size
M_∞	freestream Mach number
p	pressure
q	quantities vector
Q	monopole sources
Re	Reynolds number
St	Strouhal number
Pr	Prandtl number
t	dimensionless time
T	temperature
T_{ij}	quadrupole sources
$\mathbf{Q}$	vector numerical data matrix
$\mathbf{U}$	spatial eigenfunctions matrix
$\mathbf{V}^*$	Hermitian temporal dynamics matrix
u	velocity component along x-axis
v	velocity component along y-axis
w	velocity component along z-axis
x	x-coordinate of the three-dimensional domain
y	y-coordinate of the three-dimensional domain
z	z-coordinate of the three-dimensional domain

Greek Letters

α	angulo de incidência
Δ	parameter variation
Σ	singular values matrix
τ_{ij}	viscous stress
γ	specific heats ratio
λ	singular value (POD mode)
μ	dynamic viscosity
ν	kinematic viscosity
π	circumference over diameter ratio
ρ	density
ϕ	spatial eigenfunction

Superindices

$\hat{.}$	Fourier transformed variable
$.^n$	spanwise Fourier mode number
$.'$	fluctuation quantities

Subindices

i	dummy index
j	dummy index
k	dummy index
c	chord-based values
∞	free-stream property
λ_n	POD mode number

Abbreviations

1D	one-dimensional
2D	two-dimensional
3D	three-dimensional
AoA	angle of attack
CFD	computational fluid dynamics
CFL	Courant–Friedrichs–Lewy condition
CGNS	CFD general notation system
DFT	Discrete Fourier Transform
DNS	Direct Numerical Simulation
DMD	Dynamic Mode Decomposition
ERA	Eigensystem Realization Algorithm
FWH	Ffowcs-Williams and Hawkings Analogy
FFT	Fast Fourier Transform
k-3D	kinetic energy based norm on full 3D domain
k-wake	kinetic energy based norm on vortex wake domain
p-3D	pressure based norm on full 3D domain
p-acoustic	pressure based norm on acoustic region
LDA	Laser Doppler Anemometry
LES	Large Eddy Simulation
LIM	Linear Inverse Method
PIV	Particle Image Velocimetry
POD	Proper Orthogonal Decomposition
RAM	Random Access Memory
RMS	root-mean-square
ROM	Reduced-Order Modelling
SPL	Sound Pressure Level
SPOD	Spectral Proper Orthogonal Decomposition
SVD	Singular Value Decomposition

Other notations

$Real$	Real part of a number
$Imag$	Imaginary part of a number

Contents

1 Introduction

1.1 Airfoil Noise

Aerodynamic lifting devices are known for its intense noise scattering due to broadband surface pressure fluctuations from turbulent boundary layers (Wang and Moin, 2000). This problem is encountered in a wide range of engineering applications where low noise emissions from turbulence-solid body interaction is desired. These applications include rotor blades, wind and gas turbines, pumps, high-lift devices, fans and wings. The physics of noise scattering is associated with surface pressure fluctuations from unsteady aerodynamic loads generated as air flows past a solid body. In the case of blunt bodies immersed in low Mach number turbulent flows, the far-field acoustic power is proportional to the sixth power of the Mach number (Curle, 1955). However, when a sharp trailing edge is immersed in a low-speed turbulent flow, the far-field acoustic power is proportional to the fifth power of the Mach number (Ffowcs-Williams and Hall, 1970).

Brooks, Pope and Marcolini (1989) performed a series of experiments which were used to identify the main sources of airfoil noise, namely turbulent and laminar boundary layer noise, separation-stall noise, tip vortex noise and trailing edge bluntness noise. Each of these sources appear for different flow conditions and all the mechanisms described are related to the so-called airfoil self-noise generation. Stall noise may occur for some flow conditions in wind turbine blades and tip vortex noise is characteristic of flap side edges which are deployed when aircraft are landing.

Turbulent boundary layer noise is the most common airfoil self-noise generation mechanism since most flows of engineering applications occur in turbulent conditions. On the other hand, laminar boundary layer noise is present in airfoil shapes of reduced characteristic lengths, such as in automotive cross-bars installed in the top roof of cars, as in the work of Massaroti and Wolf (2016). Automotive cross-bars employ airfoil profiles with blunt trailing edges and, therefore, trailing edge bluntness noise is also present in these configurations. While turbulent boundary layers present a broadband far-field noise spectrum, laminar boundary layers and blunt trailing edges usually present narrowband tones from coherent sources such as vortex-shedding or Tollmien-Schlichting waves. In this context, coherent structures are more effective sources of noise generation. While small turbulent scales along boundary layers behave as incoherent sources with phase-destructive interference, coherent turbulent structures

present a constructive behavior, generating noise more efficiently.

Lockard and Lilley (2004) identified the trailing edge noise as the main aeroacoustic source in airfoil noise problems. However, leading edge noise from a turbulent flow impinging on an airfoil is also a topic of interest for aeroacousticians, as shown by Miotto *et. al* (2016). In order to correctly analyze and identify aeroacoustic sources, as well as to understand the physics involved in the turbulent structures which are responsible for the noise generation, well resolved turbulence data is needed. Several experimental, numerical and analytical approaches can be employed to study the physics of turbulence and its subsequent noise generation. Among the experimental techniques which can be applied for measuring velocity fields, one can cite particle image velocimetry, PIV, and laser Doppler anemometry, LDA. Surface and far-field pressure fluctuations can be obtained by pressure transducers and microphones, respectively. Although all these experimental techniques may be used for the analysis of turbulent flows and noise generation, one should mention that experimental campaigns in aeroacoustic wind tunnels have high costs and, therefore, are not used in conceptual design stages. Analytical models have been developed along the past decades to predict the noise from airfoils (Brooks, Pope and Marcolini, 1989). However, these models are not general and need to be tuned to specific geometries and flow conditions for accurate results.

Summarizing, as the computational resources are continuously being enhanced, the frontier of what is feasible in high-fidelity CFD has been expanded and numerical simulations have become a viable approach for the investigation of turbulent flows (Lele and Nichols, 2014; Kocheemoolayil and Lele, 2014; Wolf *et. al*, 2014; Kocheemoolayil and Lele, 2016). However, in order to obtain accurate results, low-dissipation and low-dispersion numerical methods need to be employed. Techniques such as direct numerical simulation, DNS, and large eddy simulation, LES, are well-suited for the calculation of unsteady flows.

1.2 Turbulence Analysis

Although numerical simulations may provide three-dimensional (3D) turbulent velocity fields, analyzing coherent structures in well-resolved turbulence is still not a simple task and it represents, indeed, and "old dream" for physicists and engineers. The earliest works on flow visualization were performed by Brown and Roshko (1974), whose shadowgraphs revealed convection at almost constant speed of an organized vortex-like quasi-2D coherent structure. In 1981, Cantwell reviewed the research on turbulent flows, discussing possible ways to investigate the dynamics of organized structures. The definition of coherent structures as fluid mass with instantaneously correlated vorticity

over space was given by the work of Hussain (1980, 1983 and 1986), who also characterized vorticity as a characteristic measure of coherent structures. Hussain also proposed a decomposition of the fluid flow into mean flow, coherent and incoherent turbulence for a better understanding of the origins and dynamics of the problem.

The first proposal for investigating coherent structures without the dependence of a conditional criteria was proposed by John Lumley (1967 and 1970) who employed the Proper Orthogonal Decomposition, POD, technique. Briefly, POD uses second-order statistics to extract large energy-containing structures from turbulence. The mathematical basis of POD will be discussed further in Section 3.1.

Despite of its early introduction in the field of fluid mechanics, POD has only gained attention recently, especially for its use in reduced-order models (ROM) using the Galerkin Projection of the POD modes to turn partial differential Navier-Stokes equations into a set of ordinary differential equations. Aubry *et. al* (1988) employed this technique for the study of incompressible flows while Rowley (2002) performed POD on numerical data of flow past a two-dimensional (2D) open cavity in order to expand the Galerkin Projection to model compressible flows at moderate Mach numbers. The results obtained by Rowley showed better long-time behavior when applying vector-valued POD modes than using scalar-valued ones. Also, Nagarajan *et. al* (2009) studied the compressible cavity problem using POD-Galerkin for flow control.

In its use for flow analysis, many researchers found interesting results due to the capability of POD to extract the most energetic coherent structures in turbulent flowfields. Podvin (2009), Podvin *et. al* (2010) and Podvin and Sergent (2012) made use of POD for investigating the dynamics of turbulence in the near-wall region of well-resolved turbulence data. Liberzon *et. al* (2005) performed important studies in channel flow using POD to characterize the flow and identify large eddies in 3D numerical data using the linear combination of POD modes to understand the vorticity fields. Gurka *et. al* (2006) used POD in vorticity fields for spatial characterization of large scale coherent structures present in a channel flow from experimental PIV results. Diamessis *et. al* (2010) studied slices from numerical simulation data of a stratified fluid flow using POD for identifying the eddies present in the flow. Important conclusions on the 2D and 3D coherent structures were drawn from the work of Liberzon *et. al* (2011), presenting the main differences between the application of POD in channel flow analyzing experimental data from PIV slices and combining multiple slices for the analysis of the entire fluid flow region. Taira (2011) analyzed the results obtained for numerical simulations of high angle of attack airfoils obtained by Taira and Colonius (2009) and Colonius and Taira (2008). Even for laminar flows, as in the work of Backes (2016), the coherent structures can be important on the flow analysis, so POD modes were used to characterize the spatial eddies

and the energy associated to them in a canonical rod-airfoil configuration in tandem. In acoustics, the work of Freund and Colonius (2009) is a reference for understanding how POD can be used to investigate the dynamics of coherent structures in homogeneous jet flows including the understanding of jet noise sources and the application of POD modes for acoustic propagation.

POD ranks modes ordered by the amount of energy, corresponding to large scale observable states. Although the observability is important, it does not mean that the most observable states are the ones with relative dynamical importance to the system. This drawback must be addressed by Dynamic Mode Decomposition, DMD, and Balanced POD, BPOD. The standard method have been extended to address some of the drawbacks of the method, some approaches such as the Split POD (Camphouse *et. al*, 2008), Temporal POD (Gordeyev and Thomas, 2013), Joint POD (Gordeyev *et. al*, 2014) and the promising Spectral POD (Sieber *et. al*, 2016) which performs a transition between POD and DFT modes and will be treated further in this work (Section 3.6). Good results have been obtained for DMD and BPOD, so they will be briefly discussed here.

In the past few years, DMD has gained attention due to its capability of capturing spatial and temporal instabilities. Whereas POD is based on the correlation matrix gathered from the snapshots, the DMD extracts from the snapshots a low-dimensional evolution matrix. The technique was first proposed by Schmid and Sesterhenn (2008), as an Arnoldi-type method for the decomposition of fluid flows. After that, Schmid *et. al* (2009) compared DMD modes and POD modes showing that both techniques capture bifurcation points. While the POD modes had the capability of concentrating the most energetic coherent structures, DMD gathered the less-energetic, but more unstable modes, which could be useful for instability analysis and flow control as instabilities have dynamic behavior commonly associated to modes with small energy. In the same year, Rowley *et. al* (2009) realized that the Arnoldi-type algorithm proposed by Schmid and Sesterhenn is able to compute Koopman modes, applying its spectral analysis to jet crossflow data. As stated by Rowley *et. al* (2009), the Koopman modes have a single temporal frequency information and growth rate and can be analyzed as a nonlinear generalization of global eigenmodes of a linearized system. In the work of Schmid (2010), the full information in DMD implementation was gathered with its mathematical basis and made its use well known for different applications.

Tu *et. al* (2011) used the Koopman modes to study controlled flows. Later, Tu *et. al* (2014) expanded the use of DMD to other applications, establishing the connections between DMD and Koopman modes and other decomposition techniques, such as eigensystem realization algorithm (ERA) and linear inverse method (LIM). The spectral content of the Koopman operator was analyzed among with other decomposition

techniques in Mezić (2013), also based in his previous work analysis (Mezić (2005)). Recently, Rowley and Dawson (2017) reviewed the recent evolution in model reduction for analysis and control of fluid flows, demonstrating the recent advances in modal analysis, including the recent implementations, including the extended DMD (EDMD).

DMD has been important in flow control specially for its time frequency information and the ability for dynamic analysis of instabilities. Among other modal decompositions, *e. g.* POD, DMD is promising for been used for model reduction of fluid flows. Due to the intrinsic problems in reduced-order modeling for nonlinear systems, further improvements in both techniques are been proposed.

In a different approach, balanced truncation can be extended to POD resulting in the Balanced POD (Rowley, 2005). BPOD was derived from the standard POD snapshot method to balance the observability and controllability capabilities of modal decomposition. As stated before, POD modes gather the states with large scale motion that contain the most energetic structures of the flow. However, the energy-ranked POD modes may not correspond to their dynamical importance. BPOD determines the coordinate system containing high observability, related to the most energetic large scale modes that present the most observable outputs in the system, and also high controllability, related to states that can be easily excited by control inputs.

The method has been mainly used for linear systems (Ilak and Rowley, 2008; Ahuja and Rowley, 2010). The method generates a set of balancing and adjoint modes, where the large scale motion can be analyzed in observability and controllability, which makes this method being of utmost importance for reduced-order modeling and flow control. Due to the need of adjoint modes, the used of the method for experimental results is limited. This issue have been addressed by the use of the eigensystem realization algorithm, ERA (Juang and Pappa, 1985). One of the drawbacks of the method is the need of balancing and adjoint modes based on linear dynamics. Nonlinearities extensions have been proposed, specially by the works of Lall *et. al* (2002) and Ilak *et. al* (2010).

Modal decomposition is of paramount importance for turbulence analysis of well resolved turbulence data and, as computational resources are continuously increasing, pushing the barriers for feasibility in numerical analysis, the use of these challenging eigenvalue problems will be even more necessary (Rowley and Dawson (2017)).

1.3 Overview and Motivation

Recently, Wolf *et. al* (2012 and 2013) performed several large eddy simulations of compressible flows past a NACA0012 airfoil. These authors showed that, for some of the flow configurations analyzed, a narrowband tone could dominate the far-field noise.

Among the flow conditions analyzed, they presented results showing a dominant acoustic tone for a NACA0012 airfoil at 5 degs. angle of attack (AoA). In this case, a moderate Reynolds number - low Mach number flow configuration was studied and results were compared to experimental data from Brooks *et. al* (1989). In order to represent the experiments, the suction side boundary layer was tripped using suction and blowing and the pressure side boundary layer developed under a favorable pressure gradient, being laminar up to the trailing edge. The tonal noise in this case was said to be related to the presence of large energy-containing elongated 2D coherent structures aligned in the spanwise direction. However, due to the turbulent boundary layer developing along the tripped suction side of the airfoil, it was still difficult to identify the presence of coherent structures. In this sense, POD will be used in the present work for decomposing the flow field and identifying the coherent structures which act as efficient aeroacoustic sources in the current turbulent flow past a NACA0012 airfoil. Along this dissertation, POD will also be employed to analyze the presence of coherent structures in other flow conditions past airfoils. Furthermore, an analysis of different POD techniques will be investigated, implemented and applied to perform the present studies and, finally, results will be discussed.

1.4 Objectives

The main goal of the present work is to develop knowledge beyond the simple application of the POD technique for turbulent flows. In this sense, one of the objectives of the present work is to analyze the main characteristics of different POD reconstructions, for instance, the snapshot method and the spectral proper orthogonal decomposition, SPOD, recently proposed. Moreover, Fourier POD reconstructions are also employed combined with the previous techniques. Hence, this work focuses on explaining features and implementation details of different POD techniques, providing insights for different applications.

In parallel, the present work is committed to the analysis of coherent structures in several airfoil flow configurations, including compressibility and angle of incidence effects. For the former, low and moderate Mach number flows are investigated and, for the latter, angles of attack of 0 and 5 degs. are considered. All flows studied here are obtained for a moderate Reynolds number. Global modes are the solution for modal analysis of turbulent flows, due to the nonlinear physics inherent of turbulence. Analyzing the physics of turbulence in global modes is still a hard task and a deep analysis on the behavior of such modes is important to provide the basis for more complex solutions for engineering applications. The fundamental knowledge on the physics of turbulence

presented in high-resolution simulation data, as the ones that will be used in this work, is paramount for aeronautical, automotive and industrial applications in a wide variety of projects, from wind turbines, to commercial and military airplanes.

1.5 Main Accomplishments

The present work provides several contributions to the use of POD modes in order to analyze turbulence in high-resolution numerical data. The insights here provided can be extended to different flow configurations and experimental data analysis. A thorough investigation is performed to analyze specific features of POD analysis to generate global modes for turbulent flows. One important feature that is highly used in literature is the coupling between Fourier decomposition and POD when the flow contains a homogeneous direction. However, in industrial applications and fully three-dimensional flows, a homogeneous flow direction is not always possible. The continuous improvement of computer processing will expand the barrier of what is computationally feasible in computational fluid dynamics for well-resolved turbulence data. So, more complex geometries will generate complex numerical data for highly nonlinear flows. The present work shows results for a general implementation of POD not considering the symmetry in the span direction. When the homogeneous direction is considered in POD analysis, the Fourier POD coupling already helps in decomposing the flow and analyzing specific components of the physics. However, when no homogeneous direction is present, this work shows how to improve the POD results and enhance the capabilities for capturing useful physics from the turbulence data. In this sense, the spectral POD technique is employed and analyzed considering different implementation approaches. Even when the spanwise symmetry is present, the Fourier-POD coupling can be enhanced by the SPOD technique in order to better capture coherent structures in the flow and this is also shown in this work results.

Besides the POD enhancements, the present work provides useful information about the coherent structures developing over the airfoil surface along the boundary layer and the vortex wake for different flow configurations. The results show a combination of coherent structures aligned with the streamwise direction and also diagonally aligned with the spanwise direction. These coherent structures appear at specific ranges of frequencies related to the intrinsic physics of the turbulent flow and they are associated to the aeroacoustic sources from the fluid flow that are “hidden” inside the chaotic turbulent field. When the adverse pressure gradient is stronger, at 5 degs. angle of attack, the coherent structures diagonally aligned are thinner and oscillate at higher frequencies. However, when the adverse pressure gradient is weaker, for 0 degs. angle of attack, the

diagonal coherent structures are larger, as the fluctuations are less intensive near the trailing edge.

Summarizing, the main contributions of this work include:

- the development and implementation of a fully 3D POD numerical tool which employs the snapshot method, the spectral POD method and a combination of Fourier decomposition with the SPOD method;
- the analysis of different vectorial norms for the reconstruction of the correlation matrix in the snapshot method, the SPOD method and the Fourier-SPOD method;
- the investigation of methodologies for the reconstruction of the correlation matrix in the SPOD method including different filtering procedures to the temporal signal including the role of the periodicity;
- the analysis of coherent structures in wall bounded turbulent flows developing along a NACA0012 airfoil at different flow configurations.

2 Fluid Dynamics Formulations

2.1 Governing Equations

Turbulent flows at low and moderate Mach numbers can be modelled in Cartesian coordinates by the Navier-Stokes equations (using Einstein's Notation) as follows:

$$\frac{\partial \rho}{\partial t} + \frac{\partial (\rho u_i)}{\partial x_i} = 0, \tag{2.1}$$

$$\frac{\partial (\rho u_i)}{\partial t} + \frac{\partial (\rho u_i u_j + g^{ij} p - \tau_{ij})}{\partial x_j} = 0, \tag{2.2}$$

$$\frac{\partial E}{\partial t} + \frac{\partial [(E+p)u_j - \tau_{ij} g_{ik} u_k + q_j]}{\partial x_j} = 0, \tag{2.3}$$

where u_i, ρ and p are instantaneous velocity components, density and pressure, respectively. The total energy, E, the viscous stress tensor, τ_{ij}, and the heat flux, q_j, are given by

$$E = \frac{p}{\gamma - 1} + \frac{1}{2} \rho g_{ij} u_i u_j, \tag{2.4}$$

$$\tau_{ij} = \frac{\mu}{Re} \left(g^{jk} \frac{\partial u_i}{\partial x_k} + g^{ik} \frac{\partial u_j}{\partial x_k} - \frac{2}{3} g^{ij} \frac{\partial u_k}{\partial x_k} \right), \tag{2.5}$$

$$q_j = -\frac{\mu}{RePr} g^{ij} \frac{\partial T}{\partial x_i}. \tag{2.6}$$

The set of equations is closed by the equation of state, assuming the medium as a perfect gas:

$$p = \frac{\gamma - 1}{\gamma} \rho T. \tag{2.7}$$

In the equations above, g_{ij} and g^{ij} are the covariant and contravariant metric tensors, respectively. T is the temperature, γ is the ratio of specific heats, Re is the Reynolds number defined as $Re = \rho_\infty U_\infty C / \mu_\infty$ and Pr is the Prandtl number defined as $Pr = \mu_\infty C_p / \kappa_\infty$. C is the reference length, subscript ∞ stands for freestream variables, C_p is the heat capacity at constant pressure, μ is the viscosity and κ is the thermal conductivity.

2.2 Numerical Methods for Large Eddy Simulation

2.2.1 Introduction

The important features of the numerical methods used for resolving high Reynolds flows used for database in the present work will be discussed. The database is constructed by the use of large eddy simulations conducted to accurately resolve nearfield physics. Typically, the grid resolution in terms of wall units for wall-resolving LES (Wagner *et. al*, 2007) is given by $50 < \Delta x^+ < 100$, $\Delta y^+ < 1$ and $10 < \Delta z^+ < 20$, where x, y and z are the streamwise, wall-normal and spanwise flow directions, respectively.

With the overset mesh capability implemented by Bhaskaran and Lele (2010), a body-fitted O-mesh is carefully designed to resolve the turbulent boundary layers along the airfoil wall region and a background rectangular mesh is designed to capture the turbulent wake behind the airfoil. The stretching factor of the background mesh is chosen such that metric terms are smooth and, therefore, the acoustic nearfield is captured with no distortions. The background mesh needs to be large enough for which boundary conditions to not affect the flow with reflections of acoustic waves or distortions of the mean flow field. A two-step second-order implicit scheme is used for the O-mesh since the fine grid spacings near the wall impose significant restrictions on the time step for explicit time marching schemes. A third-order explicit time marching scheme is used for the coarser background mesh since, for this mesh, the time step is restricted by accuracy rather than stability. More details about the numerical methods described in this Section can be found in Nagarajan *et. al* (2007) and Bhaskaran and Lele (2010).

2.2.2 Spatial Discretization

The numerical scheme for spatial discretization is a sixth-order accurate compact scheme from Nagarajan *et. al* (2003) implemented on a staggered grid. In a general curvilinear coordinate system, the staggered first derivative, $f^{'}$, of a function f at interior nodes is computed as

$$\alpha f^{'}_{j-1} + f^{'}_{j} + \alpha f^{'}_{j+1} = b\frac{f_{j+3/2} - f_{j-3/2}}{3\Delta x} + a\frac{f_{j+1/2} - f_{j-1/2}}{\Delta x}, \tag{2.8}$$

where $\alpha = 9/62$, $a = 3/8(3 - 2\alpha)$ and $b = 1/8(-1 + 22\alpha)$. The use of a staggered variable arrangement requires a mid-point interpolation formula. The implemented

sixth-order accurate formula is given by

$$\alpha f^I_{j-1} + f^I_j + \alpha f^I_{j+1} = b\frac{f_{j+3/2} - f_{j-3/2}}{2} + a\frac{f_{j+1/2} - f_{j-1/2}}{2}, \tag{2.9}$$

where $\alpha = 3/10$, $a = 1/8(9 + 10\alpha)$ and $b = 1/8(-1 + 6\alpha)$. The boundary and near-boundary nodes require one side derivative and interpolation formulas that can be found in Nagarajan *et. al* (2007).

Compact finite-difference schemes are non-dissipative and numerical instabilities arising from insufficient grid resolution, mesh non-uniformities, approximate boundary conditions and interpolation at grid interfaces have to be filtered to preserve stability of the numerical schemes. The high wavenumber compact filter presented by Lele (1992) is applied to the computed solution at prescribed time intervals in order to control numerical instabilities. A one parameter family of sixth-order filters is constructed using

$$\alpha\tilde{f}_{j-1} + \tilde{f}_j + \alpha\tilde{f}_{j+1} = af_j + b\frac{f_{j+1} + f_{j-1}}{2} + c\frac{f_{j+2} + f_{j-2}}{2} + d\frac{f_{j+3} + f_{j-3}}{2}, \tag{2.10}$$

where $\tilde{f}_j$ is the filtered solution, $a = 1/16(11 + 10\alpha)$, $b = 1/32(15 + 34\alpha)$, $c = 1/16(-3 + 6\alpha)$ and $a = 1/32(1 - 2\alpha)$. The spectral response of the filter is adjusted by the filter coefficient α that ranges from $-0.5 \leq \alpha \leq 0.5$. Higher values of α provide less dissipation and values of $\alpha \geq 0.48$ are used in the present computations. The boundary nodes use different filtering formulas that can be found in Bhaskaran and Lele (2010).

2.2.3 Time Integration

Far away from the solid boundaries, the governing equations are integrated using an explicit third-order compact storage Runge-Kutta scheme (Wray, 1986). After the spatial discretization, the set of partial differential equations become a set of ordinary differential equations that can be expressed in the form

$$\frac{dQ}{dt} = f(Q, t). \tag{2.11}$$

This set of ordinary differential equations can be integrated from t^n to t^{n+1} using the following third-order Runge-Kutta scheme

$$Q^{n+1/3} = Q^n + \frac{8}{15}\Delta t f(Q^n, t^n)$$

$$Q^{n+2/3} = Q^n + \frac{1}{4}\Delta t f(Q^n, t^n) + \frac{5}{12}\Delta t f(Q^{n+1/3}, t^{n+1/3})$$

$$Q^{n+1} = Q^n + \frac{1}{4}\Delta t f(Q^n, t^n) + \frac{3}{4}\Delta t f(Q^{n+2/3}, t^{n+2/3}),$$

where the intermediate time levels are $t^{n+1/3} = t^n + 8/15\Delta t$ and $t^{n+2/3} = t^n + 2/3\Delta t$.

The time integration of the fluid equations is carried out by a fully implicit second-order Beam-Warming scheme (Beam and Warming, 1978) in the near-wall region in order to overcome the time step restriction. The second-order implicit method is given by

$$\frac{3Q^{n+1} - 4Q^n + Q^{n-1}}{2\Delta} = f(Q^{n+1}, t^{n+1}). \tag{2.12}$$

The right hand side is solved through approximate factorization followed by diagonalization of the implicit matrix in the x and z directions. Details about the approximate factorization are presented by Nagarajan *et. al* (2007).

2.2.4 Boundary Conditions

Sponge layers and characteristic boundary conditions based on Riemann invariants are applied at inflow and outflow boundaries. For a subsonic inflow boundary, four incoming quantities must be specified along with one outgoing quantity computed from the interior domain. In the current study, the entropy, tangential and spanwise velocities and incoming Riemann invariant are constrained. The outgoing Riemann invariant is computed by extrapolation from the interior nodes neighboring the inflow boundary. For a subsonic outflow boundary, one incoming quantity must be specified along with four outgoing quantities computed from the interior domain. Here, the incoming Riemann invariant is imposed and the entropy, tangential and spanwise velocities and outcoming Riemann invariant are computed by extrapolation from the interior nodes neighboring the outflow boundary.

Assuming an inflow boundary located at a x plane normal to the inflow, the locally one-dimensional Riemann invariants are defined in the normal direction as

$$R_1 = u - \frac{2c}{\gamma - 1} \tag{2.13}$$

and

$$R_2 = u + \frac{2c}{\gamma - 1}, \tag{2.14}$$

where u is the velocity in the x Cartesian direction normal to the inflow and c is the local speed of sound. Hence, at the inflow boundary, the following constraints are applied $v = v_{inflow}$, $w = w_{inflow}$, $s = s_{inflow}$, $R_1 = R_{1_{incoming}}$ and $R_2 = R_{2_{outgoing}}$. The outgoing Riemann invariant, R_2, is computed using zero-th order extrapolation from the plane immediately neighboring the inflow plane. The primitive variables can be constructed from the constraints as

$$u = \frac{1}{2}(R_{1_{incoming}} + R_{2_{outgoing}}), \tag{2.15}$$

$$c = \frac{\gamma - 1}{4}(R_{2_{outgoing}} - R_{1_{incoming}}), \tag{2.16}$$

$$\rho = \left(\frac{c^2}{\gamma s_{inflow}}\right)^{\frac{1}{\gamma - 1}} \tag{2.17}$$

and

$$T = \frac{c^2}{\gamma - 1}. \tag{2.18}$$

The same methodology applies to an outflow boundary condition. However, only the incoming Riemann invariant is imposed and the other constraints are obtained by zero-th order extrapolation from the interior plane immediately neighboring the outflow plane. In the current simulations, both inflow and outflow boundary conditions are applied on the background mesh, where an explicit time marching scheme is used. At each time step the solutions in the inflow and outflow planes are updated with those obtained from the application of the inflow and outflow boundary conditions, respectively. The boundary conditions are applied after transformation to a Cartesian coordinate system along a normal to the boundary plane. The velocity components are first evaluated at the density nodes and then interpolated to their respective staggered locations.

A damping sponge layer is also applied along the inflow and outflow boundaries to minimize reflections of disturbances (Nagarajan *et. al*, 2007; Bhaskaran and Lele, 2010). In the sponge layers, the following relaxation term is added to the governing equations

$$-\sigma(Q - Q_{ref}), \tag{2.19}$$

where σ is the sponge strength specified as

$$\sigma = A\left(\frac{x - x_{sponge}}{L - x_{sponge}}\right)^n. \tag{2.20}$$

Here, x_{sponge} is the starting sponge location and L is the full length of the sponge layer. The sponge effect vanishes at the starting location and gradually grows in the

strength as the maximum size of the sponge is reached. The sponge reference solution, Q_{ref}, is specified as the freestream condition. The constants A and n used in the present computations are $A = 20$ and $n = 4$. These values are found by numerical experimentation and provide good results for the present grid and flow configurations.

Adiabatic, no-slip boundary conditions are applied at the solid boundaries. The wall density is obtained by the solution of the continuity equation

$$\frac{\partial \rho}{\partial t} + \frac{\partial (\rho u_i)}{\partial x_i} = 0. \tag{2.21}$$

The momentum and energy equations are replaced by the following constraints on the velocity

$$\rho u_i = 0 \tag{2.22}$$

and temperature

$$\frac{\partial T}{\partial n} = 0, \tag{2.23}$$

where the term $\partial(.)/\partial n$ represents a derivative in the wall-normal direction.

2.2.5 Overset Mesh Capability

A fourth-order Hermite interpolation scheme is implemented in the current overset mesh capability. Interpolation is performed in two dimensions (streamwise and wall-normal) since the third dimension (spanwise) is homogeneous in the present simulations. In two dimensions, the Hermite interpolation at an overlap point is constructed using function values and first derivatives at the four surrounding points in the donor grid that bounds the interpolated point in the uniform computational space. The coordinates (ξ, η) form a local grid system that is constructed in the computational space. The origin of this coordinate system is at the center of the box formed by the points bounding the interpolated point. The coordinates of the interpolated point in this local coordinate system are found by the inverse mapping $(\xi, \eta) = M^{-1}(x, y)$. The forward mapping $M(\xi, \eta)$ is defined at all points using the Hermite interpolation scheme, and the inverse mapping $M^{-1}(x, y)$ is found using a Newton-Raphson procedure. The

interpolation formula is given by

$$f(\xi,\eta)=\sum_{l,k=0}^{1}\left[C_{lk}^{0}(\xi,\eta)f_{i+l,j+k}+C_{lk}^{\xi}(\xi,\eta)\left(\frac{\partial f}{\partial\xi}\right)_{i+l,j+k}+C_{lk}^{\eta}(\xi,\eta)\left(\frac{\partial f}{\partial\eta}\right)_{i+l,j+k}\right]+O(\Delta^{4}), \tag{2.24}$$

where the interpolation coefficients are given by

$$\begin{aligned}
C_{lk}^{0}(\xi,\eta)&=\left[\frac{1}{2}-(-1)^{l}\xi\right]\left[\frac{1}{2}-(-1)^{k}\eta\right]\\
&\{1-2\left[(-1)^{l}\xi\left(\frac{1}{2}+(-1)^{l}\xi\right)+(-1)^{k}\eta\left(\frac{1}{2}+(-1)^{k}\eta\right)\right]\},\\
C_{lk}^{\xi}(\xi,\eta)&=(-1)^{l}\left(\frac{1}{4}-\xi^{2}\right)\left[\frac{1}{2}-(-1)^{l}\xi\right]\left[\frac{1}{2}-(-1)^{k}\eta\right],\\
C_{lk}^{\eta}(\xi,\eta)&=(-1)^{k}\left(\frac{1}{4}-\eta^{2}\right)\left[\frac{1}{2}-(-1)^{l}\xi\right]\left[\frac{1}{2}-(-1)^{k}\eta\right].
\end{aligned} \tag{2.25}$$

More details about the implementation of the method of overset grids can be found in Bhaskaran and Lele (2010).

2.3 Aeroacoustic Analogies

The aeroacoustic equations derived from Lighthill (1952) can be expanded to account different types of sound sources in the flow field. In this context, the general Ffowcs-Williams and Hawkings (1969) (FW-H) acoustic analogy is used for noise predictions. The integral formulation in frequency domain can be written as

$$\begin{aligned}
\left[\hat{p'}H\left(f\right)\right]=-\int_{f=0}\left[i\omega\hat{Q}\left(\mathbf{y}\right)G\left(\mathbf{x},\mathbf{y}\right)+\hat{F}_{i}\left(\mathbf{y}\right)\frac{\partial G\left(\mathbf{x},\mathbf{y}\right)}{\partial y_{i}}\right]dS\\
-\int_{f>0}\hat{T}_{ij}H\left(f\right)\frac{\partial^{2}G\left(\mathbf{x},\mathbf{y}\right)}{\partial y_{i}\partial y_{j}}dV\ ,
\end{aligned} \tag{2.26}$$

where $i=\sqrt{-1}$, p' is the acoustic pressure, ω is the angular frequency, $\mathbf{y}=(y_1,y_2,y_3)^t$ is the source position, $\mathbf{x}=(x_1,x_2,x_3)^t$ is the observer's position. Hat over variables $(\hat{.})$ means it's in frequency domain. The $f=0$ term represents the FW-H surface and $H\left(f\right)$ is the Heaviside function defined as $H\left(f\right)=1$, if $f>0$, and $H\left(f\right)=0$, if $f<0$. Monopole $\hat{Q}\left(\mathbf{y}\right)$ and dipole $\hat{F}_i$ acoustic sources are given by

$$Q=\left[\rho\left(u_i+U_i\right)-\rho_0U_i\right]\partial f/\partial x_i\ , \tag{2.27}$$

$$F_i = \left[p'\delta_{ij} - \tau_{ij} + \rho\left(u_i - U_i\right)\left(u_j + U_j\right) - \rho_0 U_i U_j\right] {}^{\partial f}/_{\partial x_i} \ . \tag{2.28}$$

Here, u_i represents a Cartesian fluid velocity vector and U_i is the FW-H surface velocity vector, ρ_0 is the free-stream density, p' is the acoustic pressure, p is pressure, δ_{ij} is the Kronecker delta (which is 0 if $i \neq j$ and 1 if $i = j$) and τ_{ij} is the viscous stress tensor. Quadrupole sources are defined as

$$T_{ij} = \rho u_i u_j + \left(p1 - c_0^2 \rho^{'}\right)\delta_{ij} - \tau_{ij} \ , \tag{2.29}$$

where c_0^2 is the free-stream sound speed. If one considers mean flow velocity in cartesian x-direction, the three-dimensional Green's function accounting to convective effects is given by

$$G\left(\mathbf{x},\mathbf{y}\right) = -\frac{exp\left\{\frac{-ik}{1-M^2}\left[\sqrt{\left(x_1-y_1\right)^2 + \left(1-M^2\right)\left[\left(x_2-y_2\right)^2 + \left(x_3-y_3\right)^2\right]} - M\left(x_1-y_1\right)\right]\right\}}{4\pi\sqrt{\left(x_1-y_1\right)^2 + \left(1-M^2\right)\left[\left(x_2-y_2\right)^2 + \left(x_3-y_3\right)^2\right]}} \ . \tag{2.30}$$

In this equation, k is the wavenumber, M is the free-stream Mach Number defined as $M \equiv U_1/c_0$. The Eq. 2.30 can be used for two-dimensional cases, considering $x_3 = y_3$. In the present work, the FW-H surface is computed over the solid airfoil surface and because of this assumption, Eq. 2.26 integrals are computed over a solid body only. In this way, $u_i = U_i$ for both dipole and monopole sources, reducing Eqs. 2.31 and 2.32 to

$$Q = -\rho_0 U_i {}^{\partial f}/_{\partial x_i} \ , \tag{2.31}$$

$$F_i = \left[p^{'}\delta_{ij} - \tau_{ij} + \rho_0 U_i U_j\right] {}^{\partial f}/_{\partial y_i} \ . \tag{2.32}$$

So, monopole sources and the second term of the dipole sources are now stationary, having no influence in frequency domain analysis. For Low-Mach number flows and, due to the fact that FW-H surface is considered a solid body over the airfoil, the quadrupole sources will be neglected and Eq. 2.26 can be re-writen as the Curle's Analogy (Curle, 1955)

$$\hat{p^{'}}\left(\mathbf{x}\right) = -\int_{Surf} \hat{p'}\left(\mathbf{y}\right) n_i \frac{\partial G\left(\mathbf{x},\mathbf{y}\right)}{\partial y_i} dS \ . \tag{2.33}$$

The surface integral appearing on Eq. 2.33 is computed along the scattering body surfaces and dipole sources are define only as $\hat{F}_i = \hat{p'} n_i$, with n_i being the normal vector

pointing outside the airfoil surface. The Hanning filter proposed by Lockard (2000) is used to guarantee conservation of the dipole sources energy before transforming data to frequency domain.

3 Proper Orthogonal Decomposition

3.1 Mathematical Formulation

Turbulent flows are composed of a wide range of scales and frequencies and identifying coherent structures and its dynamic behavior is not always an easy task in the space-time domain. Therefore, many techniques for modal analysis and statistical approaches have been used in order to improve the knowledge on turbulence and coherent structures.

Turbulence can be highly nonlinear, so a modal analysis may account to the propagation of waves in broad range of frequencies in both time and space. For analyzing a non-linear system of partial differential equations, as described in Section 2.1, global modes can be used to capture the coherent oscillations in time (Drazin, 1974). Since the 1990s, modal analysis of turbulent flows has gained importance for analyzing unsteady aerodynamics as shown by Huerre and Monkewitz (1990) and later by Hall (1994) and Dowell *et. al* (1998).

Among the several modal decomposition techniques, one can cite the Proper Orthogonal Decomposition (POD) that was first proposed by Lumley (1967) as a modal decomposition technique for unsteady flowfields, especially for the analysis of turbulent coherent structures. In this chapter, a brief discussion on the main features of POD will be provided and, for further details and mathematical formulation, the work by Rowley (2002), Cordier and Bergmann (2003), Freund and Colonius (2009), Andrianne *et. al* (2009) and Podvin *et. al* (2010) is recommended.

In POD, the vector of flow quantities $\mathbf{q}(\mathbf{x}, t)$ is assumed to be a function of space and time. This vector can be decomposed as a sum of the mean flow and fluctuation quantities $\bar{\mathbf{q}}(\mathbf{x}, t)$ and $\mathbf{q}'(\mathbf{x}, t)$, respectively. The latter can be further expanded in a combination of vector-valued spatial eigenfunctions $\boldsymbol{\phi}_i(\mathbf{x})$ and its time-coefficient mode amplitudes $\mathbf{a}_i(t)$ for a defined number of M modes as

$$\mathbf{q}(\mathbf{x}, t) = \bar{\mathbf{q}}(\mathbf{x}) + \mathbf{q}'(\mathbf{x}, t) = \bar{\mathbf{q}}(\mathbf{x}) + \sum_{i=1}^{M} \mathbf{a}_i(t)\boldsymbol{\phi}_i(\mathbf{x}) \ . \tag{3.1}$$

There are several ways of computing the terms $\boldsymbol{\phi}_i(\mathbf{x})$ and $\mathbf{a}_i(t)$. For example, one can cite two standard POD techniques such as the classical method, also known as direct method, and the snapshot method, well described by Cordier and Bergmann (2003). A combination between the discrete Fourier transform (DFT) and POD can be used

when the flow field has translational symmetry, also known as homogeneous turbulence direction. In this case, the POD modes along the homogeneous direction are the Fourier modes (Lumley, 1970). For all numerical database cases studied in the present work, the spanwise direction is considered to be homogeneous and, therefore, the vector of flow quantities $\mathbf{q}(\mathbf{x}, t)$ can be re-written as

$$\mathbf{q}(x, y, z, t) = \sum_k \mathbf{q}_k(x, y, t) e^{2i\pi(kz/L_z)} \ , \tag{3.2}$$

where L_z is the periodic dimension of the flow and kz is the spanwise wavenumber. The direct method computes the spatial correlation matrix and averages over time. This is the technique of choice for experimental data that are usually obtained with a high time resolution but are poorly resolved spatially (Cordier and Bergmann, 2003).

In general, one may consider $\mathbf{Q}$ as a matrix consisted of grid points in rows and time frames ordered in columns. POD is a singular value decomposition (SVD) of the matrix $\mathbf{Q}$. For more details on the mathematical background on SVD an its relation with POD, one may refer to the work of Atwell and King (2004). For mathematical basis on eigenvalue decomposition and SVD, the books of Saad (1992), Trefethen and Bau III (1997), Horn and Johnson (2012) and Golub and Van Loan (2012) are highly recommended.

$$\mathbf{Q} = \mathbf{U}\mathbf{\Sigma}\mathbf{V}^* \ , \tag{3.3}$$

where $\mathbf{U}$ is the spatial eigenfunction matrix formed by grid points in rows and modes in columns, $\mathbf{\Sigma}$ is the diagonal singular values matrix and $\mathbf{V}^*$ is the Hermitian matrix that gathers the temporal dynamics of the POD modes.

One may consider that solving SVD for high-fidelity turbulence data is unfeasible due to computational memory costs. A less expensive approach is using the snapshot method, which consists of solving the SVD problem not for the database $\mathbf{Q}$, but for a correlation matrix formed by $\mathbf{Q}^T\mathbf{Q}$, or a covariance matrix formed by $\frac{1}{N}\mathbf{Q}^T\mathbf{Q}$, where N is the number of snapshots or time frames. As N is a scalar, it influences only the singular values, not the eigenvectors. The right singular vectors, $\mathbf{V}$, are the orthonormal eigenvectors of $\mathbf{Q}^T\mathbf{Q}$. The square roots of the eigenvalues of $\mathbf{Q}^T\mathbf{Q}$ are equal to the singular values $\mathbf{\Sigma}$.

In the present work, we prefer to use the snapshot method since our numerical simulations provide a high resolution in space but with a limited number of collected snapshots, resulting in a correlation matrix feasible to be computed via SVD. Here, we generalize the vector of primitive variables as $\mathbf{q} = (\rho, u_x, u_y, u_z, p)^t$, where $(u_x, u_y, u_z)^t$ are the Cartesian velocity components, ρ is the density and p is the pressure. The snapshots of $\mathbf{q}$ are computed at time t and the correlation matrix C_{ij} is defined as the following

product of a number N snapshots computed along a domain of fluid Ω

$$C_{ij} = \frac{1}{N} \left(\mathbf{q}'(\mathbf{x}, t_i), \mathbf{q}'(\mathbf{x}, t_j) \right)_\Omega \ . \tag{3.4}$$

Using a correlation matrix it is also possible to vectorize the matrix using a POD norm. We define a norm vector $\boldsymbol{\beta} = (\beta_1, ..., \beta_5)$ that determines which norm is being used in the POD analysis. A kinetic energy norm uses $\boldsymbol{\beta} = (0, 1, 1, 1, 0)$, a pressure-based norm uses $\boldsymbol{\beta} = (0, 0, 0, 0, 1)$ and so on. Considering $\mathbf{q}'(\mathbf{x}, t_i) = \mathbf{q}'_i$, the norm vector is applied together with the inner product of the snapshots as follows

$$C_{ij} = \left(\mathbf{q}'_i, \mathbf{q}'_j \right)_\Omega = \int_\Omega \left[\beta_1 \rho'_i \rho'_j + \beta_2 u'_{xi} u'_{xj} + \beta_3 u'_{yi} u'_{yj} + \beta_4 u'_{zi} u'_{zj} + \beta_5 p'_i p'_j \right] d\Omega \ , \tag{3.5}$$

where Ω is the fluid region employed to provide the physics for the reconstruction, here called the domain of information. This domain is an important part of the POD reconstruction. For instance, if one intends to understand the coherent structures along the wake of a bluff body, this flow region should be used as the domain of information and a kinetic energy norm could be used. If the interest lies in the acoustic far-field, one should use the domain of information along the acoustic field only.

The singular values are computed as follows:

$$\mathbf{CS} = \boldsymbol{\lambda} \mathbf{S} \ , \tag{3.6}$$

where $\mathbf{S}$ is the matrix of right eigenvectors of $\mathbf{C}$ and $\boldsymbol{\lambda}$ represents the matrix with the eigenvalues of $\mathbf{C}$. Here, SVD can be employed to compute the eigenvalues and eigenvectors of $\mathbf{C}$ since this matrix is positive semi-definite (Atwell and King, 2004). The LAPACK package (Anderson *et. al*, 1999) is used to perform the SVD computations. As the matrices computed in 3.6 are square of order about 1000, no parallelization is required.

The covariance matrix is used for the SVD computation. The usage of the snapshot method to form a covariance matrix $\mathbf{C}$ leads to a normalization of the singular values $\mathbf{S}$ in order to form an orthogonal basis of eigenvectors, written in the form $\mathbf{s}_i \sqrt{\lambda_i N}$. Here, the term $\mathbf{s}_i$ is the ith-column of matrix $\mathbf{S}$ and N is the number of snapshots. In this sense, the spatial eigenfunctions of the POD reconstruction can be defined as

$$\boldsymbol{\phi}_i (\mathbf{x}) = \frac{1}{\sqrt{\lambda_i N}} \sum_{m=1}^{N} \mathbf{q}'_i (\mathbf{x}) \, \mathbf{s}_i^m \ . \tag{3.7}$$

As the flowfield is decomposed, the spatial eigenfunctions are only dependent of the position. However, the mode amplitudes are functions of time and describe the unsteady dynamics of the flowfield composed by the spatial eigenfunctions. The mode amplitudes

can be computed as

$$\mathbf{a}_i\left(t\right) = \int_{\Omega} \mathbf{q}_i'\left(\mathbf{x},t\right) \boldsymbol{\phi}_i\left(\mathbf{x}\right)\ d\Omega\ . \tag{3.8}$$

Eventually, as already stated, the domain of information Ω can be different from the entire flow field domain. Hence, a more general form of computing the time coefficients of the model shape amplitudes can be used. The general formula takes into account only the eigenvectors and eigenvalues generated by solution of the eigenvalue problem in Eq. 3.6. In this way, the mode amplitudes $\mathbf{a}_i\left(t\right)$ are related to the domain of information as well as to the spatial eigenfunctions $\boldsymbol{\phi}_i\left(\mathbf{x}\right)$. So, for a number N of snapshots, in a simplified form, the mode amplitudes $\mathbf{a}_i\left(t\right)$ are computed in the following form in the snapshot method

$$\mathbf{a}_i\left(t\right) = \mathbf{s}_i\sqrt{\lambda_i N}\ . \tag{3.9}$$

Since we are able to perform a modal decomposition of the unsteady components of the flow, it is possible to reconstruct the flowfield with using only a limited number of spatial eigenfunctions and mode amplitudes using Eq. 3.1. If one has a number N of snapshots, it is possible to generate the same number of eigenvalues and eigenfunctions. By definition, a reconstruction employing all the M modes (where $M = N$) would result in the original unsteady flow.

POD has received attention in the several fields of study due to its capacity of data compression. In this sense, when the SVD procedure is applied to the correlation matrix, it provides the singular values in an organized fashion, in this case, in a decreasing order of magnitude. Therefore, it is possible to separate the POD modes based on their energy. One of the important aspects of POD is that one can then reconstruct the flowfield using the most energetic modes. For several flows, the use of only a few modes may result in the reconstruction of a flowfield with the important dynamics and, hence, compressing information of large numerical and experimental databases. As already mentioned, if one uses Eq. 3.1 with the all snapshots and modes, the reconstructed flowfield will contain 100% of the original flowfield energy. In this case, the reconstructed flowfield $\mathbf{q}^*(\mathbf{x},t)$ will be given by

$$\mathbf{q}^*(\mathbf{x},t) = \mathbf{q}(\mathbf{x},t)\ . \tag{3.10}$$

If the flowfield is reconstructed with $N < M$ modes, $\mathbf{q}^*(\mathbf{x},t)$ will be an approximation of the original flow $\mathbf{q}(\mathbf{x},t)$ and it will contain the information related to the spatial eigenfunctions and mode amplitudes used in the reconstruction process. Therefore, POD can be applied in two ways: a) it can be used to understand the dynamics of specific flow

structures such as coherent structures in turbulence and b) it can be used to reconstruct complex flowfields using the most energetic scales of the flow and, hence, to compress large databases and to generate reduced-order models.

3.2 1D Periodic Domain POD

In order to clarify and state important features of POD, a test case will be computed in a one-dimensional (1D) periodic domain. As stated previously by Lumley (1970), in homogeneous directions, POD modes are Fourier modes. In the present case, a wave is described initially by Eq. 3.11, which satisfies the homogeneous condition. The pure advection of this wave is solved using a high-order accurate numerical methodology.

$$p(x) = \frac{1}{1 + 25x^2} \ . \tag{3.11}$$

A 6th-order compact finite-difference scheme (Lele, 1992) is used for the spatial discretization of the linear wave equation and a 4th-order Runge-Kutta explicit scheme is used for the time marching. The numerical scheme employed here for the spatial discretization should introduce little numerical dissipation. Therefore, the entire procedure should produce high-frequency oscillations which should be damped by low-pass filters. In the present case, no explicit filtering techniques are used to highlight the POD capabilities of capturing small scale fluctuations in less energy-containing modes. Figure 3.1 shows the wave propagation after one period of simulation in the periodic domain. This figure also shows the spectral content for one single point in the spatial domain. In the present simulation, the CFL parameter was set to $CFL = 0.5$ to guarantee stability of the numerical scheme.

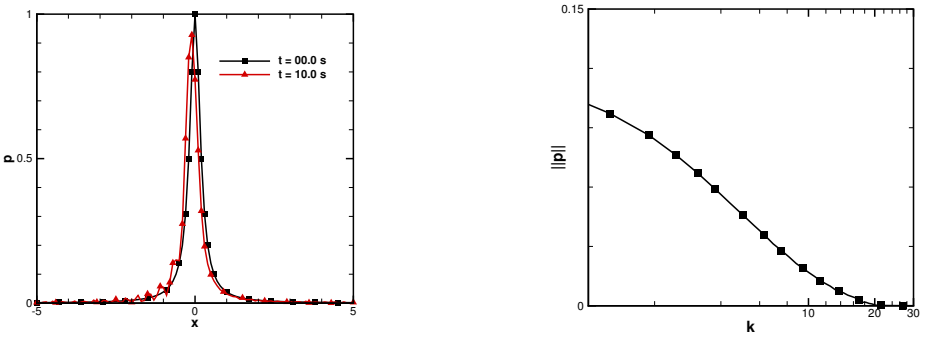

(a) Wave advection in time. (b) Spectral content of the wave.

Figure 3.1: Time and spectral content of the wave given by Eq. 3.11 propagated in a 1D periodic domain.

The correlation matrix is computed for the present data set in a simplified version of the Eq. 3.4. Figure 3.2 shows an example of correlation matrix and the distribution of eigenvalues over the POD spectrum. Since the case is periodic, the first and the last snapshots are highly correlated due to the small dissipation and dispersion inherent to the high-order numerical methods used in the wave propagation. The first eigenvalues shown in Fig. 3.2(b) contain most of the energy. Figure 3.2(c) shows the accumulative values of the normalized singular values for a number n of POD modes. We may call the accumulative singular values as the convergence of the POD modes, since it shows the relative amount of energy present for a number n of POD modes compared to the full energy of the dataset. One can notice that a reconstruction using around 50 modes would have almost the total amount of energy of the original dataset. Figure 3.2(c) is obtained by the sum of the normalized singular values shown in Fig. 3.2(b).

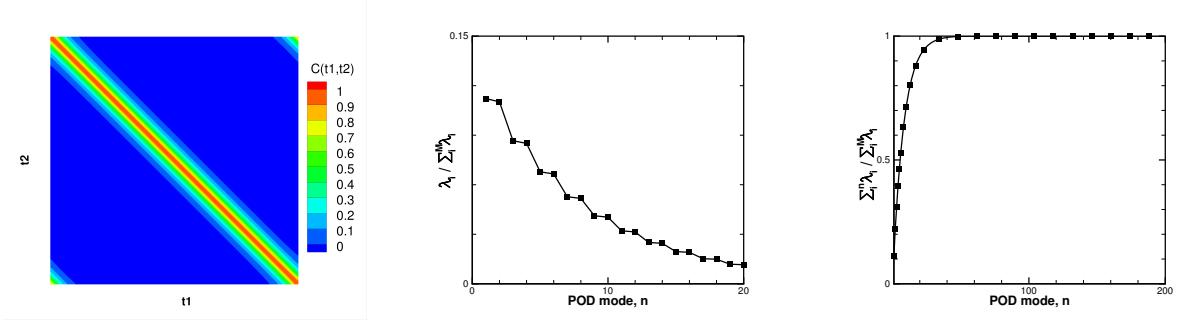

(a) Correlation matrix.

(b) Normalized singular values of POD modes.

(c) Normalized sum of singular values.

Figure 3.2: Correlation matrix, its singular values in the POD spectrum and the POD energy convergence to original data set.

POD modes usually appear in pairs, as shown in Fig. 3.2(b), where the coupled modes have similar amplitudes. In this case, their behavior is similar to Fourier modes which are mirrored in the Fourier spectrum. However, in POD, due to the singular values decomposition, they are ranked in an energetic sense, from the most energy-containing ones to the lowest energetic ones. Paired modes usually have useful information in turbulent data set analysis, as will be shown later.

In POD modes that contain small portions of the energy of the original data set, the signal-to-noise ratio may affect the clarity of the information in the eigenfuntions and mode amplitudes. For the present case, this appears for modes beyond 50. Hence, POD modes with small signal-to-noise ratio are not considered when extracting important information from the data set. For example, Fig. 3.3 shows how the most energy containing modes differ from those with small signal-to-ratio. One must remember that, due to its homogeneity, for the present 1D case, the POD modes have sine and cosine shapes and are phase correlated.

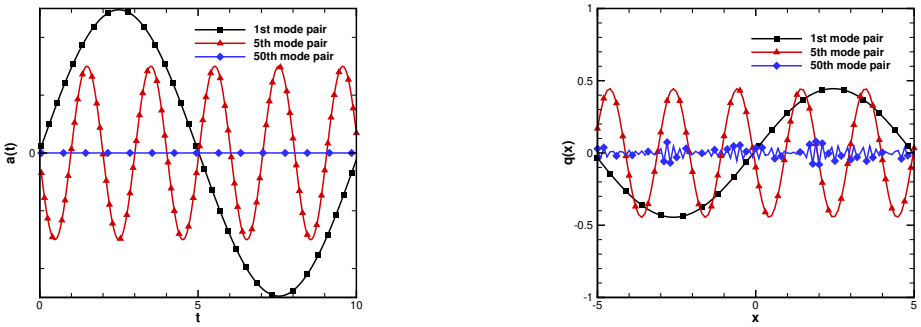

(a) Mode amplitudes. (b) Spatial eigenfunctions.

Figure 3.3: Spatial eigenmodes and mode amplitudes.

The flow reconstruction shown in Eq. 3.1 can be used to compress big data. In the present case, it is possible to see how the sum of the POD modes affect the reconstruction of the advected pressure wave. Here, POD is able to represent the important features of the original pressure wave as shown in Fig. 3.4.

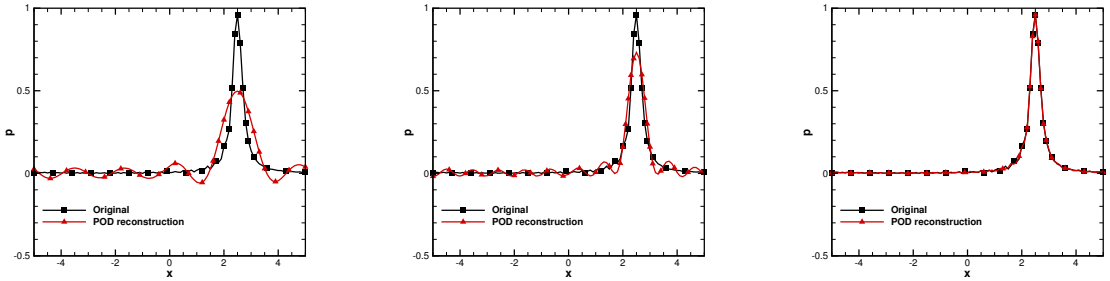

(a) 10 POD modes. (b) 20 POD modes. (c) 50 POD modes.

Figure 3.4: 1D domain POD reconstruction, using Eq. 3.1, compared to original wave propagation at $t = 2.5\ s$ ($^1/_4$).

Even when only 10 POD modes are employed in the reconstruction, the function peak is already represented in the correct portion of the domain, as shown in Fig. 3.4(a). A reconstruction using 20 modes, in Fig. 3.4(b), presents a wave form which is close to the original and, for a reconstruction with 50 modes or more, the small scale fluctuations present in the data are captured smoothly, as shown in Fig. 3.4(c). Not presented here, the use of 200 POD modes, which is the number of snapshots used in the full dataset, completely captures the data set information and reconstructs the original wave form, as shown in Section 3.1 and Eq. 3.10.

3.3 Flow Configuration

In this Section, the POD reconstruction is employed to analyze coherent structures in a turbulent flow past a NACA0012 airfoil with rounded trailing edge at 5 degs. angle of attack (AoA). This turbulent flow is obtained by a compressible large eddy simulation (LES) with wall resolution. The LES database was obtained by Wolf and co-authors and more details of the numerical methods employed in the simulation can be found in Wolf (2011). The structured spatial discretization is formed by a staggered grid body-fitted O-grid with $960 \times 125 \times 128$ grid points and a background grid with $896 \times 511 \times 64$ grid points. The dimensionless timestep is $\Delta t = 0.02$ for 874 time frames recorded in conservative variables. The total simulation time is 17.46. The baseline configuration uses blowing along the suction side of the airfoil to trip the boundary layer which becomes turbulent. The pressure side boundary layer is laminar since it is not tripped and develops under a favorable pressure gradient. Numerical results are compared to experimental data from Brooks, Pope and Marcolini (1989) and good agreement is obtained for the acoustic predictions.

The acoustic predictions for this flow configuration present a tonal peak which was thought to be related to the presence of correlated aeroacoustic sources along the span of the airfoil, as stated by Wolf *et. al* (2012). The current POD analysis will be employed to shed light into this topic. Figure 3.5 shows the turbulent flow passing over the suction side of the airfoil surface, after blowing is employed, and along the wake region downstream the trailing edge. The following POD techniques presented in this Section are used to provide a better understanding of possible coherent structures present in the flow. In this context, POD would serve as a filtering process to identify such structures in the turbulent flow.

The baseline case was selected due to the intricate physics that presents tonal and broadband noise generation. Figure 3.6 was presented by Wolf *et. al* (2012) and shows the sound pressure level spectrum at an observer located 7.9 chords at the mid-chord location above the trailing edge. Results are shown as a function of the Helmholtz number, kc, where k is the acoustic wavenumber and c is the airfoil chord. In this figure, numerical results are compared to experimental data available from Brooks *et. al* (1989) and it is possible to notice the good agreement between simulation and experiment, especially concerning the tonal peak at $kc = 8.5$ and a small peak between $kc = 15$ and 20. These peaks are thought to be associated to large coherent structures highly correlated along the spanwise direction, although these structures are not clearly observed in the numerical simulation. In general, tonal noise is associated with highly-coherent sources which generate noise at a specific frequency more efficiently. For example, a von Kármán

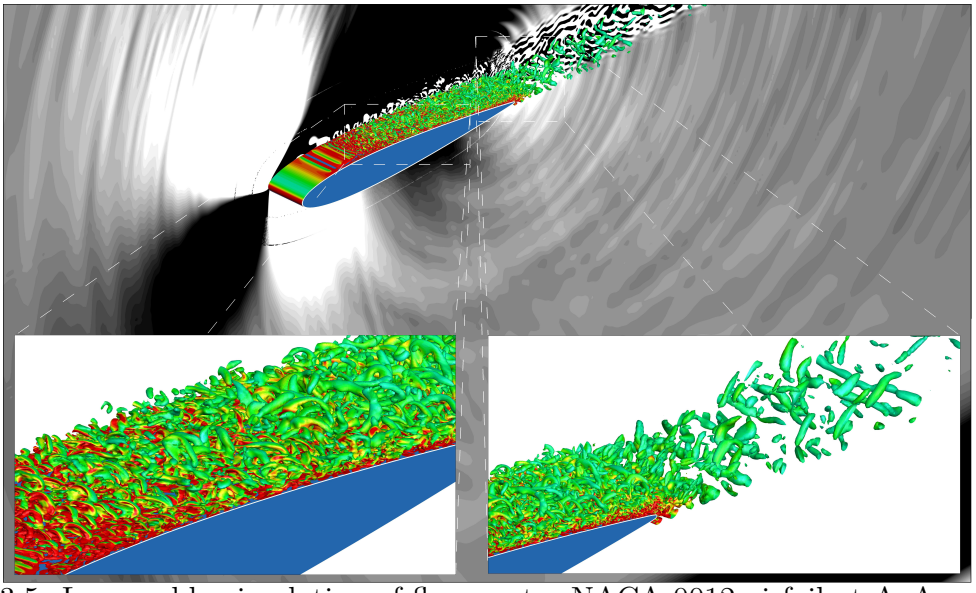

Figure 3.5: Large eddy simulation of flow past a NACA 0012 airfoil at AoA = 5 degs. AoA, $M_\infty = 0.115$, $Re_c = 408000$. Isosurfaces of Q-criterion coloured by vorticity magnitude with contours of divergence of velocity in the background. Airfoil surface in blue.

vortex street behind a cylinder would generate tonal noise at the reduced frequency of vortex shedding, $St \approx 0.2$, where the Strouhal number is given by $St = {}^{fD}/_{U_\infty}$. Here, f is the frequency, D is the cylinder diameter and U_∞ is the free stream velocity. While free turbulence would result in a set of uncorrelated three-dimensional eddies that generate noise in an inefficient fashion, vortex shedding could result in a spanwise coherent source that would generate noise in an almost two-dimensional fashion. In the current numerical simulation, where periodical boundary conditions are applied, this source could indeed be fully two-dimensional.

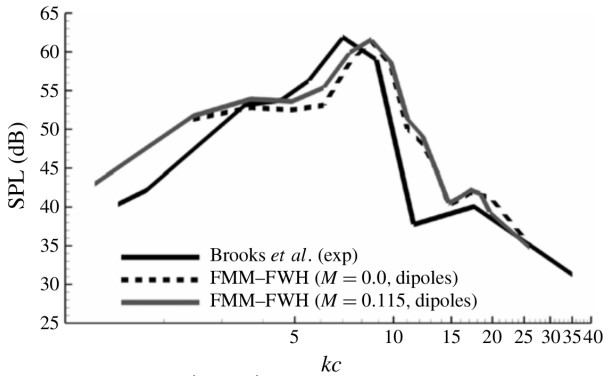

Figure 3.6: Sound pressure level (SPL) at an observer location $x = c$, $y = 7.9c$ and mid-span originally presented by Wolf *et. al* (2012).

As the results have a homogeneous direction along the airfoil span (z-direction), the snapshot method could be adapted considering that POD modes are Fourier modes in the z-direction Lumley (1970). The advantages of using Fourier decomposition in the

homogeneous direction, instead of computing the POD modes directly for the full domain, will be clarified along the text.

In this Section, the first POD approach employed will consider an average along the z-direction, *i.e.*, it will be a two-dimensional POD for the entire flowfield. Despite of the simplicity of this computation, it can yield very useful insights on POD norms to be used and the acoustic scattering, which can be easily computed for a 2D field.

The full three-dimensional proper orthogonal decomposition will also be implemented to analyze the behavior of the coherent structures in the spatial eigenfunctions and to perform a comparison with the Fourier-POD implementation. Also, in this chapter, a time spectral POD (SPOD) implementation Sieber *et. al* (2016) will be performed in the full 3D flowfield to assess the effects of filtering on the correlation matrix and its consequences in the decomposition of the most energy-containing structures in the flowfield. Different types of filtering will be tested and the importance of considering a periodic time signal will be analyzed.

Finally, the Fourier-POD will be analyzed in terms of the spatial eigenfunctions in order to identify coherent structures in the flowfield. Also, a coupled implementation of the Fourier-POD and the SPOD will be made to see how the filtering affects small disturbances at different Fourier modes.

3.4 Spanwise Averaged 2D POD

In order to filter three-dimensional fluctuations in the flow field, a spanwise average is performed resulting in a two-dimensional set of flow data. Figure 3.7 shows mean results for x-momentum and root mean square, RMS, of x-momentum. This 2D averaging process will be used for the analysis of POD norms. Figure 3.7 shows that fluctuations are considerably smaller than the mean values, however, they cannot be neglected.

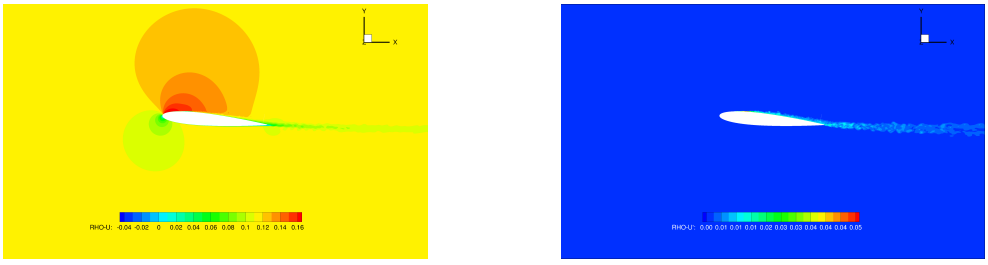

(a) X-momentum component.

(b) RMS of x-momentum component.

Figure 3.7: Results of spanwise averaging.

Despite its simplicity, 2D POD can provide insights about the different norms which can be used for the reconstruction process and also about the largest structures that

are present in the turbulent field. In the present work, both pressure (p-mean 2D) and kinetic energy (k-mean 2D) based norms are used. These norms are used in literature for POD analysis in many references, one important to be discussed is that Freund and Colonius (2009) found good results for reconstructing the acoustic waves using pressure norm and turbulent structures using kinetic energy norm. In this work we are willing to characterize the coherent structures where the turbulent fluctuations are higher, that is, near the airfoil and in the vortex wake region. For this reason the use of pressure norm computed only for acoustic waves region may not present good results when computing spatial eigenfunctions near the solid body, however their results will be compared among the other POD norms in further discussion (Section 3.5.2).

Considering that the term "mean 2D" is used here to emphasize that the POD reconstructions are employed in the 2D flowfield. As already discussed, POD allows the representation of most of the energy of the flowfield using a small number of modes. Figure 3.8 presents the energy contained in the first 20 modes for the reconstruction of the 2D spanwise-averaged flowfield and the sum of the energy for the first 200 modes. Initially, the sum of the energy of the modes for the pressure-based norm grows faster than for the kinetic energy one. Therefore, for a smaller number of POD modes, the reconstructed flowfield would have more energy for the pressure norm than for the kinetic energy one. This observation can also be made from the energy of the single modes.

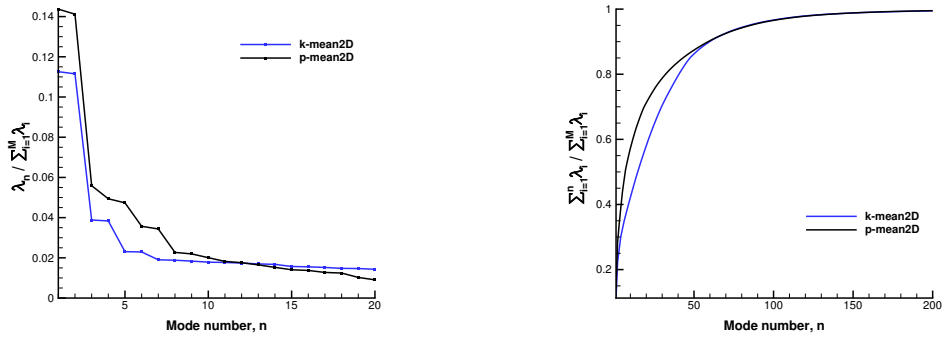

(a) Normalized energy of individual modes

(b) Cumulative energy of the modes.

Figure 3.8: Eigenvalues for pressure and kinetic energy POD norms.

POD norms may influence the coupling of modes and sometimes, singles modes may appear. For example, the results obtained by the kinetic energy norm presents a better coupling of eigenvalues than the pressure norm, as shown in Fig. 3.8(a). For the former norm, the three pairs of modes can be seen in the plot while, for the latter, modes 1 and 2 have similar energy levels, denoting a pair, but modes 3, 4 and 5 represent one pair and one single mode. This issue will affect the information contained in spatial eigenfunctions.

Figure 3.9 presents pressure fluctuations obtained by the first mode eigenfunction from

POD. One can see that the results obtained by the pressure norm have higher magnitudes of pressure fluctuations in the acoustic field compared to the kinetic energy norm. This is related to the information in Fig. 3.8 (a), where the pressure norm presents higher eigenvalues for the first modes.

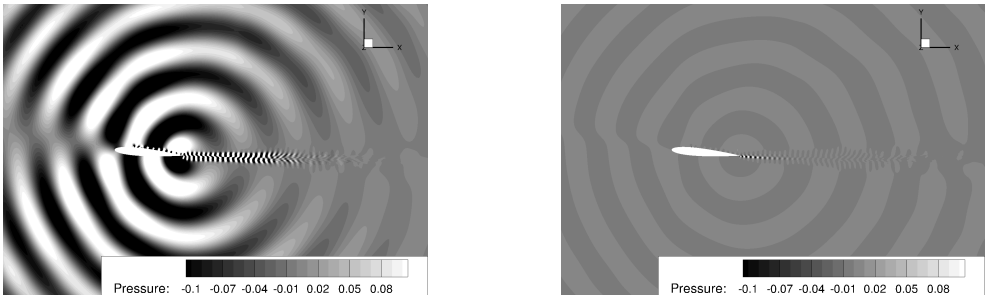

(a) Pressure norm. (b) Kinetic energy norm.

Figure 3.9: Pressure fluctuations obtained by the POD spatial eigenfunctions of mode 1.

3.4.1 Acoustic Analysis

For the sake of performing a refined analysis on the flow reconstruction using POD and its subsequent acoustic field, the solid Ffowcs-Williams and Hawkings (1969) formulation is implemented using a 2D approach. Here, the FWH formulation assumes that the sources and observers are in uniform motion and, therefore, the implementation is similar to Curle (1955). This study is performed to assess the effects of the POD reconstructions on the acoustic far-field. For this analysis, the sound spectra is computed using a POD reconstruction of the sources through the pressure-based norm, which is thought to be more appropriate for the acoustic analysis. Results are presented in Fig. 3.10 for the direct computational fluid dynamics (CFD) calculation, acoustic analogy and POD. In Fig. 3.10(a) the pressure fluctuations from CFD are measured directly at 1.0 chord length above the mid-chord of the airfoil. Curle's analogy results are computed at the same point using surface pressure fluctuations from the CFD data. The results of the original 2D flow (shown as CFD2D in the figure) and from the POD reconstruction (POD in the figure) are compared. One can see that the first 2 POD modes are able to reconstruct the tonal noise content of the spectrum at $kc = 8.5$. This means that the most energetic flow structures are associated with noise generation at that particular frequency. When more modes are added, the spectrum tends to approximate the original one computed from the CFD. Some differences between the direct calculation of pressure fluctuations in the acoustic field and the FWH solution are related to the lack of quadrupole sources which are neglected in the acoustic analogy computation.

A far-field analysis is also presented in terms of sound pressure level in Fig. 3.10(b)

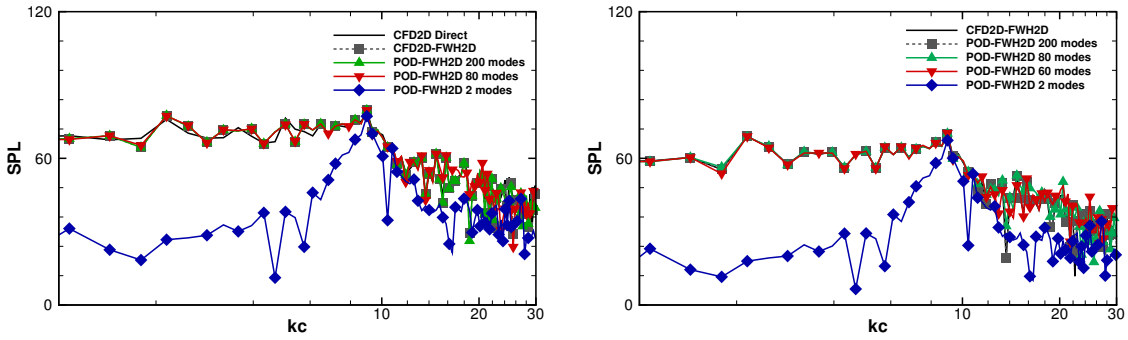

(a) Nearfield. (b) Farfield.

Figure 3.10: Pressure-based norm results for scattering spectra with acoustic analogy presented in Eq. 2.33.

where only the acoustic analogy is used to compute the sound spectra far from the airfoil. In this case, the observer is at $7.9c$ above the trailing edge and, therefore, this position is outside the CFD computational domain. Here, the POD reconstruction provides the surface pressure signal along the airfoil which is required for the FWH acoustic analogy. The spectral shape in the far-field is practically the same as for the near acoustic field, despite the differences in magnitude. Again, the first 2 modes are able to capture the tonal noise peak at $kc = 8.5$ and the other modes account for the broadband content of the sound spectrum.

A directivity analysis is also performed to assess the effects of the POD reconstruction on the noise propagation. Figure 3.11 presents directivity plots for different frequencies. These plots are obtained through pressure fluctuations which are reconstructed using a different number of modes. It is important to notice that both the magnitudes and shapes of the directivities are modified by the POD reconstructions. One can observe that, for the tonal noise frequency, the shape of the directivity is always similar, indicating that the first modes already contain the important content in terms of pressure fluctuations for this particular frequency. On the other hand, for other frequencies, the shapes of the directivities are completely different from the original FWH one. This means that the noise generated for these frequencies depends on finer turbulent structures which are not recovered in the POD reconstruction using only a few modes. That is, the use of more or less POD modes for reconstruction affects the properties of turbulence not only in magnitude, but in this case, also in the shape of acoustic scattering.

3.4.2 Turbulent Wake Analysis

The focus of the present study is to identify coherent structures in the flowfield along the turbulent wake. The kinetic energy and pressure norms will be employed

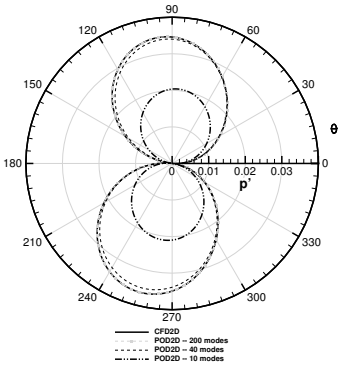

(a) $kc = 2.52$.

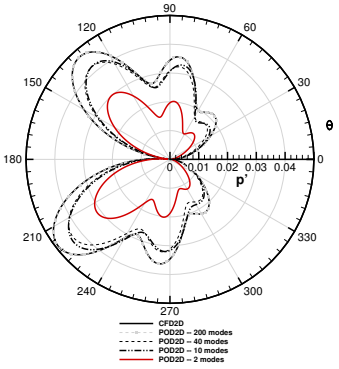

(b) $kc = 8.62$.

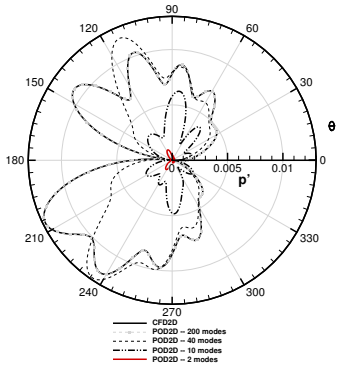

(c) $kc = 14.38$.

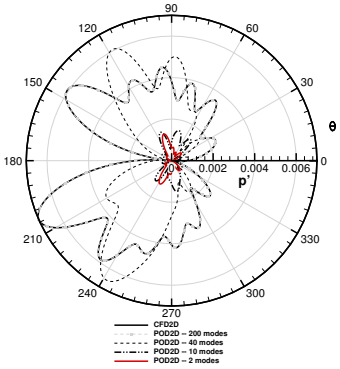

(d) $kc = 18.33$.

Figure 3.11: Acoustic pressure directivity for observer locations at 7.9c above the trailing edge.

in the present analysis. One way to identify if the POD modes carry information of periodical dynamics, which may represent coherent structures, is via the λ_i POD spectrum distribution presented in Fig. 3.8(a). Figure 3.12 highlights the presence of eigenvalues of modes with similar values, typical of coupled modes. POD modes appear in pairs in the eigenvalue distribution analogue to the sine-cosine relation in Fourier modes.

When the POD modes are not present in pairs, or when there is an odd number of eigenvalues with similar energetic levels, the information in the spatial eigenfunctions may not be clearly presented making it impossible to identify coherent structures. As Fig. 3.12 shows, for the present flow configuration, the kinetic energy norm allows a better coupling of the POD modes, especially for the first 8 singular values. On the other hand, the p-mean 2D norm shows that modes λ_1 and λ_2, and λ_6 and λ_7, form pairs with eigenvalues of similar energy levels. However, modes λ_3, λ_4 and λ_5 seem to be uncoupled.

Figure 3.13 shows the spatial eigenfunctions for some of the POD modes from Fig. 3.12 obtained using the pressure norm. Results are presented in terms of the y-momentum component. It is possible to see that POD modes λ_1 and λ_6, which have pairs in Fig. 3.12(b), present a clear vortex wake structure with periodic disturbances. A similar

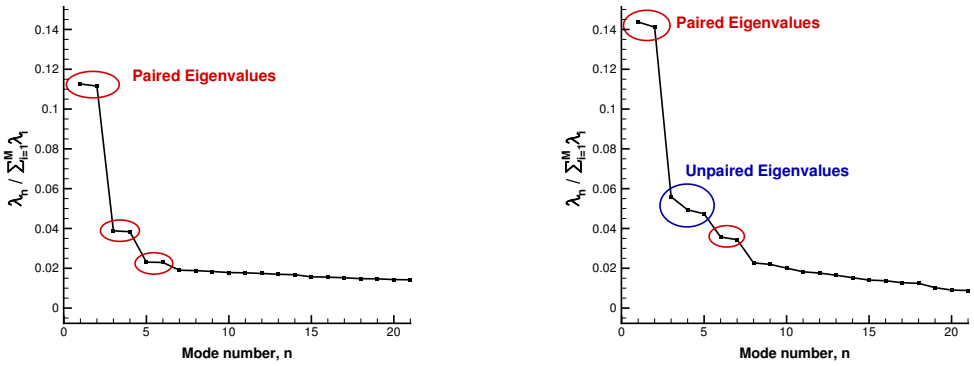

(a) Kinetic energy norm. (b) Pressure norm.

Figure 3.12: POD eigenvalues of the most energy-containing paired modes highlighted in red circles. Unpaired modes shown in blue circles.

alternated pattern of disturbances is also visualized along the turbulent boundary layer region developing on the suction side of the airfoil. On the other hand, POD modes λ_3 and λ_4 show fluctuations which are distorted and without regularity besides some additional noise. This happens since the pressure norm is not able to characterize the structures formed in this part of the energy spectrum, generating uncoupled modes. This result indicates that the pressure norm may not be well suited for identification of coherent structures in the region of the flow comprising the wake and boundary layer. However, it is better suited for the reconstruction of pressure waves propagating to the far-field.

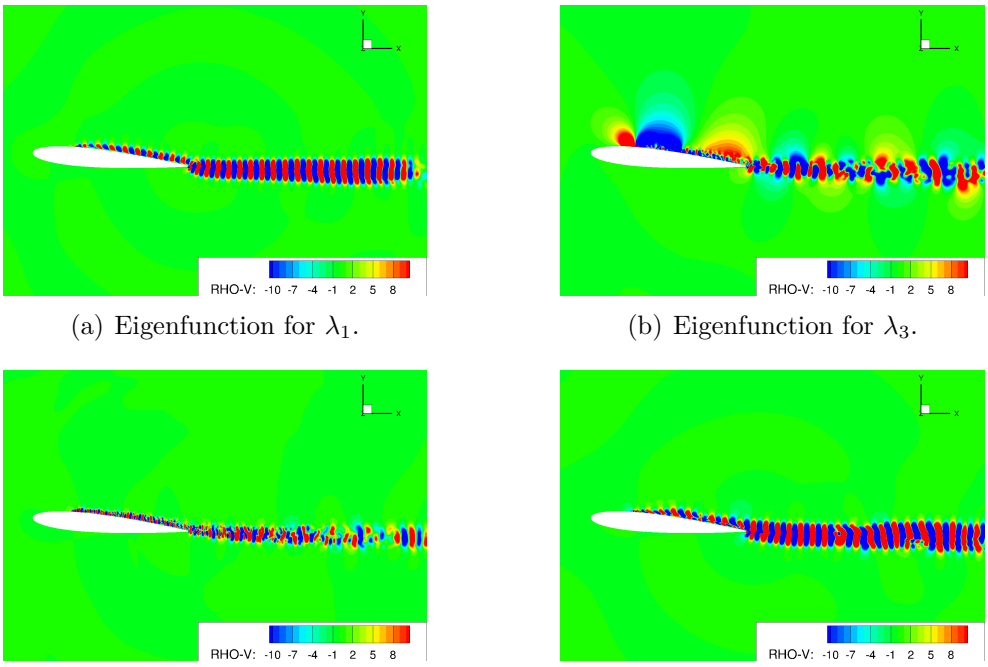

(a) Eigenfunction for λ_1. (b) Eigenfunction for λ_3.

(c) Eigenfunction for λ_4. (d) Eigenfunction for λ_6.

Figure 3.13: Spatial eigenfunctions formed via paired and unpaired modes computed using the p-mean 2D norm.

Figure 3.14 presents the POD modes obtained through the k-mean 2D norm for the y-momentum component. In this figure, one can see that all modes show structures with alternate pattern and which represent coherent structures in the vortex wake. The even POD modes are similar to their counterparts (odd modes). Therefore, for the current case, the k-mean 2D norm presents better results in terms of visualization of coherent structures along the vortex wake. In fact, the first modes shown in the figure seem to have similar wavelengths.

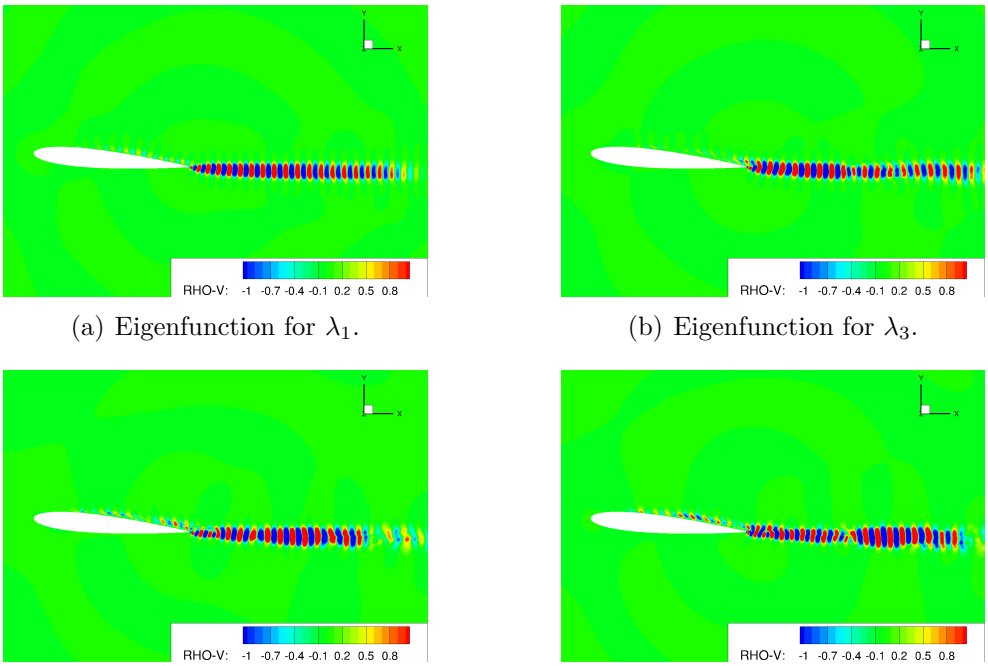

(a) Eigenfunction for λ_1.

(b) Eigenfunction for λ_3.

(c) Eigenfunction for λ_5.

(d) Eigenfunction for λ_7.

Figure 3.14: Spatial eigenfunctions formed via paired eigenvalues computed using the k-mean 2D norm.

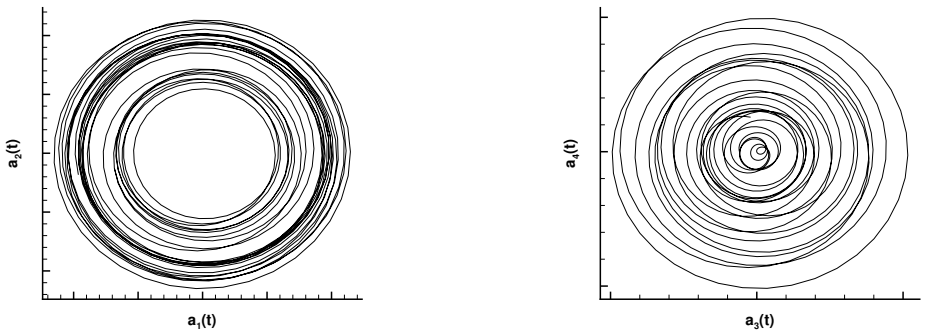

(a) a_1 and a_2.

(b) a_3 and a_4.

Figure 3.15: Phase diagram for time mode amplitudes obtained by the k-mean 2D norm.

Paired modes can be identified by a phase space plot which should describe a harmonic motion. Unpaired modes, on the other hand, should be described by a non-harmonic

motion. Therefore, the paired modes are visually inspected via a harmonic correlation in the phase diagram, which is a laborious process since each pair of modes needs to be identified one by one. Figure 3.15 shows the phase diagram for POD modes obtained using the k-mean 2D norm and one can see that mode amplitudes a_1 and $_2$ are phase related, as well as modes a_3 and a_4. If this relation is well defined, the coherent structures in the spatial eigenfunctions will be also defined, as shown by Fig. 3.14.

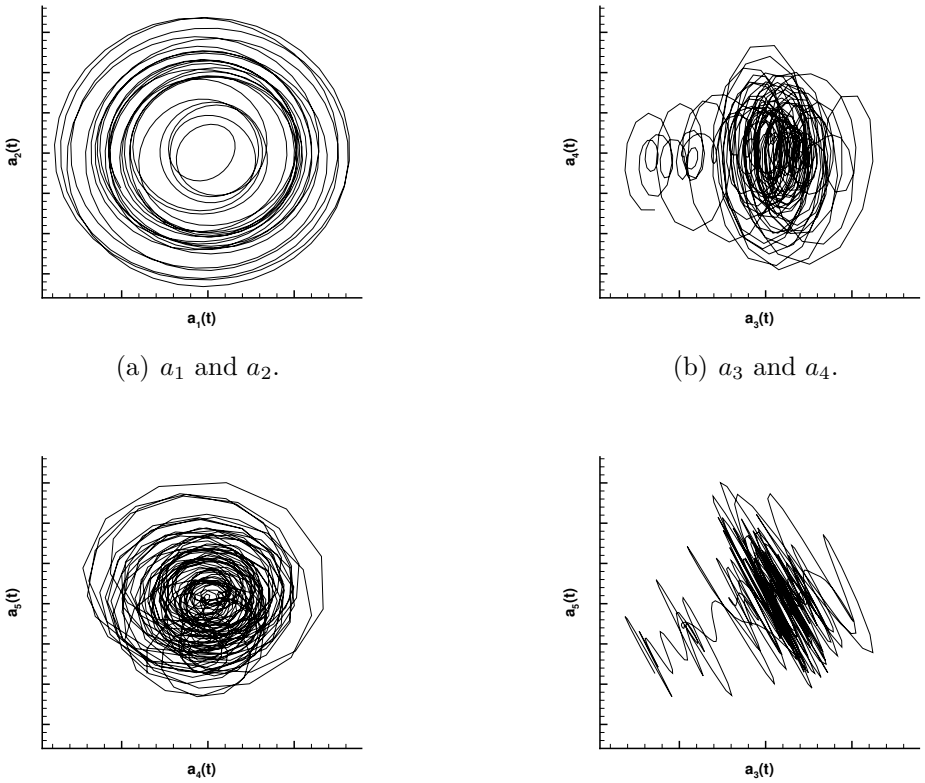

(a) a_1 and a_2.

(b) a_3 and a_4.

(c) a_4 and a_5.

(d) a_3 and a_5.

Figure 3.16: Phase diagram computed for mode amplitudes obtained by the p-mean 2D norm.

The pressure based norm results presented in Fig. 3.16 show that the temporal mode amplitudes a_1 and a_2 are paired, but for mode amplitudes a_3, a_4 and a_5 are not. This should be also observed in the phase diagram computed for these modes. One may notice in Fig. 3.16(a), the phase diagram for modes a_1 and a_2 show the cyclical pattern expected for a periodic structure with strong phase correlation. The phase plots computed for the combinations of modes a_3, a_4 and a_5 present a non-harmonical behavior. This is an indicative of the lack of clarity in the identification of coherent structures in the flow field for these modes. Modes that usually contain coherent turbulence information are presented in pairs and have strong phase correlation.

For all that is stated in this section, it is possible to conclude that the k-mean 2D

norm presents better results for finding coherent structures in the turbulent flowfield. The fist modes capture important physics and are phase related yielding a clear view of the turbulent structures formed near the trailing edge and along the wake. The first pair of POD modes presents the form of an elongated wavepacket starting from the trailing edge region. This pair of modes is present in both kinetic energy and pressure norms with more or less intensity. The second pair of modes obtained by the kinetic energy norm is composed by modes 3 and 4 which also show the wavepacket content near the trailing edge. However, for the pressure norm, modes 3 and 4 are not paired and present some distinct information from each other, including some noise. The presence of large wavepackets will also be shown and discussed in the three-dimensional POD reconstruction.

3.5 General 3D POD Implementation

3.5.1 Parallel Implementation and Computational Cost

The proper orthogonal decomposition is a computational expensive process in terms of both memory allocation and CPU processing. As stated in Section 3.1, the snapshot method computes the correlation matrix for every time frame and, in order to accelerate the computation, the entire numerical data must be saved in the RAM memory.

This becomes extremely expensive when computing high-fidelity simulation cases with millions of degrees of freedom in terms of mesh resolution and hundreds or maybe thousands of time samples. For example, considering the baseline case here analysed which consists of a body-fitted O-grid with $960 \times 125 \times 128$ grid points and a background grid with $896 \times 511 \times 64$ grid points. The simulation is stored for 874 data frames with double-precision in PLOT3D format. Each frame stores five conservative variables including density, x-, y- and z-momentum and total energy. In this case, we have approximately 1.5 Tb of information to allocate in the RAM memory without considering the auxiliary variables, matrices, vectors and integers. A personal computer or even the available high-performance clusters usually do not have such amount of memory available for RAM allocation.

In order to overcome this issue, the standard snapshot method (Sirovich, 1986) was implemented in Fortran in parallel using the standard message passing interface (MPI) for memory partitioning and the open multi-processing (OpenMP) approach for accelerating the computation of the correlation matrix in each partition and process. As shown in Fig. 3.17, the domain is partitioned into one direction only, *i.e.*, a 1D-decomposition in the spanwise direction with one MPI partition per process. Inside each process, the OpenMP

processes compute the correlation matrix and modes in a parallel fashion.

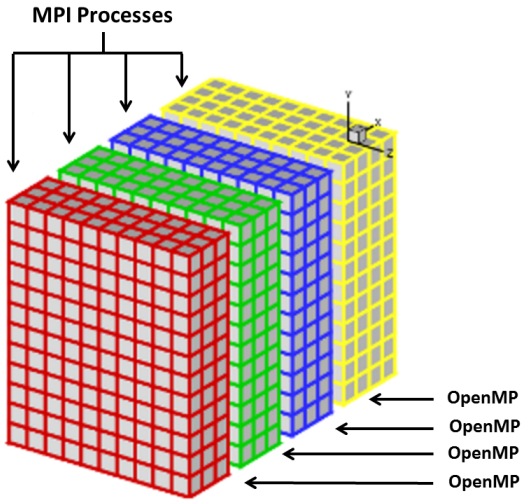

Figure 3.17: MPI domain partitioning example using an one dimensional decomposition for memory usage optimization. The example figure was extracted from Li and Laizet (2010).

The overall process is parallelized in equal sized slices along the spanwise direction and summed up to compute the correlation matrix. Even so, the PLOT3D format is still a barrier because it only allows the access of the entire flow data of a single frame at once. In this way, one MPI process is used to read the entire flow data and, then, it splits the data to the other processes slowing down the procedure. The solution found to deal with this problem was to convert the files to the CFD general notation system (CGNS), a highly recommended format for storing simulation data. The advantage of this format is due to the ability of accessing parts and variables separately. Also, when converting the files, the conservative variables from PLOT3D are converted to primitive variables which makes it possible for accessing each variable separately for the correlation matrix computation without the need of converting them inside the code. In this way, the total memory to be allocated decreases to approximately 290 Gb. In order to obtain a further reduction in the memory usage, the variables are allocated as single precision, which decreases the memory usage to 145 Gb.

The fully parallel code computes the correlation matrix in approximately 6 hours using the entire 874 data files. The computational resources were 8 MPI processes allocating 50 Gb each inside the RAM memory, 1 for each computer node (40 OpenMP processes per node). Without the implemented solutions to speed up the processing, the numerical tool could read only 200 out of the 874 data files due to lack of RAM. Furthermore, the computation of the correlation matrix would be extremely time-consuming. For example, once, using the same computational resources but allocating only 600 snapshots inside the RAM Memory, the correlation matrix computation took 28 hours. The

homogeneous direction consideration (Fourier-POD, in Section 3.7) drastically reduces the RAM memory usage, but does not affect the overall time for the computations. Hence, the current version of the POD implementation is able to reduce both memory and time processing costs.

3.5.2 POD 3D Results

This section presents results obtained by the fully 3D POD reconstruction. One should remind that the original flowfield has a homogeneous spanwise direction. This means that along the spanwise direction, POD modes should correspond to Fourier modes Lumley (1970). In this case, a combination of Fourier and POD could be implemented. However, in this case, we will not force the homogeneous direction to analyze the results of a direct implementation of POD in the full domain. Hence, it will be possible to know how a combination of Fourier decomposition in the homogeneous direction differs from the full-domain POD results.

In order to assess the effects of the physical domains on the POD modes, 4 different reconstructions will be considered. These reconstructions differ in the POD norm used (kinetic energy and pressure) and the simulation domain employed. Many analysis can be performed for POD norms and information domains. Still, there is no definition in literature on what norm is better stated for all possible vector-POD studies. Usually, an analysis of the POD spectrum, the mode coupling and an analysis of the spectral content in the most energetic modes may clarify what physics is covered and uncovered by the use of each norm. Freund and Colonius (2009) found good results for acoustic field reconstruction using pressure-norm and coherent structures in the turbulent jet in the kinetic norm. However, it is not possible to state it is the best application for all situations, specially because of the numerical database used at $M_\infty = 0.9$ and low Reynolds number (Freund, 2001). For a realistic database, the analysis must be taken carefully, not jumping into conclusions, maybe considering the application of many norms for the flow field data to extract useful information for modeling, control and analysis.

Reconstructions obtained using the full computation domain are implemented using kinetic energy (k-3D) and pressure (p-3D) norms. Moreover, the kinetic-energy norm (k-wake) is implemented for a limited portion of the computational domain including only a subset of the domain where turbulent fluctuations are more intense. This region corresponds to the airfoil wake and its suction side boundary layer. The acoustic pressure norm (p-acoustic) is also implemented considering a region of acoustic propagation above the airfoil surface. This subset of the domain was chosen for a region were acoustic waves propagate as pressure fluctuations in a reduced order of magnitude compared to

the turbulent wake region fluctuations. These particular regions of the k-wake and the p-acoustic norms are shown in Fig. 3.18.

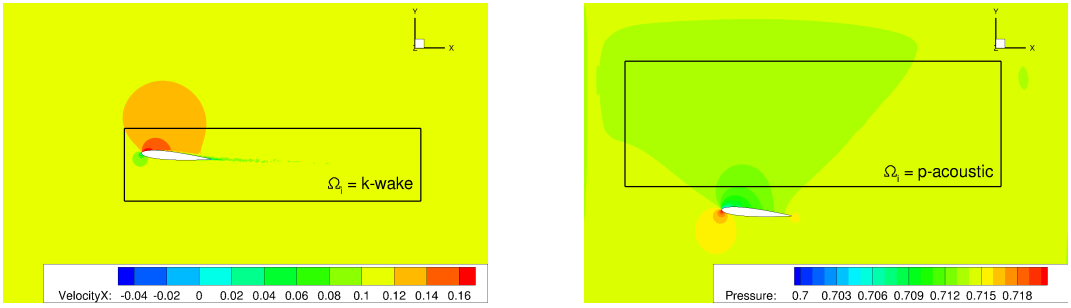

(a) k-wake norm. (b) p-acoustic norm.

Figure 3.18: Limited computational domain regions Ω_i employed for the calculation of the correlation matrix using different norms.

The correlation matrix is computed by a sum of product of correlations among variables over the computational domain employed. Therefore, the summation of variables with low or negligible values should have a small influence in the results. Such observation can be seen in Fig. 3.19 which presents the energy of specific eigenvalues obtained by the k-mean and the k-3D norms. One can see that the energy levels of the modes are very similar although the computational domains employed in the POD mode reconstructions are different. It is clear that the fluctuations of turbulent kinetic energy occur mainly along the airfoil wake and boundary layer regions and, hence, this should be the region of choice for the reconstruction using the kinetic energy norm. At the same time, employing the entire computational domain in the reconstruction does not add much computational cost to the calculations since the grid points are concentrated close to the airfoil and its wake. Therefore, along this section, results will be shown in terms of the k-3D norm which uses the entire data along the computational domain.

Figure 3.20 presents the different correlation matrices computed via the 3 different norms (k-3D, p-3D and p-acoustic). One can notice that the k-3D norm produces a high correlation only for the elements along the main diagonal while the pressure based norms present higher correlations outside the diagonal. In the case of the p-acoustic norm, the correlations are computed along the acoustic field where pressure waves radiate outwards. These pressure waves have higher correlation among themselves which is demonstrated in the correlation matrix.

The different norms affect the way that the eigenvalues group information in the POD spectra as shown in Fig. 3.21(a), and they will also affect the convergence of the POD modes in terms of the energy contribution as shown in Fig. 3.21(b). The k-3D norm presents eigenvalues with smaller energetic content in the first modes. On the other hand, the p-acoustic norm has most of the energy accumulated in the first modes.

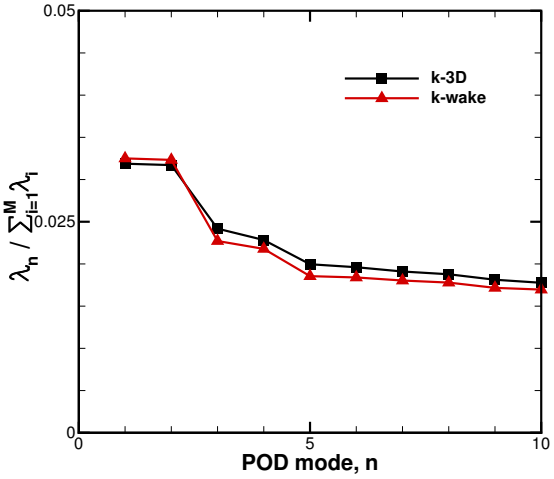

Figure 3.19: Eigenvalues of the full 3D POD reconstructions using the kinetic energy norm along the entire computational domain (k-3D) and only the airfoil wake region (k-wake).

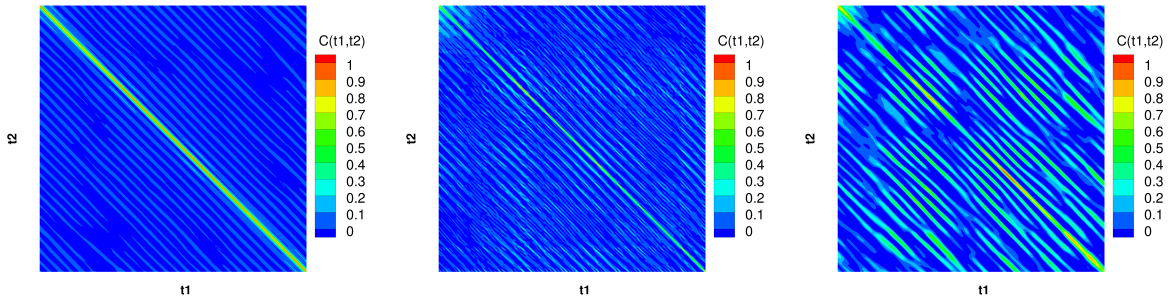

(a) k-3D norm. (b) p-3D norm. (c) p-acoustic norm.

Figure 3.20: Correlation matrices for different POD norms.

Although this norm may recover the total energy with fewer modes, it does not mean that the information contained in the modes provide useful information in terms of physical coherent structures.

As one can see in Fig. 3.21(a), for the three POD norms tested, the first 4 modes seem to be paired, which means that they are phase related as already stated in Section 3.4.2. Figure 3.22 shows the phase diagram for the first 3 pairs of temporal mode amplitudes in order to better evaluate the coupling among them. Results obtained for the first two modes using the k-3D norm present a strong phase relation as can be observed in the circular pattern in the figure. However, mode amplitudes a_3 and a_4, as well as modes a_5 and a_6, show a distorted pattern in the phase diagram meaning that they are not paired and do not represent coherent structures. The p-3D norm presents some phase relation between modes a_1 and a_2 and a_3 and a_4, respectively. One can clearly see that the latter represent structures at higher frequencies than the former since they have more cycles in the phase plot. Modes a_5 and a_6 do not present do not present a phase relation.

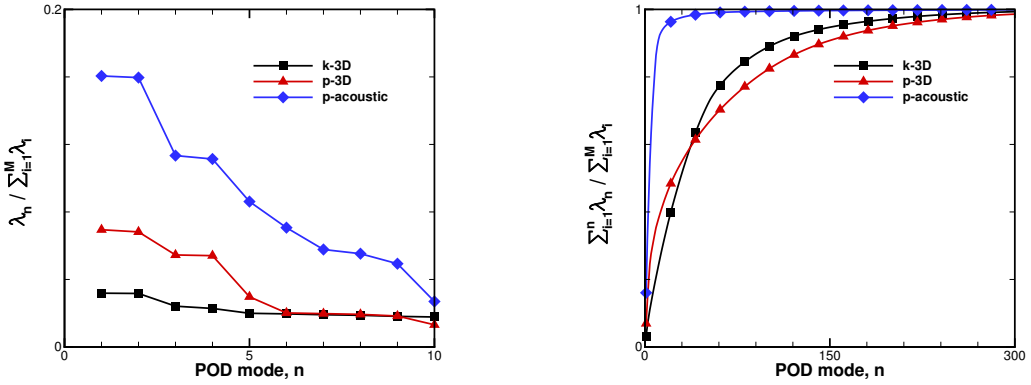

(a) Normalized energy of singular values.

(b) Cumulative energy of normalized singular values.

Figure 3.21: Singular values for 3D implementation of POD using the k-3D, p-3D and p-acoustic norms.

Finally, results obtained by the p-acoustic norm presents a phase relation between mode amplitudes a_1 and a_2 similarly as the results obtained by the other norms. However, the plot shows some distortion in the phase compared to the other norms, especially the k-3D norm. Similar results are obtained for modes a_3 and a_4, which may contain information about coherent structures. As observed for all norms, modes a_5 and a_6 obtained by the p-acoustic norm do not present a clear phase relation.

The phase relation is computed using the temporal coefficients of the individual POD modes. In Fig. 3.23, one can analyze the behavior of the temporal coefficients obtained using the p-3D norm. Figures 3.23(a), (b) and (c) present the temporal evolution of the coefficients and results show that mode amplitudes a_1 and a_2 are related by a phase shift. A similar observation can be made for modes a_3 and a_4, which have a higher frequency dynamics. However, the temporal behavior of modes a_5 and a_6 do not show any clear phase relation, as expected. In Figs. 3.23(d), (e) and (f), one can see the amplitudes of the Fourier transformed temporal coefficients in logarithmic scale. It is possible to notice that the first two modes are responsible for fluctuations in the tonal peak frequency at Helmholtz number $kc \approx 9$. One should remind that this tonal peak dominates the acoustic radiation in the farfield as observed by Wolf *et. al* (2012) and it is caused by a energetic coherent structure such as vortex shedding. In Fig. 3.6, a tonal acoustic peak is presented at $k \approx 8.5$. Aeroacoustic sources in the form of quadrupoles suffer noise scattering along the airfoil surface. In this case, it is possible to conclude that the first two POD modes represent the aeroacoustic sources responsible by the tonal noise observed. The second pair of modes excite higher frequencies and present a broad-tonal peak at $kc \approx 25$. The oscillation at higher frequencies was already noticed in Fig. 3.22(e), where the phase diagram presents several cycles. The third pair of modes present broadband spectra with

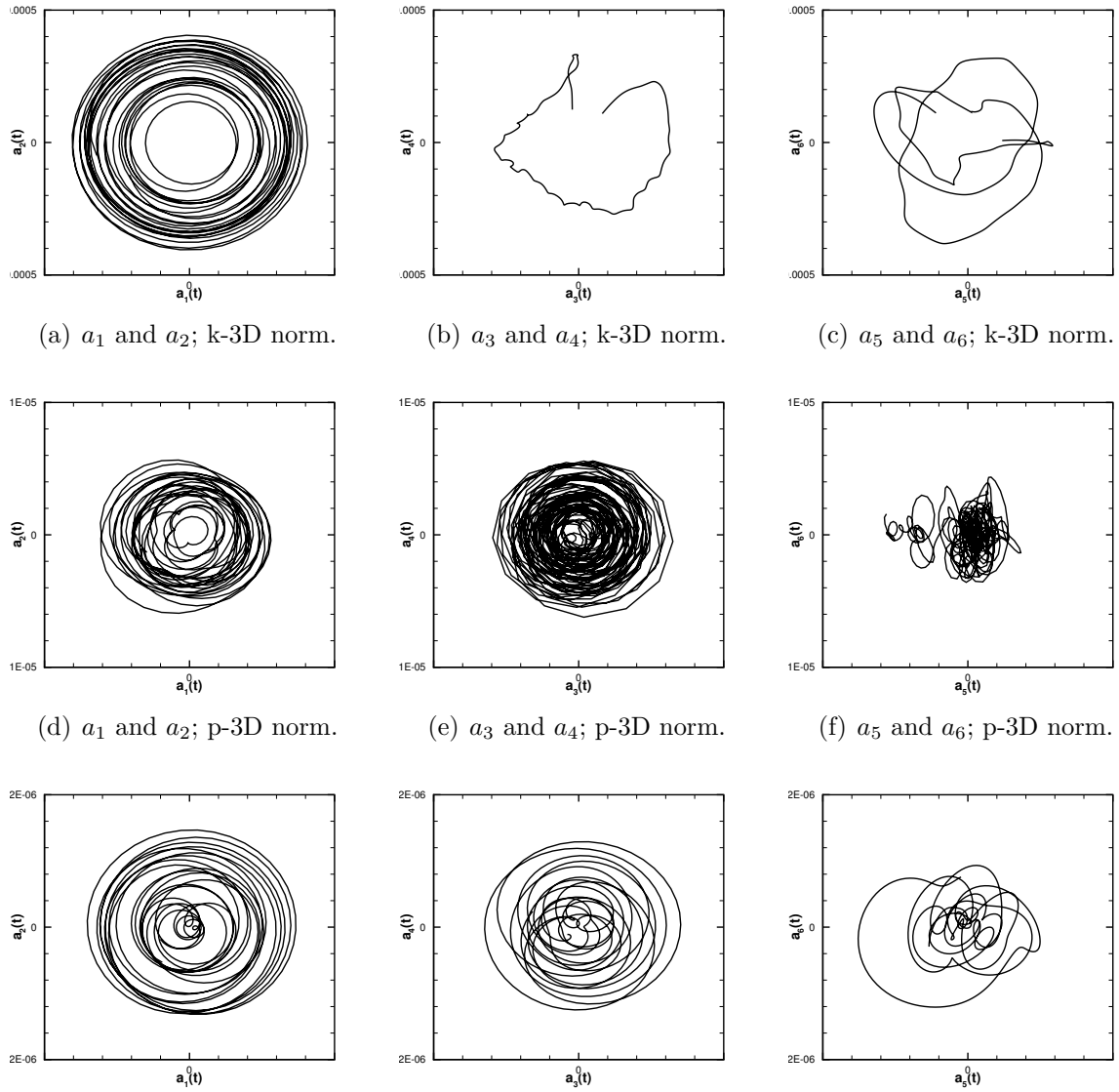

(a) a_1 and a_2; k-3D norm. (b) a_3 and a_4; k-3D norm. (c) a_5 and a_6; k-3D norm.

(d) a_1 and a_2; p-3D norm. (e) a_3 and a_4; p-3D norm. (f) a_5 and a_6; p-3D norm.

(g) a_1 and a_2; p-acoustic norm. (h) a_3 and a_4; p-acoustic norm. (i) a_5 and a_6; p-acoustic norm.

Figure 3.22: Phase diagrams for POD modes computed using different norms. Circular patterns represent significant phase relation between mode pairs.

different levels and, therefore, confirm the previous analysis which assumed they had no phase relation.

From previous analysis, we assume that the first POD modes are associated to coherent structures which generate noise at the tonal peak frequency. However, we cannot say that the only modes that contribute to the tonal noise frequency are those from the first pair and we presume that other modes may also contain information related to that frequency. The different norms studied here capture approximately the same dynamics for the first pair of modes. However, it is possible to see small differences among the results in terms of the eigenfunctions which are representative of the spatial components of the modes. Figures 3.24 and 3.25 show detail views of the spatial modes along the boundary layer

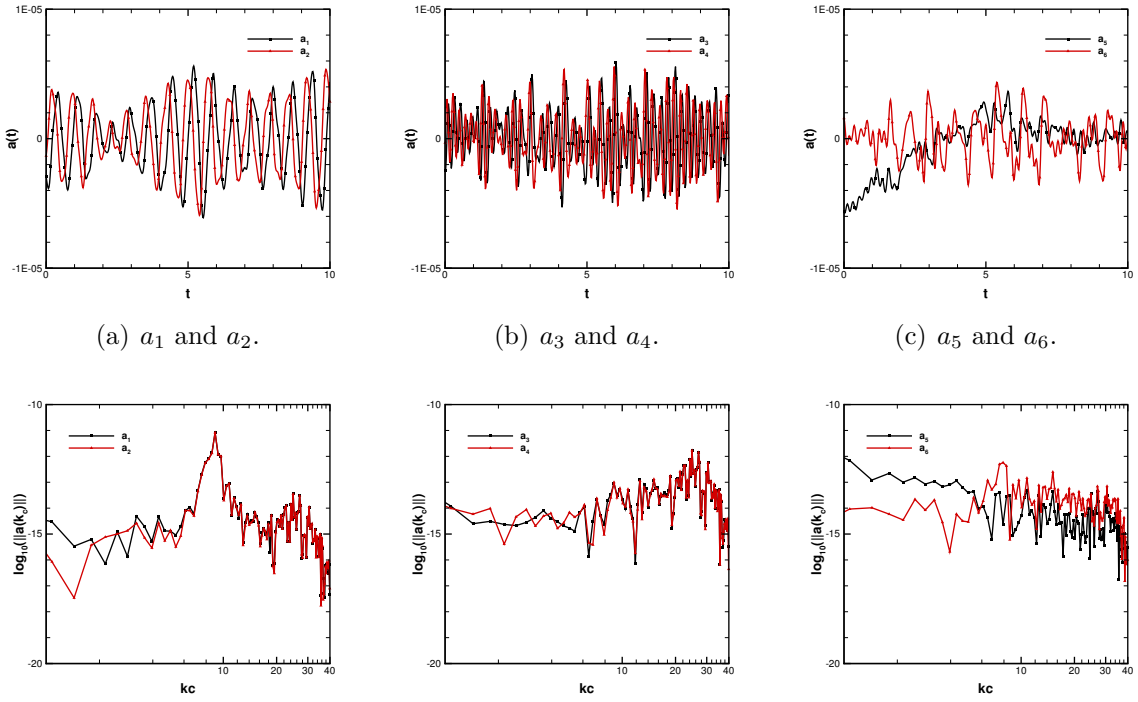

(a) a_1 and a_2. (b) a_3 and a_4. (c) a_5 and a_6.

(d) a_1 and a_2. (e) a_3 and a_4. (f) a_5 and a_6.

Figure 3.23: Dynamics of temporal coefficients for different POD modes obtained by the p-3D norm in the time domain (a,b,c) and Fourier domain (d,e,f).

and wake regions, respectively. In these figures, one can observe the spatial distribution of the first POD mode for the three norms investigated here. Both the k-3D and p-3D norms computed using information along the entire computational domain present clear alternating coherent structures which can be visualized in terms of the y-component of velocity. On the other hand, when the spatial modes are obtained using p-acoustic norm, one can see some additional noise in the velocity components, especially along the wake region. Although the p-acoustic provides a faster convergence in terms of energy levels for the singular values, its application to the nearfield turbulence fluctuations is not able to decompose the coherent turbulent structures. The other norms which form the correlation matrices using nearfield information can provide a clearer identification of such structures, which is a desirable property for the study of turbulence.

Figure 3.24 shows that coherent structures are formed just after the suction-blowing tripping mechanism that induces transition in the suction side of the airfoil. The scale of the plots are adjusted for the different norms in order to present equal-sized coherent structures for each figure. In this analysis, only small differences are perceived between the k-3D and p-3D norms, but the p-acoustic norm is clearly different from the others. The presence of 2D elongated structures in the spanwise direction is present in the p-acoustic norm eigenfunctions, but they appear with larger rollers which differ from those observed in the other norms. In Fig. 3.25, one can see the development of large 2D elongated

coherent structures after the flow passes the trailing edge and the differences between the k-3D and p-3D norms are small. The p-acoustic norm presents instabilities in the vortex wake which contaminate the 2D structures.

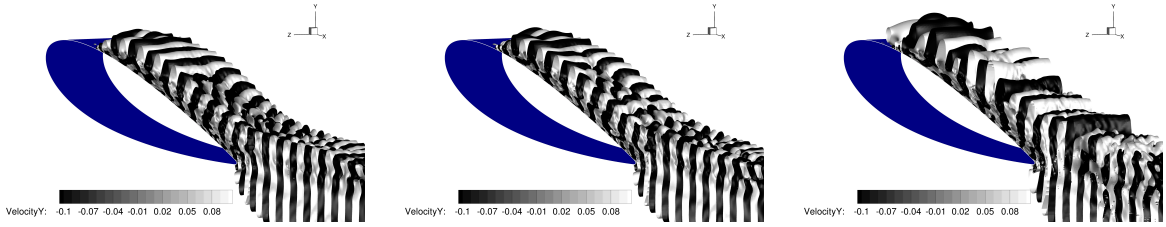

(a) k-3D norm. (b) p-3D norm. (c) p-acoustic norm.

Figure 3.24: Isosurfaces of y-component of velocity reconstructed using eigenfunctions for POD mode λ_1 for different norms along the airfoil surface. Airfoil surface in blue.

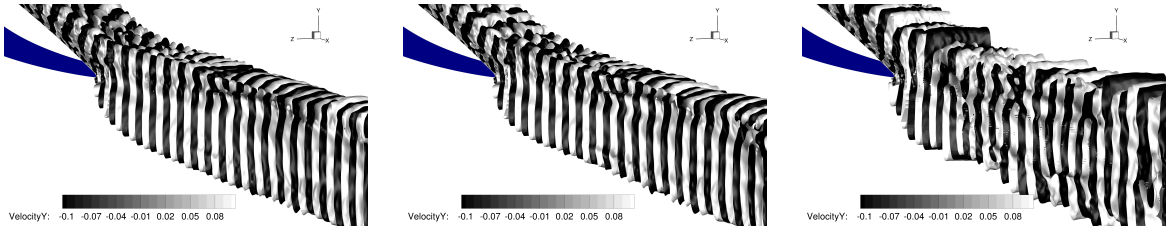

(a) k-3D norm. (b) p-3D norm. (c) p-acoustic norm.

Figure 3.25: Isosurfaces of y-component of velocity reconstructed using eigenfunctions for POD mode λ_1 for different norms along the wake region.

There is a considerable difference between the results obtained by different norms for the second pair of modes. Previous results showed that the second pair of modes computed using the kinetic energy norm are not coupled. Figure 3.26 shows the spatial eigenfunctions for mode λ_3 from this norm. This POD mode carry part of the energy content required to reconstruct the original turbulent flowfield. The non-coupled modes are not further studied in literature but, due to the physics observed for the current baseline case, they may be related to convection of the coherent structures in the streamwise direction. In the present case, Fig. 3.26(a) shows the presence of large streamwise structures, however, they are distorted and are hard to be identified. Fig. 3.26(b) shows that these eddies does not affect the acoustic waves propagated in the nearfield.

The p-3D and p-acoustic norms have coupled modes in the second pair and their eigenfunctions are presented in Fig. 3.27. The scale is once again adjusted for better visualization of the spatial modes but, in this case, it is not possible to observe coherent structures of similar wavelengths. The second pair of modes presents more higher frequency coherent structures in the suction side of the airfoil and in the vortex wake region near the trailing edge, especially for the p-3D norm. In this case, Fig. 3.23(e) shows thin

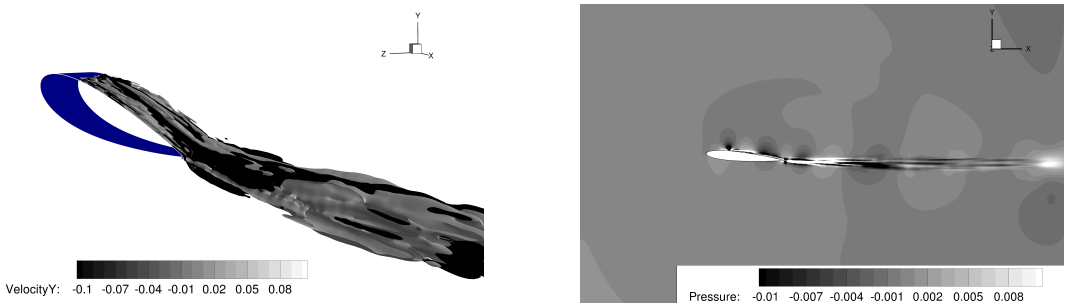

(a) Velocity-Y. (b) Contours of pressure component.

Figure 3.26: Visualization of the spatial eigenfunction for POD mode λ_3 computed using the k-3D norm. (a) Isosurfaces, airfoil surface in blue; (b) mid-span plane.

elongated 2D structures with considerable background noise. These structures may be related to high frequency noise generation by poorly correlated turbulent structures. For the p-acoustic norm, one can notice larger structures in the figure that shows the spatial components for the third mode. However, these structures still present some distortions and background noise. For this case, the second pair of modes is capturing structures that may be related to the physics described by the first pair of modes but which were not contained by them in the eigenvalue decomposition.

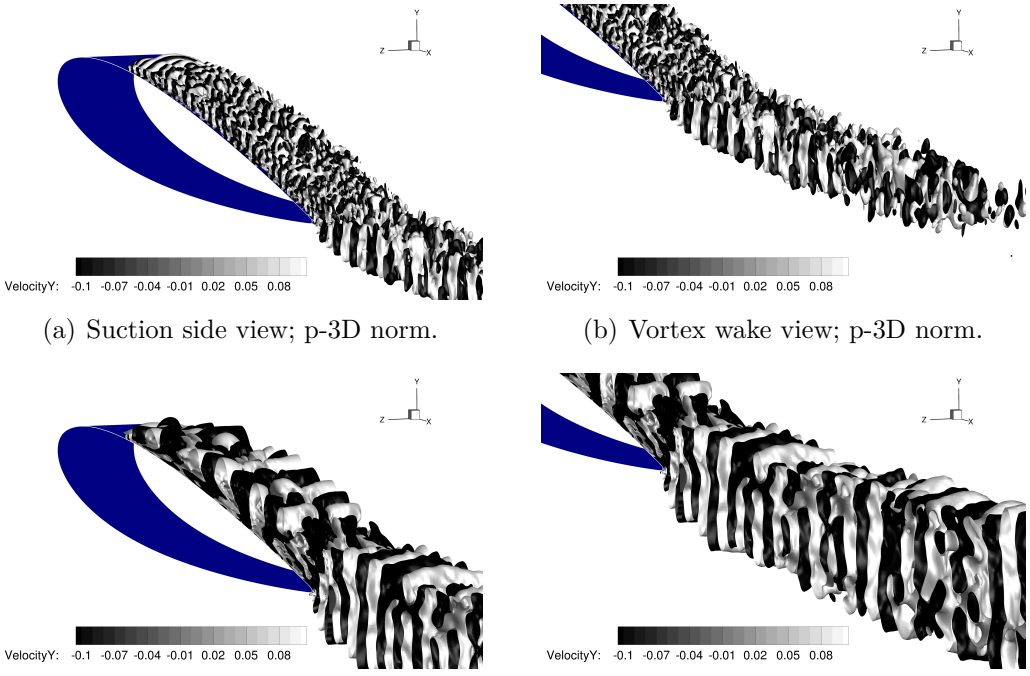

(a) Suction side view; p-3D norm. (b) Vortex wake view; p-3D norm.

(c) Suction side view; p-acoustic norm. (d) Vortex wake view; p-acoustic norm.

Figure 3.27: Isosurfaces of y-velocity component reconstructed using the eigenfunctions for POD mode λ_3 for different norms.

The direct implementation of POD, without considering the present homogeneous flow direction along the airfoil span is computationally expensive. Moreover, the results obtained by different POD norms can be contaminated by the information from different

modes. In order to obtain improved results, one can use spatial filters such as Fourier decomposition along the homogeneous direction or time spectral filters for the correlation matrix. The current section is still important to show how a direct implementation of the full 3D POD reconstruction can be performed. For fully 3D flows, without homogeneous directions, this may be the only implementation possible and one should be aware of the challenges which appear in the POD reconstruction. Moreover, the current section is also important since the results presented will serve as a basis for comparison with other 3D POD reconstructions obtained using filters and other techniques.

3.6 Spectral POD

From the previous analysis of the POD temporal and spatial modes, it is possible to say that the total energy of the flow reconstruction may not be well distributed along the POD spectrum. Such issue results in uncoupled modes which, as shown in Sections 3.4.2 and 3.5.2, may not represent physical coherent structures that can be identified by visual inspection of the spatial eigenfunctions or temporal modes. Thereby, it is important to obtain as many coupled modes as possible to organize the POD spectrum in order to better identify the coherent structures present in the turbulent flow and to perform an energy assessment contained by these structures.

In this way, it is possible to consider applying a filter in the correlation matrix, which acts a transition between POD and DFT. This technique is called spectral proper orthogonal decomposition (SPOD), it was first proposed by Sieber *et. al* (2016) and it consists of a filtering applied to the correlation matrix prior to the SVD. This process conserves the total energy of the flow redistributing the energy along the POD spectrum through specific frequencies. As observed in the previous section, the POD modes are built based on energy and a specific mode usually contains information of structures at different frequencies. In the SPOD, modes are also constructed based on energy but the filtering process of the correlation matrix allows the reconstruction of most energetic modes at particular frequencies.

The filter is applied according to Eq. 3.12 to the correlation matrix $\mathbf{C}$ resulting in a new correlation matrix $\bar{\mathbf{C}}$ which has increased diagonal similarity. The general POD methodology is not altered according to Section 3.1 and the presence of the filtering is formed by three important parameters: the window function of the filtering (g_k), the N_f integer scalar value that represents the size of the window, and the periodic or non-periodic considerations about the time series in the correlation matrix. The periodicity is considered over the boundaries of the correlation matrix when the N_f parameter must account to points outside the matrix. The periodic considerations in

the time series leads to a periodic correlation matrix. In this way, when the N_f parameter accounts for points outside the matrix, they must be mirrored with respect to inner terms of the matrix. When the time series is non-periodic, the points outside the matrix correlation can be zeroed.

$$\bar{C}_{i,j} = \sum_{k=-N_f}^{N_f} g_k C_{i+k,j+k} \tag{3.12}$$

The three main parameters described previously will be analyzed using the two main POD norms investigated before: the kinetic energy and pressure norms employed along the entire flow field, k-3D and p-3D norms, respectively. The p-acoustic norm is not considered here due to its considerable signal-to-noise ratio. For the sake of simplicity in the analysis and to investigate the effects of the fully three-dimensional SPOD implementation, the studies will not consider the homogeneity of the spanwise direction, *i.e.,* we are performing a direct full domain 3D SPOD reconstruction.

3.6.1 Filtering Function and Window Size

Several filtering functions can be applied to the correlation matrix in order to obtain optimum spectral response. The filtering functions applied in the present work are the square filter represented by $g_k = 1/(2N_f + 1)$, and the smooth response optimized Gaussian filter (Pope, 2001) represented by $g_k = e^{8k^2/N_f^2}/\sum g_k$. The advantage of the Gaussian filtering is the smooth spectral response as shown in Fig. 3.28 which presents the Fourier response of the square and Gaussian functions. One can notice that the Gaussian filtering is less sensitive to changes in the window size and, hence, it provides an enhanced control in the response of the SPOD compared to the square filter. The latter shows a fast decay in the frequency response.

For the coupled modes, the relation shown in the phase diagrams using the temporal POD coefficients is a harmonic correlation. For the uncoupled modes, one could see that no phase relation could be observed. SPOD can improve the phase relation of POD modes through coupling. This way, uncoupled modes can be coupled and the phase relation of already coupled modes can also be improved. For example, let us consider the evolution of the first two temporal modes shown in the phase diagram of Fig. 3.29. The total time of the recorded data corresponds to 874 frames which gives a total non-dimensional time of $t = 17.46$. One must remind that the time scale is obtained using the chord length and the freestream speed of sound as characteristic length and velocity scales. Figure 3.29 shows how the harmonic correlation develops in time for the general 3D implementation of the POD using the k-3D norm. In a similar fashion, Fig. 3.30 presents the harmonic correlation for the same pair of modes computed by the SPOD technique using a square

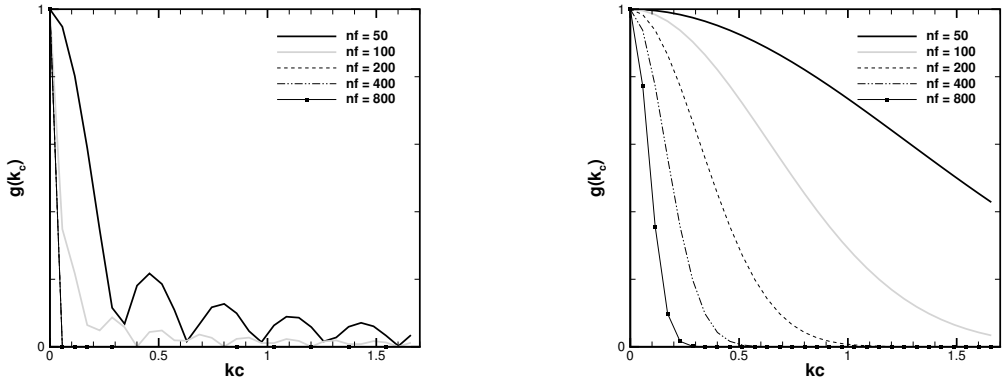

(a) Square filter. (b) Gaussian filter.

Figure 3.28: Normalized spectral response of the square and Gaussian filtering functions for different window sizes N_f.

window filtering with $N_f = 800$ and the same k-3D norm.

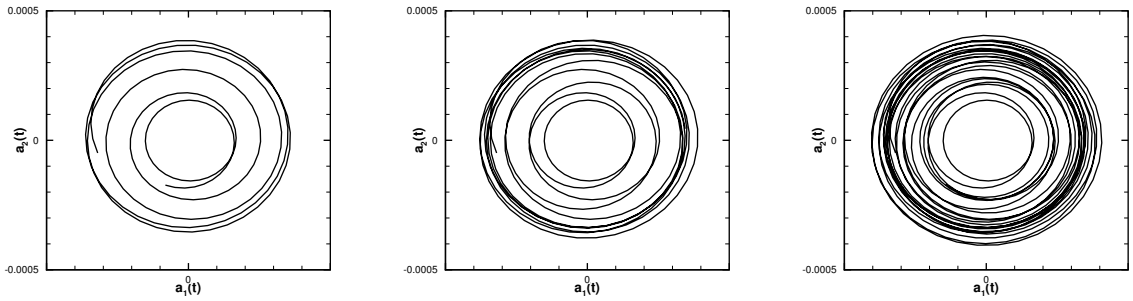

(a) $t \approx 4$. (b) $t \approx 8$. (c) $t \approx 16$.

Figure 3.29: Phase diagram showing the temporal evolution of POD modes 1 and 2, represented by a_1 and a_2, obtained using the k-3D norm.

The major difference between Figs. 3.29 and 3.30 is that the latter presents more organized phase patterns as they evolve in time. Figure 3.29 shows a growth in amplitude of the temporal modes with some harmonic synchronization. However, the modes still have some intersection points representing that there are multiple frequencies represented in the mode pair and that their mode coupling is not well stated in the POD spectrum. Figure 3.30 presents a cleaner harmonic correlation in the first pair of modes showing that their coupling is well determined and the coherent structures in its eigenfunction will be better represented. As the SPOD with square window filtering has a faster transition to DFT, as shown in Fig. 3.28, the representation with $N_f = 800$ is approximately the same as employing a DFT for this case.

In Fig. 3.31 it is possible to see how the SPOD technique filters the information of the mode amplitudes as the window size N_f is increased. The square window is applied in this case and one can notice that the SPOD not only filters information but redistributes

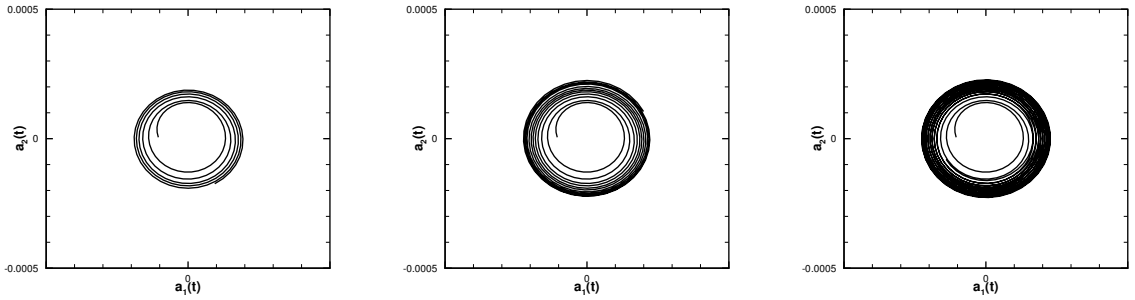

(a) $t \approx 4$. (b) $t \approx 8$. (c) $t \approx 16$.

Figure 3.30: Phase diagram showing the temporal evolution of SPOD modes a_1 and a_2 obtained using the k-3D norm. A square window filtering is applied with $N_f = 800$.

the information in the temporal modes creating a wavepacket structure that increases and decays along the time span. Also, the highest point in the mode amplitudes is exactly in the middle of the temporal signal. As the window size increases, the energy of the wavepacket decreases and the oscillations have lower magnitude. This means that the energy of the first pair of modes has been spread along the POD eigenvalue spectrum.

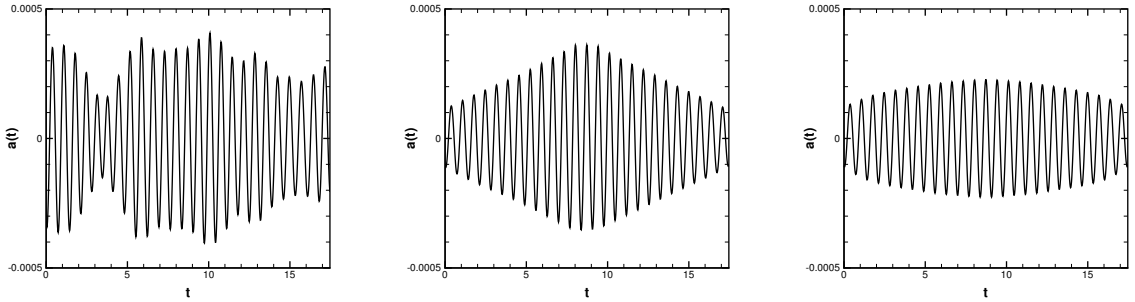

(a) $N_f = 0$. (b) $N_f = 400$. (c) $N_f = 800$.

Figure 3.31: Evolution of temporal mode a_1 obtained with k-3D norm and square-box filtering with different window sizes N_f.

Figures 3.32 and 3.33 present spectra of the first temporal mode computed using the square-box and Gaussian filtering functions in the SPOD method, respectively. In Fig. 3.32(a), one can see the spectrum for the first POD mode without the application of any filtering. As the square filter is applied in Figs. 3.32(b) and (c), the broadband content of the spectra become cleaner and the tonal peak at $kc \approx 8.5$ is better characterized.

In this case, the low frequency tones are smoothed out and the high frequency content has a faster amplitude decay. However, as shown in Fig. 3.28, the square-box filtering may affect other frequencies that represented by the physics in the POD mode and so, the spectrum shows a minor noise in the signal, especially at low frequencies.

Spectra of the first temporal mode are shown in Fig. 3.33 for the Gaussian filter applied with different values of N_f. Results are smoother than those presented in Fig. 3.32 since the Gaussian filtering has a more controllable frequency response, as shown in Fig. 3.28.

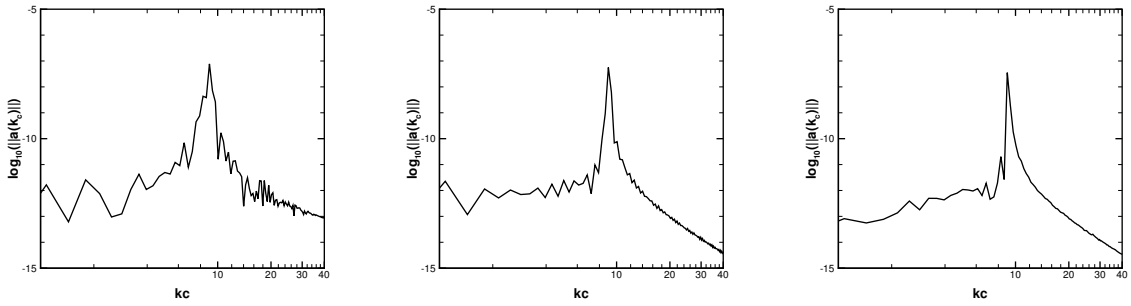

(a) $N_f = 0$. (b) $N_f = 400$. (c) $N_f = 800$.

Figure 3.32: Spectra of 1st temporal mode a_1 obtained by the k-3D norm and square-box filtering SPOD with different window sizes N_f.

The Gaussian filter has improved results presenting less noise for all frequencies, especially in the low frequency regime which does not show oscillations. In this case, the Gaussian filtering presents a smoother transition between POD and DFT.

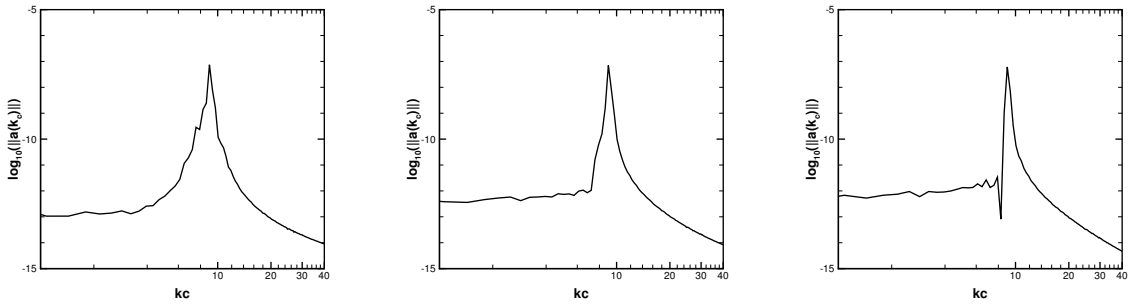

(a) $N_f = 200$. (b) $N_f = 400$. (c) $N_f = 800$.

Figure 3.33: Spectra of 1st temporal mode a_1 obtained by the k-3D norm and Gaussian filtering SPOD with different window sizes N_f.

Similarly to the square-box function, the Gaussian filter also improves the harmonic correlation in the first pair of modes obtained by the k-3D norm, as shown in Fig. 3.34. Even so, the SPOD cannot guarantee that coherent structures are clearly represented along the entire POD spectrum, unless when the transition to DFT is complete and only for those modes with considerable signal-to-noise ratio.

An example where the phase diagram is improved by the Gaussian filter employed in the SPOD technique, but still the mode pair is not fully coupled, can be seen Fig. 3.35 which shows the phase diagram for the second mode pair obtained by the k-3D norm. It is possible to see that the modes oscillate at some lower frequency, but the harmonic correlation is not well represented. At lower frequencies, only large window sizes can present good harmonic correlation and, in this case, the SPOD technique is not very useful as the DFT would present the same results. One should remind that, for the present numerical simulations, statistical convergence is not obtained for the low frequency content of the spectrum. For this portion of the spectrum to be well captured,

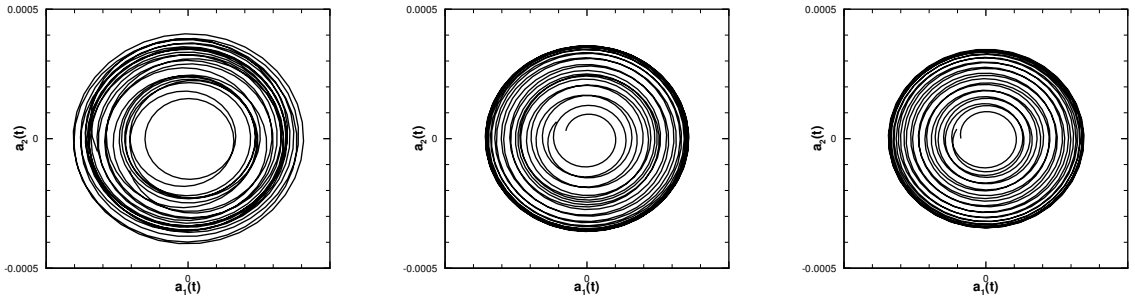

(a) $N_f = 0$. (b) $N_f = 400$. (c) $N_f = 800$.

Figure 3.34: Phase diagram of the 1st POD mode pair obtained by the k-3D norm with Gaussian filtering for different window sizes N_f.

the simulations would have to be run for a much longer time considerably increasing the computational cost of the simulation and the data storage requirements. Furthermore, the tonal frequency of interest here is in the mid-frequency portion of the spectrum, which is statistically well-captured.

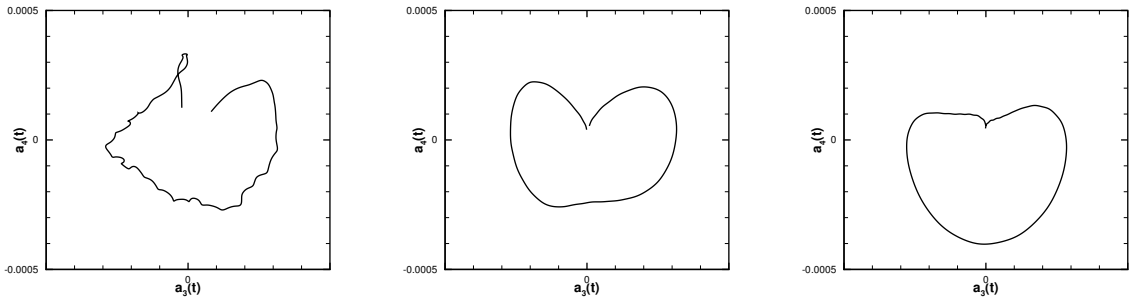

(a) $N_f = 0$. (b) $N_f = 400$. (c) $N_f = 800$.

Figure 3.35: Phase diagram of the 2nd mode pair (a_3 and a_4) obtained by the k-3D norm with Gaussian filtering for different window sizes N_f.

The previous analysis of the filtering functions and window sizes were obtained using the turbulent kinetic energy norm, k-3D, along the entire computational domain. Here, we will present a similar investigation in terms of phase diagrams and spectra using the pressure norm, p-3D. In Sec. 3.5.2, Fig. 3.22 presents the harmonic correlations for the 3 first mode pairs obtained by the standard POD technique for different POD norms. It was also shown that the p-3D norm has a stronger harmonic correlation for the second mode pair than for the first mode pair.

Figure 3.36 presents the spectrum of the temporal modes for mode amplitude a_1 obtained by the p-3D norm and the Gaussian filter with different window sizes, N_f. Differently from the k-3D norm, for the pressure norm, higher noise levels are observed at high frequencies when the standard POD technique is employed. When the SPOD method is applied, the oscillations at low frequencies vanish and only small oscillations appear in the high frequency content of the spectrum. The application of the Gaussian

filter with $N_f = 400$ cleans the spectrum leaving a well-defined tonal peak at the $kc \approx 9$ frequency.

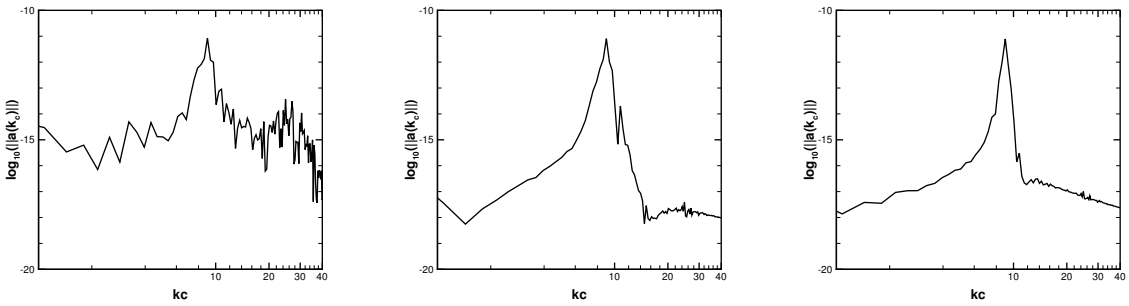

(a) $N_f = 0$. (b) $N_f = 200$. (c) $N_f = 400$.

Figure 3.36: Spectra of 1st temporal mode obtained by the p-3D norm and Gaussian filtering with different window sizes N_f.

An analysis for the third mode amplitude a_3 is presented in Fig. 3.37 using the same parameters as for the first mode a_1. One can see that when the filtering is not applied, the energy is spread along several frequencies with a tonal peak at $kc \approx 25$. From Fig. 3.37(a), it is impossible to define a particular frequency for the third mode. However, when the SPOD technique is employed, the energy is redistributed in the correlation matrix and the spectrum shows a tonal peak at a lower frequency, similar to that observed for the first POD mode. This tonal frequency is in the same frequency band where the tonal acoustic peak occurs in Fig. 3.6. In this case, the third SPOD mode is representative of the aeroacoustic sources that compose the tonal peak noise sources in the current airfoil noise problem. On can notice that the SPOD technique distributes the energy of the flow in the POD spectrum. The second mode pair from SPOD contains flow information related to lower frequencies than those presented in the non-filtered POD spectrum.

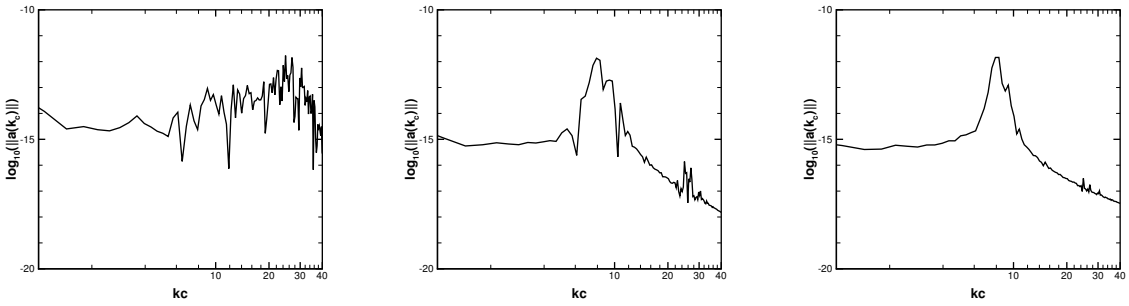

(a) $N_f = 0$. (b) $N_f = 200$. (c) $N_f = 400$.

Figure 3.37: Spectra of 3rd temporal mode a_3 obtained by the P-3D norm and gaussian filtering with different window sizes N_f.

Figure 3.38 shows the phase diagram and the harmonic correlation of the second mode pair obtained by the p-3D norm and the Gaussian filtering. One can see the significant

improvement in the harmonic correlation for this mode pair compared to the standard POD technique. That means that the energy region where the second mode pair is comprised in the non-filtered POD is different from that presented in the filtered SPOD method. The non-filtered spectrum for the first POD mode presents a tonal peak but it also has high energy at other frequencies in the spectrum. The Gaussian filtering in the SPOD redistributed the energy in the POD spectrum. Now, both the first and second mode pairs represent the physics originally contained in the first pair of unfiltered POD modes. The information at high frequencies does not disappear but it is now related to another region of the filtered POD spectrum, for example, in the third mode pair obtained by the p-3D norm.

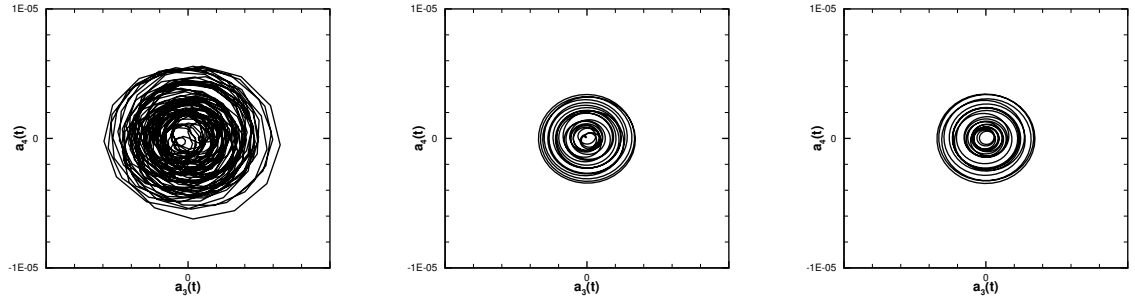

(a) $N_f = 0$. (b) $N_f = 200$. (c) $N_f = 400$.

Figure 3.38: Phase diagram of the 2nd mode pair obtained by the p-3D norm and Gaussian filtering for different window sizes N_f.

The phase diagram results obtained for the third pair of modes are presented in Fig. 3.39. This figure shows that the non-filtered POD has no harmonic correlation and, therefore, no useful information in terms of coherent structures since it contains a considerable noise-to-signal ratio. The SPOD technique employed using the Gaussian filtering is capable of presenting useful information at high frequencies and, with a window size $N_f = 200$, the harmonic correlation is already considerably improved.

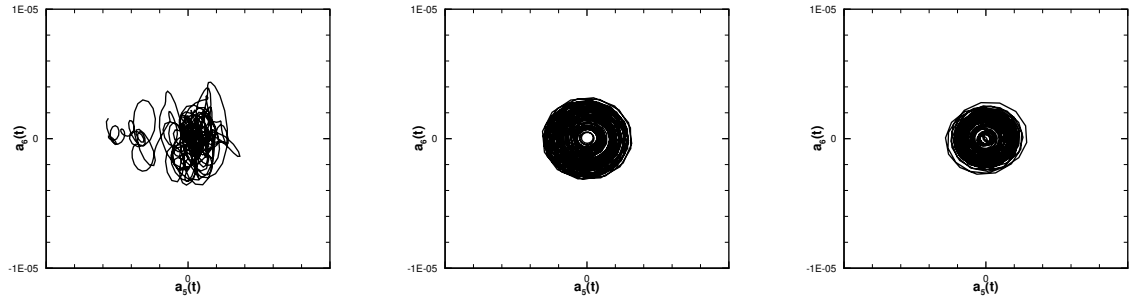

(a) $N_f = 0$. (b) $N_f = 200$. (c) $N_f = 400$.

Figure 3.39: Phase diagram of the 3rd mode pair obtained by the p-3D norm and Gaussian filtering for different window sizes N_f.

As the SPOD affects the POD spectrum redistributing spectral energy over the POD modes, it is expected that the energy convergence becomes slower when SPOD is used. The total turbulent flow energy is spread along the spectrum which gives mode pairs containing less energy than before. Although this is undesirable if the main interest is in ROM or data compression, it can imply significant improvements in the analysis of coherent structures and turbulent flow decomposition. In this case, the eigenfunctions will present well-defined turbulent structures and the SPOD modes will have information closely related to a single or a narrowband of frequencies, making it easier to understand the turbulent flow field.

The POD eigenvalue spectrum for the first 10 POD modes is shown in Fig. 3.40 obtained by the Gaussian filtering with $N_f = 0$, 200 and 400. In these cases, the increase in the window size N_f decreases the energy contained in the first mode pair. However, one can notice that the SPOD filtering helps in flattering the POD spectrum, improving the mode coupling for both POD norms. The k-3D norm is less sensitive to the filtering process, but the p-3D norm suffers great reduction in the energy contained in the POD modes. The second pair of modes in the p-3D norm decays considerably in terms of the energy content compared to the non-filtered case. This is also represented by the results in Figs. 3.37 and 3.38 which show that the information contained in the second pair of modes is completely changed due to the application of the spectral filtering. The k-3D norm presents the re-distribution of the flow energy and, for some POD modes, the energy contained in the mode pair for the SPOD is higher than the non-filtered POD. This is caused by the flattering effect on the SPOD spectrum, which re-distributes the energy and helps in coupling the POD modes.

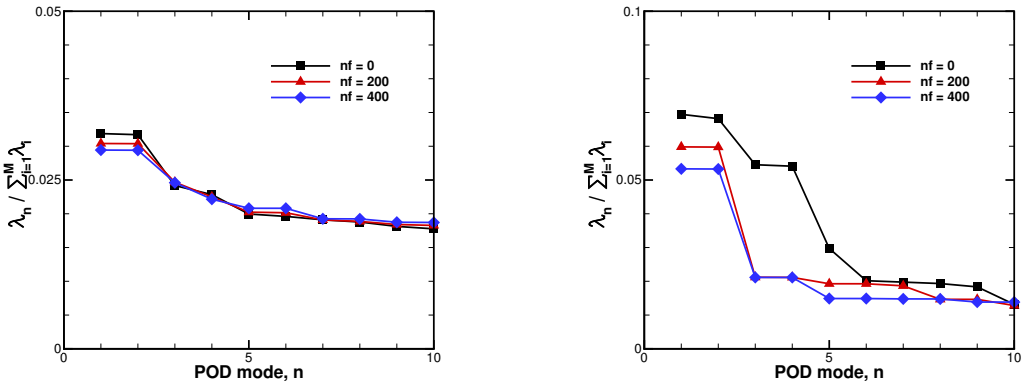

(a) k-3D norm.

(b) p-3D norm.

Figure 3.40: Normalized singular values for different window sizes N_f in the Gaussian filtering.

In Figure 3.41, the correlation matrix for the p-3D norm is shown and the effect of increasing the diagonal similarity is clearly noticed when different window sizes are

applied in the filtering procedure. The DFT approach increases dramatically the diagonal similarity, but the window size is large enough to affect the main diagonal of the matrix. One must remember that, in the present analysis, only non-periodical considerations are used so far in the calculation of the correlation matrix. In this way, the correlation outside the matrix is considered as zero when the filtering procedure is applied. When the window size accounts for points outside the correlation domain, the zero information accounts for reducing the correlation value and, hence, important information in the main diagonal of the matrix, which is non-physical but easy to be implemented computationally.

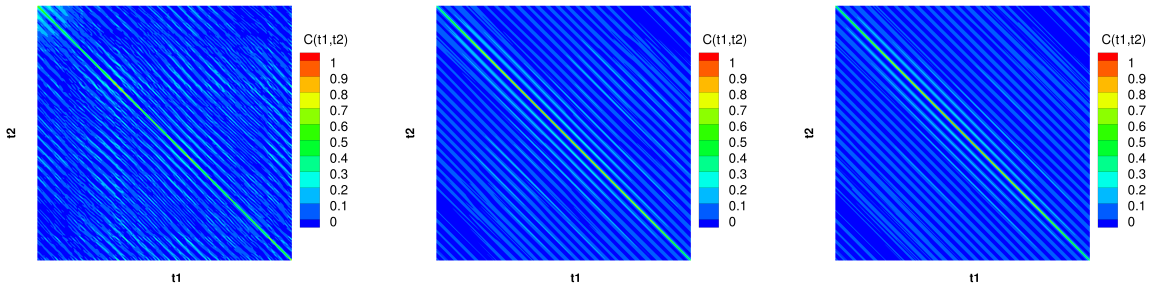

(a) $N_f = 0$. (b) $N_f = 400$. (c) $N_f = 800$.

Figure 3.41: Correlation matrices obtained by p-3D norm with Gaussian filtering SPOD for different window sizes N_f.

Nevertheless, one should remind that the time series is not periodic as well as this consideration will produce some drawbacks in the analysis. The consideration is not extremely harmful as for a DFT analysis because, in POD, the presence of a step function does not produce the same effect as in Fourier domain.

3.6.2 Periodic vs. Non-Periodic Time Series

Proper orthogonal decomposition does not require periodicity of the time signal. For a finite time series, the spectral filtering has no information outside the boundaries of the correlation matrix. In this case, one may consider that the lack of information represents a zero correlation outside the boundaries. However, if the time series is stated as periodic, the outside region of the correlation matrix is computed considering the matrix as periodic itself. In well-resolved numerical data of statistically converged turbulent flows, the periodicity of the signal is usually assumed and that can improve the reconstruction of information in POD modes. Also, the choice between Gaussian or square-box type functions for the filtering operation may produce considerable differences when the periodic time series is considered. One of the noticeable differences between the periodic and the non-periodic time series in the filtering operation is on the correlation matrix, as shown in Fig. 3.42. This figure presents the correlation matrices obtained by

the pressure norm, p-3D, for the non-periodic case and for the square-box and Gaussian filtered periodic cases. The main diagonal of the matrix computed in the non-periodic case decreases its magnitude near the boundaries due to the accounting of zero values outside the matrix domain. Assuming that the time series is periodic, one has a periodic correlation matrix where the main diagonal presents higher values near the boundaries when compared to the non-periodic case.

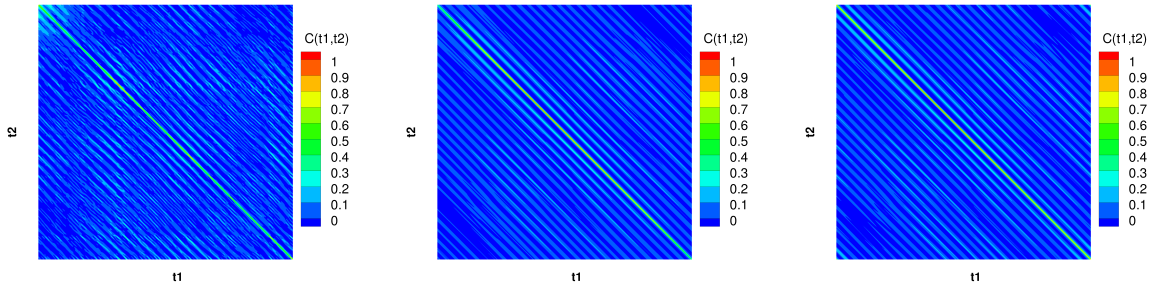

(a) Non-periodic. (b) Square-box periodic. (c) Gaussian periodic.

Figure 3.42: Correlation matrix obtained with the p-3D norm for different filtering functions for window size $N_f = 400$.

The POD eigenvalue spectrum is slightly affected by the periodic assumption, as shown in Fig. 3.43. The filtering operation may flatter the POD spectrum and periodicity improves such feature as can be seen in the second mode pair for the k-3D norm in Fig. 3.40(a). The SPOD technique did not show a considerable improvement in the coupling of the second pair of modes obtained using the kinetic energy norm for the non-periodic time series assumption. However, when periodicity is considered, the second mode pair of modes is coupled for the k-3D norm. The p-3D norm presents only small differences in the POD spectrum when periodicity is assumed.

The visualization of the spectral content of the temporal modes helps in the identification of the differences between the periodic and non-periodic assumptions. Figure 3.44(a) shows how the periodicity in the time series improves the definition of the amplitudes in the spectrum, focusing only in the main frequency of the POD mode. One can see that the low and high-frequency broadband content of the spectrum is considerably reduced when periodicity is enforced. Here, the Gaussian filtering is used with $N_f = 400$ for both periodic and non-periodic cases.

The comparison between the square-box and the Gaussian filtering functions is shown in Fig. 3.44(b). The oscillations in the frequency content are present for both filter types. When the non-periodic assumption is considered, as shown in Figs. 3.32 and 3.33, the oscillations are more prominent for the square-box filtering, especially the dominant tonal frequency. In these cases, the Gaussian function presents a smoother spectral content. When the periodic time series is assumed, the cleaning effect in the spectrum is intensified

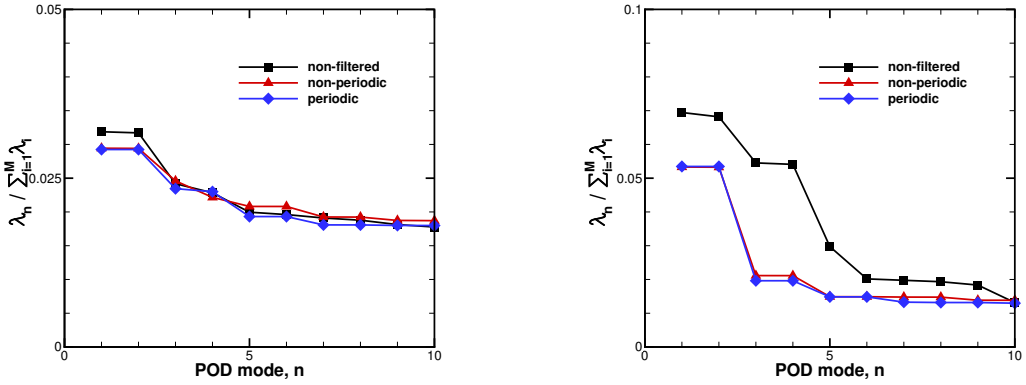

(a) k-3D norm. (b) p-3D norm.

Figure 3.43: POD spectrum including the filtering operations assuming periodic and non-periodic time series. Results are obtained using the Gaussian filtering with window size $N_f = 400$.

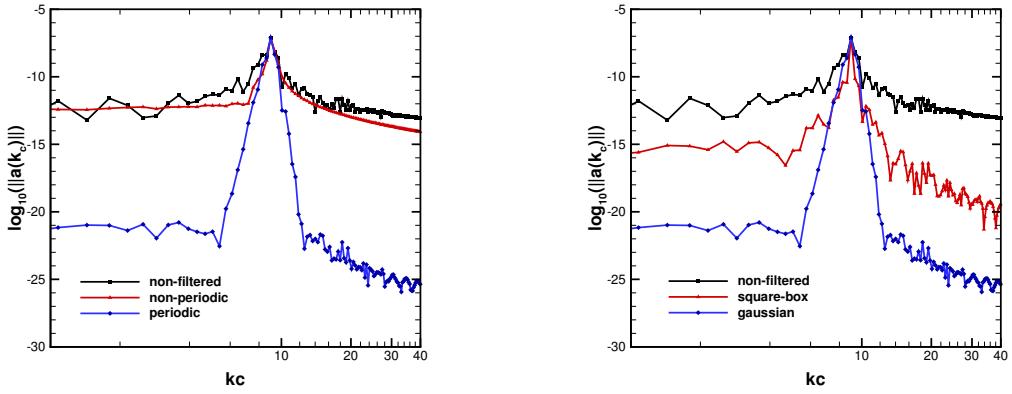

(a) Periodicity effect. (b) Filtering type effect.

Figure 3.44: Spectra of the 1st temporal mode a_1 obtained with the k-3D norm. Results are obtained for non-filtered and filtered correlation matrices with and without the periodicity time signal consideration for window size $N_f = 400$.

outside the narrowband of the dominant POD mode frequency.

Figure 3.45 presents the phase diagram for the first POD mode pair obtained by the k-3D norm using different filter functions. This figure shows that, for the same window size N_f, the square-box function with periodic assumption converges faster to the Fourier modes which contain information of a single frequency. For a POD analysis, it may be desirable that the modes contain more than only one frequency in order to extract useful turbulence information in the POD eigenfunctions. In Figs. 3.45(b) and (c) one can observe that, for the Gaussian filter, the periodic assumption presents noticeable improvements in harmonic correlation compared to the non-periodic implementation. The first POD mode pair has a clear correlation in the phase diagram. However, it was shown in Figs. 3.22 and 3.35 that the standard POD and the spectral POD could not provide a

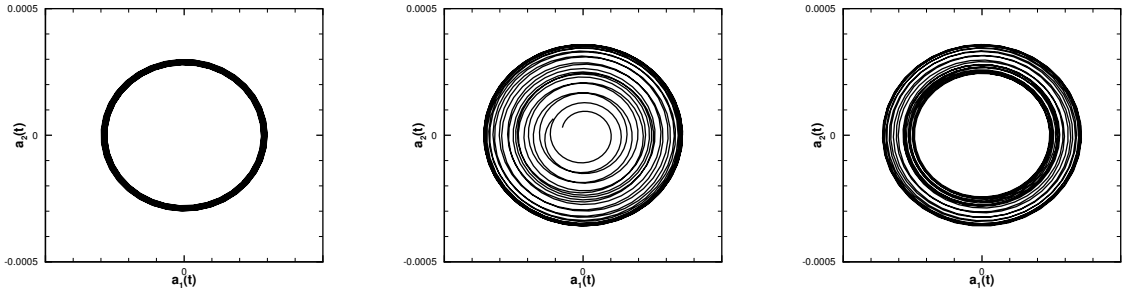

(a) Square-box periodic. (b) Gaussian non-periodic. (c) Gaussian periodic.

Figure 3.45: Phase diagram for the first pair of modes (a_1 and a_2) showing the improvements in harmonic correlation obtained by the k-3D norm for different filter functions with $N_f = 400$.

harmonic correlation for the second and third mode pairs when the kinetic energy norm was employed. When the correlation matrix is assumed periodic in the spectral POD method, these mode pairs present an improved correlation as one can notice in Fig. 3.46. As one can see, these mode pairs oscillate at low frequencies which are not well captured by the present simulation database, due to computational costs. Even though these larger scale structures may not be computed entirely, they are still part of the resolved turbulent flow. The assumption of the periodic time series combined with the spectral filtering in the POD are able to capture the presence of the high energy POD modes oscillating at lower frequencies than for the first mode pair. A similar analysis would be difficult to perform using DFT.

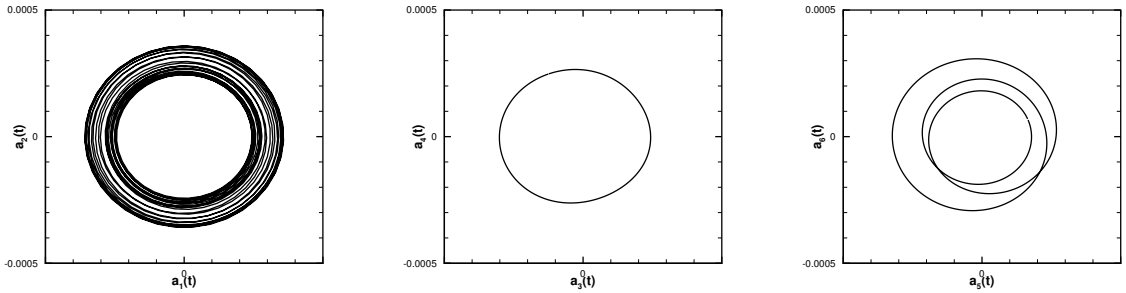

(a) a_1 and a_2. (b) a_3 and a_4. (c) a_5 and a_6.

Figure 3.46: Phase diagrams for different mode pairs obtained by the k-3D norm with the Gaussian filter, $N_f = 400$ and periodic time series assumption.

The spectral content of the time mode amplitudes a_1, a_3 and a_5 obtained by the k-3D norm is shown in Fig. 3.47. These results are obtained using the Gaussian filter with $N_f = 400$. When the periodic assumption is applied, the broadband content of the spectrum at lower and higher frequencies is reduced and the tonal peak is better defined. The first mode is responsible for capturing the most energetic turbulent structures in the flow which oscillate at the narrowband frequencies associated to the tonal noise peak

analyzed in the acoustic radiation, as shown in Fig. 3.6. As observed in the phase diagrams of Fig. 3.46, the 3rd and 5th modes, a_3 and a_5, associated to the 2nd and 3rd mode pairs, respectively, are related to lower frequencies in the spectrum. In these cases, the periodic assumption is also able to clear the broadband content of the spectra defining the amplitudes of the low frequency phenomena associated to these modes.

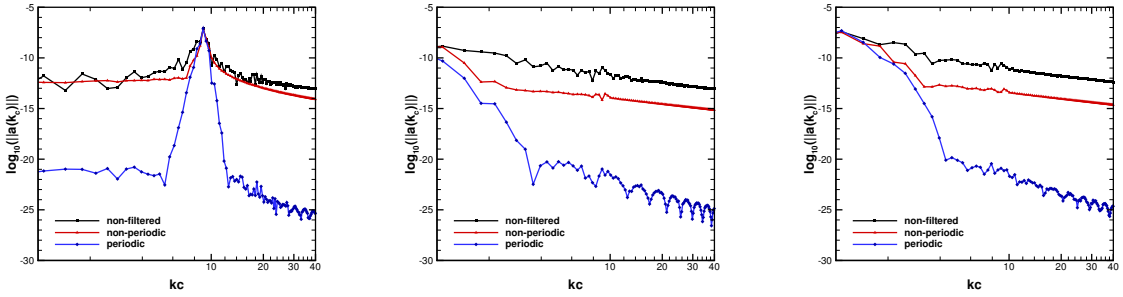

(a) 1st POD mode a_1. (b) 3rd POD mode a_3. (c) 5th POD mode a_5.

Figure 3.47: Spectra of POD temporal modes obtained by the k-3D norm and the Gaussian filtering with window size $N_f = 400$.

The POD eigenfunctions describe the spatial coherent structures that oscillate at the respective frequency content of the mode pair. In Fig. 3.48 one can see the spatial eigenfunctions for POD modes λ_1, λ_3 and λ_5, obtained using the k-3D norm with the same parameters as in the previous analysis. One can see the periodic structures in the airfoil wake region for mode λ_1. Modes λ_3 and λ_5 present a distorted pattern since they are related to larger structures, which oscillate at lower frequencies, not well-resolved. However, one may notice that these eddies are aligned with the flow stream on the suction side of the airfoil. Coherent structures perpendicular to the trailing edge have poor acoustic propagation, so are poorly captured in the acoustic scattering analysis (Ffowcs-Williams and Hall, 1970). Fig. 3.48(b) shows improvement in spatial characterization compared to Fig. 3.26(a), which presents the eigenfunction for mode λ_3 without spectral filtering. As expected from the phase diagrams, the structures obtained for mode λ_3 have longer wavelengths than those observed in mode λ_5.

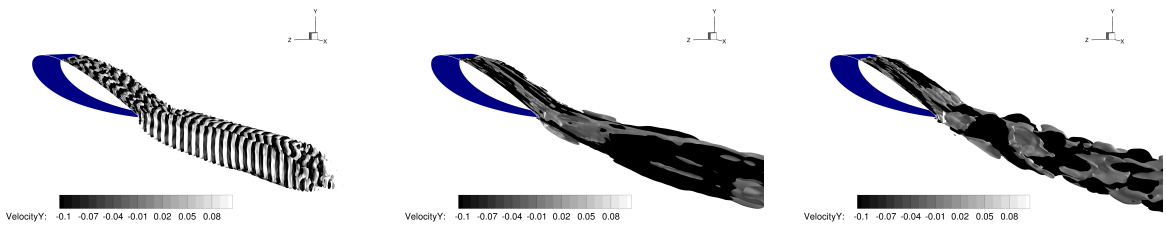

(a) Eigenfunction for λ_1. (b) Eigenfunction for λ_3. (c) Eigenfunction for λ_5.

Figure 3.48: Isosurfaces of y-component of velocity for POD spatial eigenfunctions obtained by the k-3D norm. Results are computed using the Gaussian filter with $N_f = 400$ and considering periodicity of the correlation matrix.

When the pressure norm, p-3D, is employed for the reconstruction of the correlation matrix, one can notice in Fig. 3.49 that the spectra of the temporal modes are modified compared to those obtained by the k-3D norm. For this case, the first, second and third mode pairs are related to narrowband information surrounding the tonal noise peak. Again, the assumption of a periodic time series reduces the broadband noise from the spectra allowing the identification of a cleaner tonal region. The frequencies of the tonal regions for the present mode pairs are the same as that analyzed in the airfoil self-noise generation studied in Wolf *et. al* (2012). On the other hand, the time mode amplitude a_7, associated to the 4th mode pair, is related to a high frequency narrowband region. In this case, the effects of periodicity on the construction of the correlation matrix are more evident. When the time series is assumed non-periodic, the SPOD spectrum associates the 4th mode pair to information at moderated frequencies, visualized as a narrowband tone at $kc \approx 25$. Considering a periodic time signal makes the SPOD reconstruction shift the energy of the 4th mode to higher frequencies as observed in Fig. 3.49(d).

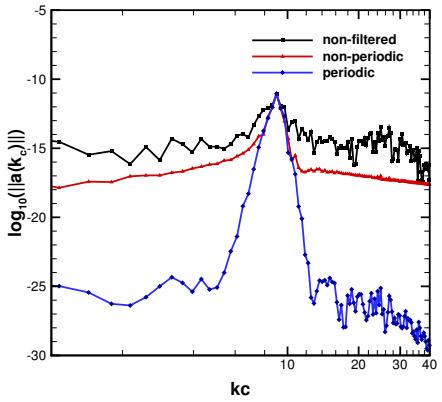

(a) 1st POD mode a_1.

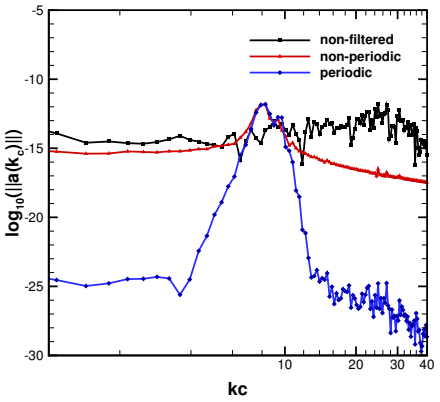

(b) 3rd POD mode a_3.

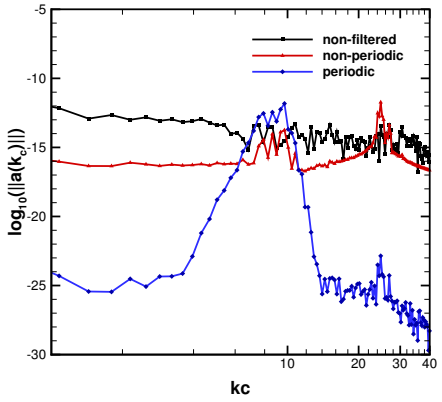

(c) 5th POD mode a_5.

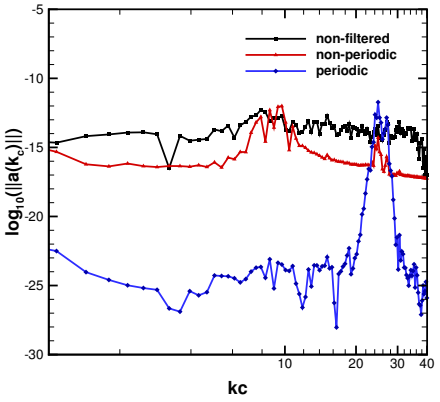

(d) 7th POD mode a_7.

Figure 3.49: Spectra of POD temporal modes obtained by the p-3D norm and the Gaussian filtering with window size $N_f = 400$.

In this way, it is possible to understand that the coherent structures present in the first 3 mode pairs of the SPOD reconstruction are related to the main noise sources at the tonal peak. The large elongated structures associated to these mode pairs are shown in Fig. 3.50. As they oscillate at more than one single frequency, the POD eigenfunctions still have some noise which slightly distorts the structures along the wake and boundary layer regions. The 4th mode pair is associated to the presence of high frequency oscillations. In Fig. 3.23, the high frequency oscillations were present in the 2nd mode pair, mode amplitudes a_3 and a_4, but the harmonic correlation was not clean enough for a visualization of the coherent structures in the flow data.

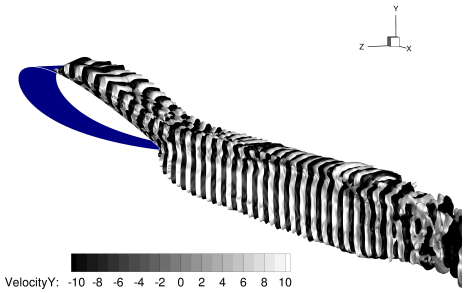

(a) Eigenfunction for λ_1.

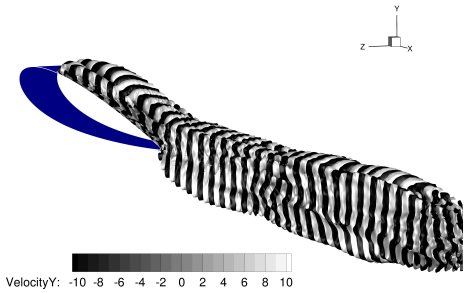

(b) Eigenfunction for λ_3.

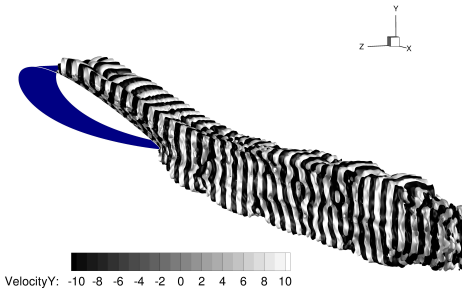

(c) Eigenfunction for λ_5.

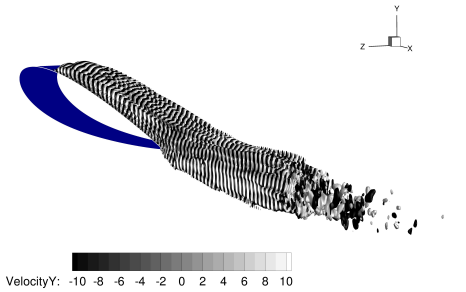

(d) Eigenfunction for λ_7.

Figure 3.50: Isosurfaces of y-component of velocity for POD spatial eigenfunctions obtained by the p-3D norm. Results are computed using the Gaussian filter with $N_f = 400$ and considering periodicity of the correlation matrix.

The high frequency oscillations are well-captured by the current high-fidelity simulation due to the low-dispersion/low-dissipation characteristics of the numerical methods employed. These methods are adequate for resolving the high-frequency turbulent structures in the flowfield. In this sense, the small coherent structures responsible for these high-frequency scales are clearly observed in Fig. 3.50(d).

As an important insight on the turbulence and the coherent structures detected in this analysis, one can notice that the small coherent structures present in the 4th mode pair for the p-3D norm dissipate faster than those in the 1st, 2nd and 3rd mode pairs. This is related to the dissipative characteristics of turbulent flows at small scales. Similar to that,

the larger coherent structures, which are poorly resolved in the k-3D norm for the 2nd and 3rd POD mode pairs, propagate for the entire domain after passing through the solid body. For the POD analysis, even when the large coherent structures are not resolved entirely, it is possible to understand their behavior. In the present simulation data, more simulation time could result in a better representation of the spatial eigenfunctions.

In conclusion, the spectral filtering operation may present small differences in the energy distribution of the POD eigenvalue spectrum. However, the filtering can affect deeply the information contained by each POD mode. The distribution of energy changes the information present in the mode pairs providing a better harmonic correlation in the phase diagrams and, therefore, showing an improved correlation to physical coherent structures of the flowfield.

3.7 Fourier-POD Coupling for Homogeneous Directions

As stated by Lumley (1970), in homogeneous directions, POD modes are Fourier modes. This leads to a simplification in the POD analysis since Fourier decomposition can be applied along the homogeneous directions and the general POD reconstruction is only applied to the other directions. In the present flow configuration, due to the application of periodic boundary conditions and the 2D geometry, the flow is homogeneous along the spanwise direction. In this way, POD is applied to the flow quantities $\mathbf{q}(\mathbf{x}, t)$ in the form of the Eq. 3.2. This technique fully decouples the quantities in the spanwise direction so POD can be computed for each Fourier mode (z) separately. Thus, the present Section will discuss the features of such implementation and analyze the results from this methodology. Since the Discrete Fourier Transform, DFT, will be used for decoupling the homogeneous direction, the present method will be a combination of Fourier decomposition and POD, namely, Fourier-POD analysis.

A Fast Fourier Transform (FFT) algorithm is used to decompose the homogeneous direction due to its simplicity and computational speed. Nevertheless, different decomposition techniques could be applied, such as dynamic mode decomposition (DMD) for spatial instability analysis, or wavelet decomposition. For the sake of clarity, spanwise Fourier modes are named z with superscript corresponding to the specific Fourier mode, starting from mode 0, which provides the mean value. POD modes λ can also use superscript to identify the correct Fourier mode and subscript referred to the singular value, when applied.

In the present LES data, the flow is resolved using a staggered grid and the body-fitted

O-grid has twice the number of nodes than the background grid. In order to allow the Fourier decomposition of the flowfield in the spanwise direction, a 2nd-order interpolation is performed on the background grid along the spanwise direction to refine the mesh and build data with the same number of grid points all over the computational domain. Therefore, a Fourier decomposition via FFT is performed in the computational domain for all nodes along the spanwise direction. This procedure is performed after computing the mean flow and extracting the fluctuating quantities.

The current procedure yields similar results for the Fourier mode z^0 compared to the spanwise mean 2D procedure described in Section 3.4. However, the Fourier-POD here described consists in decomposing the Fourier modes in the spanwise direction only after the fluctuating quantities are computed. Even so, some analysis of Section 3.4 can be applied to what is analyzed in the present section, especially regarding to mode coupling and spectral content of the Fourier modes. The analysis of Section 3.4 can be considered as a Fourier-POD analysis using only the Fourier mode z^0, *i.e.*, the constant mode.

As the spanwise direction is fully decoupled, the Fourier-POD is performed for each individual Fourier mode. Figure 3.51 shows the POD eigenvalue spectra for the k-3D and p-3D norms. The singular values are normalized by the sum of values in the constant mode z^0. That is because the singular values are higher when the content of the correlation matrix presents higher values. The normalization shows how the energy of the fluctuations is more intense for the 1st Fourier mode z^0 mode and decays along the spectra. For Fourier modes of larger wavenumbers than the mode z^4, the fluctuations are so small that the POD spectrum is not even considered in the analysis for the POD norms analyzed here.

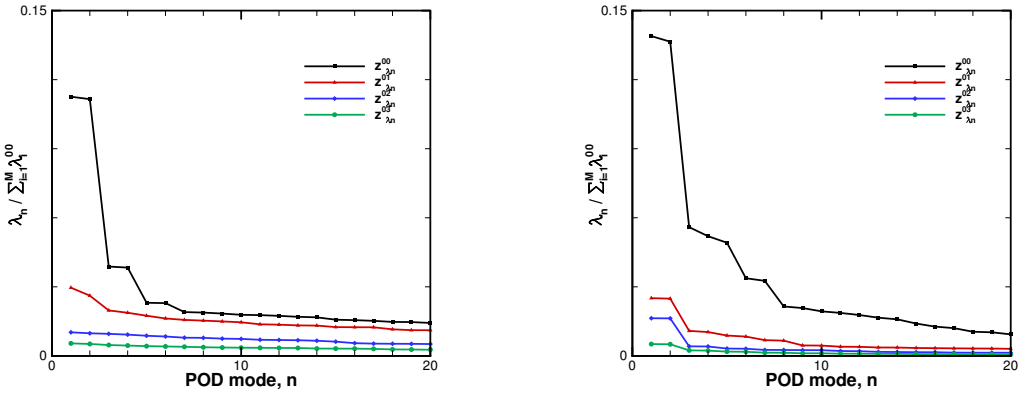

(a) k-3D norm.

(b) p-3D norm.

Figure 3.51: POD spectrum of first 4 Fourier modes in the spanwise direction (z) normalized by the sum of singular values from the constant Fourier mode (z^0) for different norms.

In Fig. 3.51, one can see that the singular values in the λ_3^0, λ_4^0 and λ_5^0 POD modes are decoupled for the p-3D norm in z^0. On the other hand, the first 3 POD mode pairs seem to

be clearly coupled for the k-3D norm. The behavior of the coupled and decoupled modes has been analyzed in the previous sections, so the corresponding harmonic correlations will not be presented here. Instead, the spectral content of the modes will be analyzed.

As a Fourier decomposition is performed, the eigenvectors, mode amplitudes and spatial eigenfunctions are now complex values. Figure 3.52 shows how the real and imaginary parts of the complex numbers which represent the time mode amplitudes are related. It shows that they have a phase relation and the spectral content of these quantities is approximately the same. This is not applied to the Fourier mode z^0, as its imaginary part is zero. Consequently, for easiness in the following analysis, only the spectral content of the real parts of the eigenvectors and mode amplitudes will be analyzed. To visualize the spatial eigenfunctions, an inverse Fourier transform is performed computing only the respective Fourier mode desired. From now on, the analysis will focus in each Fourier mode separately.

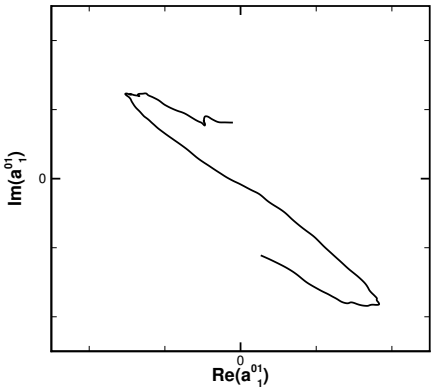

(a) $Real(z_1^1)$ and $Imag(z_1^1)$.

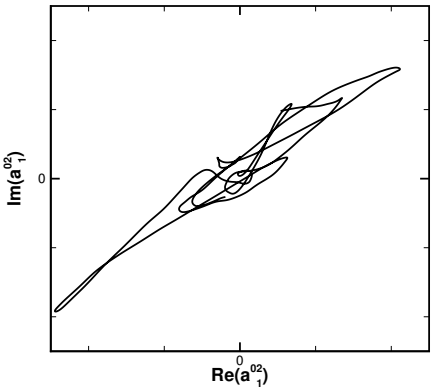

(b) $Real(z_1^2)$ and $Imag(z_1^2)$.

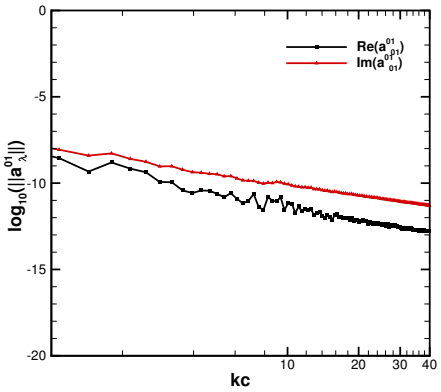

(c) Spectra of $Real(z_1^1)$ and $Imag(z_1^1)$.

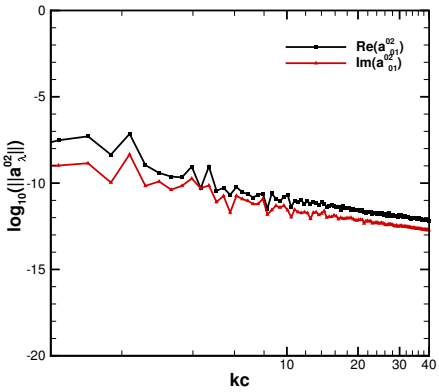

(d) Spectra of $Real(z_1^2)$ and $Imag(z_1^2)$.

Figure 3.52: Analysis of 1st POD modes.

As shown in the previous sections, kinetic energy and pressure norms yield different

decompositions of the POD modes. For example, the pressure norm captures high frequencies after the tonal noise and the kinetic energy norm tends to reconstruct low frequency information in the turbulent field. As the computational domain is not large enough for the propagation of low frequency waves and, as the pressure fluctuations decay faster after passing trough the trailing edge, the high frequency information is better captured by the pressure norm. On the other hand, the turbulent structures propagate over the domain until the buffer zone is reached which grants the kinetic energy norm with low frequency information that is not captured by the pressure. So, after reconstructing the main energetic content in the first POD modes at the narrowband near $k_c \approx 9$, each norm decomposes the turbulent information according to its own solution, low-frequency content in the kinetic energy norm and high-frequency content in the pressure norm. Therefore, both norms will continue to be used in the current analysis to allow a better understanding of the dynamics of the coherent structures in the flowfield data.

Figure 3.53 shows the spectral content of the time mode amplitudes a_1, a_3 and a_5 for each of the Fourier modes z^0, z^1 and z^2 using the k-3D norm. As shown in Fig. 3.14, the coherent structures present in the most energy containing mode pairs for the spanwise mean mode are related to the same spectral content. In Fig. 3.53(a) it is clear that these coherent structures oscillate at frequencies close to the tonal noise peak. Even so, these POD modes are still influenced by a large set of other frequencies. Figures 3.53(b) and (c) show the presence of low frequency coherent structures in the flowfield which were previously observed. One may notice that these low frequency coherent structures are not related to the spanwise correlated structures responsible for the tonal noise show in Fig. 3.6 and analyzed by Wolf *et. al* (2012).

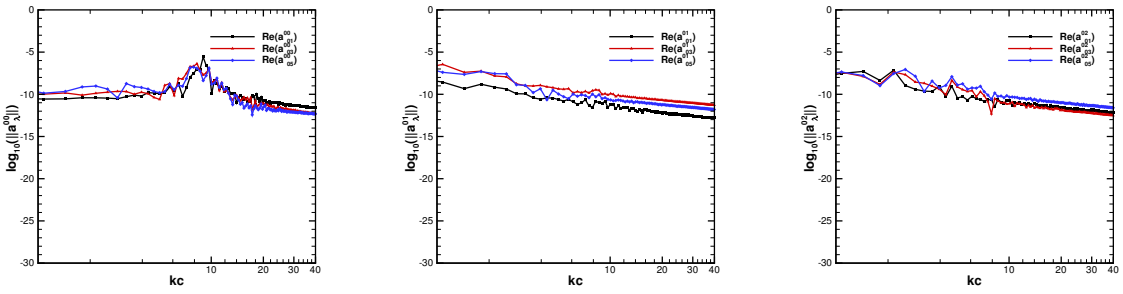

(a) Fourier mode z^0. (b) Fourier mode z^1. (c) Fourier mode z^2.

Figure 3.53: Spectral content of the real part of the POD temporal modes a_1, a_3 and a_5 obtained by the k-3D norm for different Fourier modes.

In Fig. 3.54, the dynamic behavior of the coherent structures can be analyzed through an analysis of the spatial eigenfunctions for Fourier mode z^0. The 1st POD mode λ_1^0 eigenfunction presents a large wavepacket developed on the turbulent flow over the suction side and that grows after passing by the trailing edge. POD eigenfunctions

from the modes λ_3^0 and λ_5^0 show how some instabilities are present over the suction side. This figure indicates how the Fourier mode z^0 contains the information related to the turbulence generated in the boundary layer and that propagates as 2D coherent structures downstream the solid body. Near the trailing edge, large 2D coherent structures oscillate and, as the POD mode λ_5^0 shows, the coherent structures are combined to form larger wavepackets downstream the trailing edge.

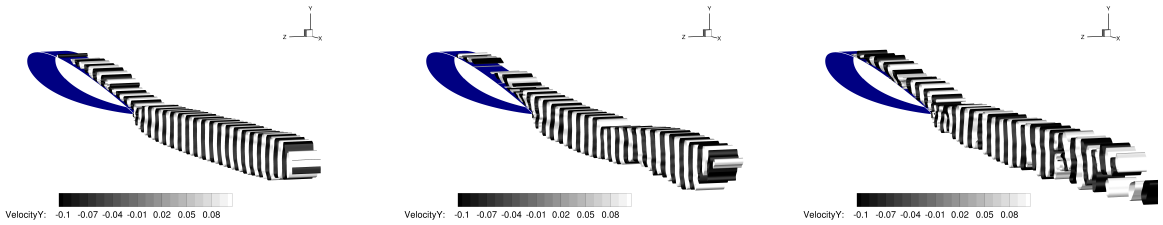

(a) Eigenfunction for λ_1^0. (b) Eigenfunction for λ_3^0. (c) Eigenfunction for λ_5^0.

Figure 3.54: Spatial eigenfunctions for spanwise Fourier mode z^0 obtained by the k-3D norm.

A visual inspection of the Fourier mode z^1 shows that it contains information related to turbulence with wavenumber one along the spanwise direction. The present high-fidelity flow data was generated to accurately compute the small turbulent structures along the airfoil span. In this sense, the spanwise direction has 5 times the size of the displacement thickness in the trailing edge region, which would be sufficient to reduce the correlation of the small scale turbulent structures which compose the noise sources for an aeroacoustic prediction. However, the development of larger scale coherent structures would require a wider span in order to be fully resolved in the numerical simulation. As shown in Fig. 3.53(b), the spectral content of the POD modes in z^1 is related to low frequency oscillations which may not be fully captured in the large eddy simulation. As the first POD mode pair is decoupled for the current Fourier mode, the analysis of the spatial eigenfunctions is not easy, as shown in Fig. 3.55.

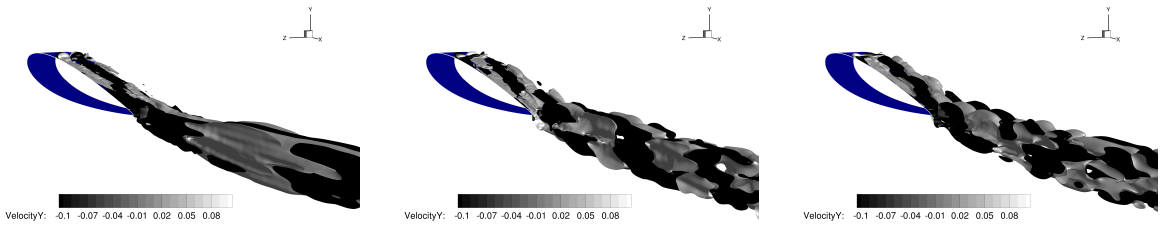

(a) Eigenfunction for λ_1^1. (b) Eigenfunction for λ_3^1. (c) Eigenfunction for λ_5^1.

Figure 3.55: Spatial eigenfunctions for spanwise Fourier mode z^1 obtained by the k-3D norm.

Taking a closer look over the structures formed over the suction side in Fig. 3.56, one can notice the presence of large coherent structures aligned with the airfoil chord

and that oscillate in the spanwise direction. As the low frequency information is poorly captured in the numerical data with limited time signal, the large structures present are not clearly captured as well. Also, the limited span size affects the capturing of these structures via Fourier-POD analysis. That is because for the larger wavelengths in the spanwise direction, mode z^1 may not be enough to capture the dynamics of these coherent structures.

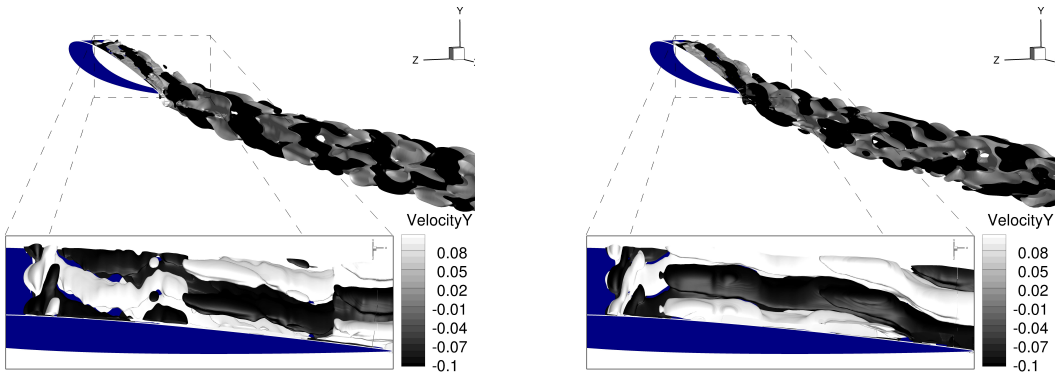

(a) Eigenfunction for λ_3^1. (b) Eigenfunction for λ_5^1.

Figure 3.56: Detail view of spatial eigenfunctions for spanwise Fourier mode z^1 obtained by the k-3D norm.

The analysis of the Fourier mode z^1 leads to doubts over the span size required to capture large turbulent structures in homogeneous directions. An analysis of the POD modes for z^2 can be observed in Fig. 3.57 where one may notice the presence of large eddies aligned with the flow, in the same way presented in z^1. Now, the spanwise length is not the problem as the wavelength solved comprises half the span. These coherent structures oscillate at low frequencies as shown in Fig. 3.53(c) and they have similar dynamics compared to that observed in Fig. 3.55. From these figures, it is possible to determine that the poorly captured coherent structures in the POD modes for z^1 are related to the limited time signal of the numerical data.

As the computational time is limited by simulation costs and data storage, low frequency structures are seldom captured on a Fourier-POD analysis. Despite this observation, it is indeed a great capability of the current analysis to show that running the simulation for a longer time would result in the capturing of further energy containing turbulence information. Also, the Fourier-POD analysis proves that these large coherent structures are related to spanwise Fourier mode z^1, and that they oscillate in the homogeneous direction, forming large rolls over the suction side of the airfoil that will further interlace in the vortex wake.

These large structures are not present in the acoustic scattering analysis, because the eddies are perpendicular to the trailing edge and do not propagate sound efficiently to the farfield. These coherent structures can only be analyzed via global modes of the nonlinear

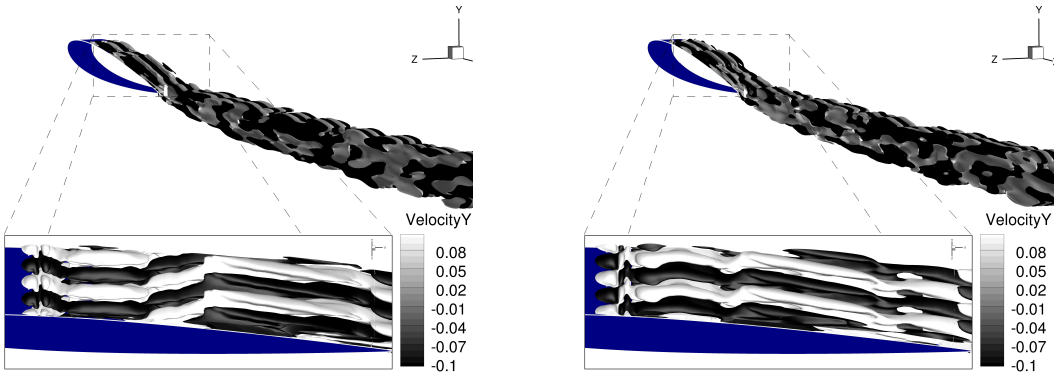

(a) Eigenfunction for λ_1^2. (b) Eigenfunction for λ_3^2.

Figure 3.57: Detail view of spatial eigenfunctions for spanwise Fourier mode z^2 obtained by the k-3D norm.

flow. They have similar spatial behavior as the POD modes λ_3 and λ_5 in POD and SPOD analysis in Sections 3.5.2 and 3.6.2.

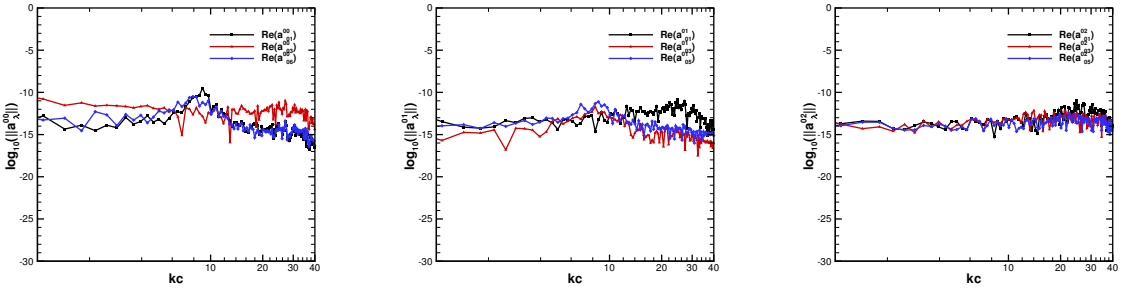

(a) Fourier mode z^0. (b) Fourier mode z^1. (c) Fourier mode z^2.

Figure 3.58: Spectral content of the real part of the POD temporal modes a_1, a_3 and a_5 obtained by the p-3D norm for different Fourier modes.

As previously mentioned, the p-3D norm will tend to reconstruct POD modes at high-frequencies, differently from the k-3D norm. Figure 3.58 shows the spectral content of the temporal mode amplitudes for spanwise Fourier modes z^0, z^1 and z^2. The constant mode does not contain only information for the tonal band as shown for the k-3D norm in Fig. 3.53(a). This can be observed in the spectral content of the 3rd POD mode λ_3^0 which is not coupled and contains information for a broad range of frequencies, especially at high frequencies. The following paired mode contains the POD modes λ_6^0 and λ_7^0. The spanwise Fourier mode z^1 also presents POD modes with information spanning multiple frequencies and, for this case, the temporal modes a_3^1 and a_5^1 contain information at the tonal noise frequency. However, the 1st mode amplitude a_1^1 is composed by information at high frequencies, similar to that of the time mode amplitude a_3^0 for z^0. The POD modes for spanwise mode z^2 contain too much noise in their spectral content but oscillate mainly in the high-frequency range.

As mentioned, the POD modes λ_1^0 and λ_2^0, also the λ_6^0 and λ_7^0 are coupled for the

spanwise mode z^0. Therefore, they present a clear turbulent information in their spectral content and spatial eigenfunctions. The 3rd POD mode λ_3^0 is noisy and presents spectral content at a broad range of frequencies. As a result, in Fig. 3.59(b), 2D correlated structures at multiple length scales are presented. The 1st POD mode λ_1^0 eigenfucntion shows a clear wavepacket downstream the trailing edge, but the 6th POD eigenfunction λ_6^0 is already disturbed in the vortex wake. It is important to notice the presence of large coherent structures detaching from the airfoil surface in the 6th POD mode λ_6^0 eigenfunction after the turbulent transition. Instabilities in the vortex wake are also present.

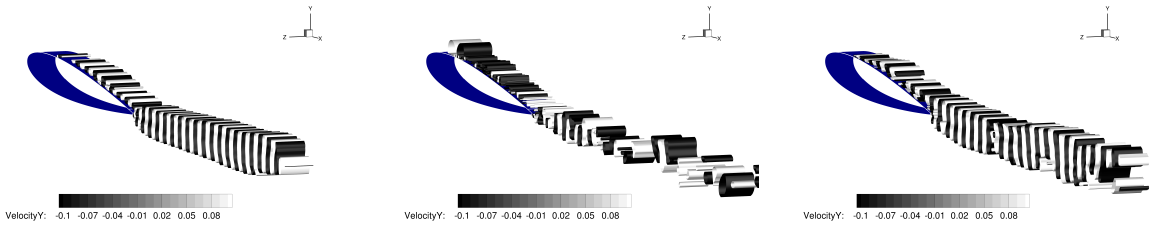

(a) Eigenfunction for λ_1^0. (b) Eigenfunction for λ_3^0. (c) Eigenfunction for λ_6^0.

Figure 3.59: Spatial eigenfunctions for spanwise Fourier mode z^0 obtained by the p-3D norm.

For the spanwise Fourier mode z^1, the 1st POD mode λ_1^1 eigenfunction oscillates at higher frequencies as shown in its spectral content. However, the 3rd and 5th POD modes, λ_3^1 and λ_5^1, present a spectral content that is dominant at the tonal peak frequency. The tonal noise is said to be related to the presence of coherent structures aligned in the span direction and that generate noise more efficiently. Figure 3.60 shows coherent structures which are not perfectly aligned in the spanwise direction. They propagate as sound with low efficiency, but also oscillate at the narrowband frequencies around the tonal peak. Therefore, they also contribute to the noise generation at this frequency range. Also, it is possible to see that the vortex wake contains instabilities that cause a merging of coherent structures.

The spanwise Fourier mode z^2 is formed mainly from high frequency oscillations as observed in the spectra plots of the POD temporal modes. Therefore, the POD modes contain noise from a broad range of frequencies as shown in Fig. 3.58 and it is difficult to analyze the spatial eigenfunctions. The oscillations at these frequencies also contain the presence of diagonally aligned structures, but oscillating at higher frequencies than those observed for z^1.

A quick comparison among the results obtained for the spectral content of the mode amplitudes using the Fourier-POD implementation and the full 3D POD implementation, both considering the p-3D norm, shows that the Fourier-POD analysis does not lose any turbulence information with respect to the full 3D POD technique. The spectral content

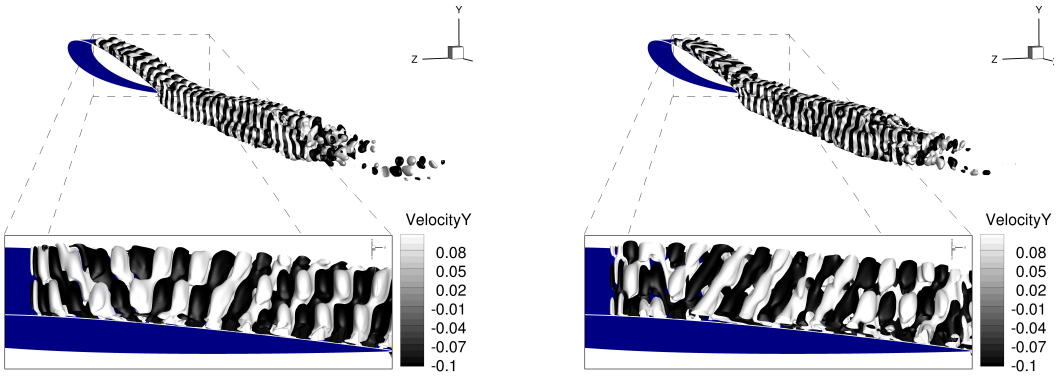

(a) Eigenfunction for λ_3^1. (b) Eigenfunction for λ_5^1.

Figure 3.60: Detail view of spatial eigenfunctions for spanwise Fourier mode z^1 obtained by the p-3D norm highlighting coherent structures diagonally aligned with the airfoil span.

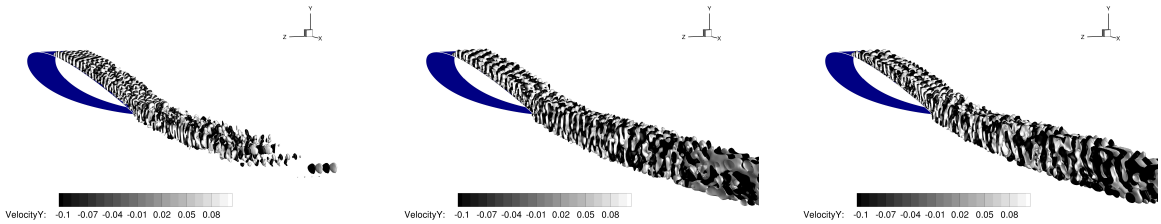

(a) Eigenfunction for λ_1^2. (b) Eigenfunction for λ_3^2. (c) Eigenfunction for λ_5^2.

Figure 3.61: Spatial eigenfunctions for spanwise Fourier mode z^2 obtained by the p-3D norm.

of the coupled modes presented in Fig. 3.23(d) are also shown in Figs. 3.58(a) and (b). The high frequency oscillations present in Fig. 3.23(e) are now appearing mainly in Fig. 3.58(c) but are also a part of the spectral content of the 1st POD mode for z^1. Fourier-POD improves the identification of coherent structures related to each Fourier mode in the homogeneous direction. In this way, it cleans the turbulence information and is useful in the analysis of separate components of the flowfield that appear clustered in the results of the general 3D implementation proposed in Section 3.5.

3.8 Combined Fourier-Spectral POD

For those cases where a homogeneous direction in the flowfield is not available, for example, a fully 3D geometry such as a landing gear, the general 3D implementation of POD may be the only procedure available for the analysis of the most energetic coherent structures in the flow. However, as already shown in previous sections, the POD modes may contain excessive noise from multiple frequencies making the analysis of coherent structures difficult. Moreover, a broad spectral content may is also not adequate for

the understanding of the coherent structures. For these cases, an implementation of the spectral POD method was shown in Sec. 3.6 to produce improved mode decompositions at specific frequencies and, hence, improving the analysis of turbulent structures composing the flowfield.

When a homogeneous direction is available in the flowfield, a Fourier decomposition can be employed reducing the cost of the POD reconstruction and allowing a clearer identification of coherent structures along the span. However, even with the Fourier decomposition, the reconstruction of turbulent structures may contain broadband spectral content which may difficult the analysis of the spatial eigenfunctions and temporal mode. In this sense, the spectral POD technique which already showed good results for the general 3D implementation of POD will be combined with the Fourier-POD method in order to assess the benefits of the combination of both techniques.

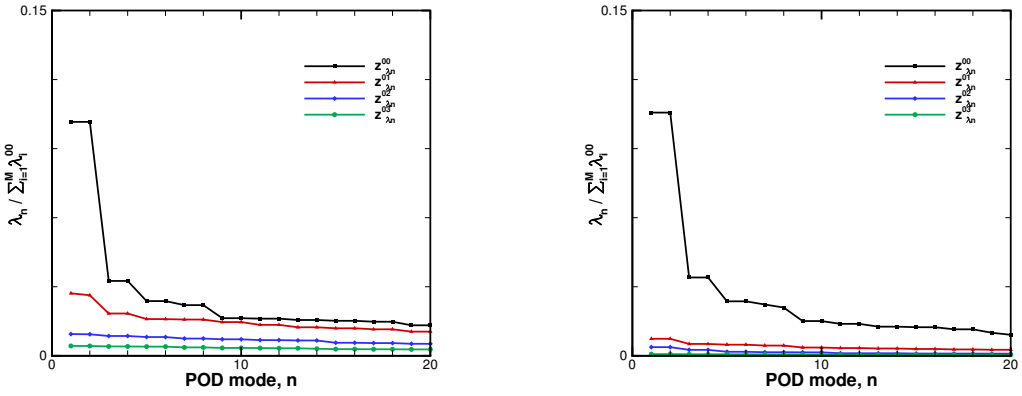

(a) k-3D norm. (b) p-3D norm.

Figure 3.62: POD spectrum of first 4 Fourier modes in the spanwise direction (z) normalized by the sum of singular values from the constant Fourier mode (z^0) for different norms.

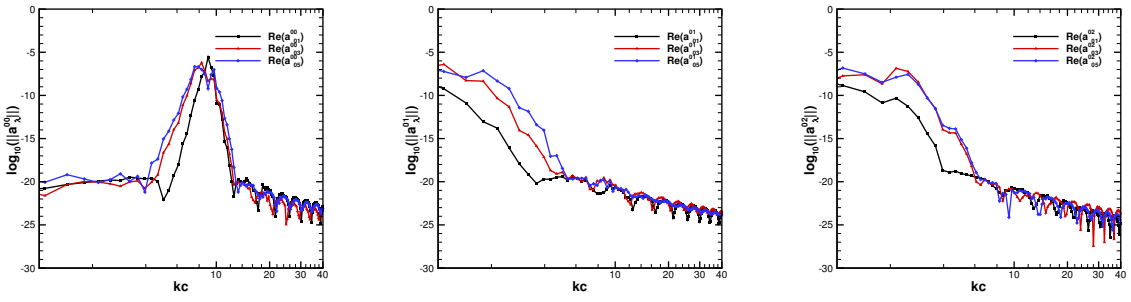

(a) Fourier mode z^0. (b) Fourier mode z^1. (c) Fourier mode z^2.

Figure 3.63: Spectral content of temporal POD modes a_1, a_3 and a_5 obtained by the k-3D norm using a periodic time series and Gaussian filter with window size $N_f = 400$ for different Fourier modes (z).

In the present section, a spectral filtering of the correlation matrix is applied using

the Gaussian window and the periodic time series assumption. These methods are chosen since they presented superior results for all cases analyzed. The window size is set as $N_f = 400$ for all spanwise modes. Clearly, a different window size could be applied for each Fourier mode optimizing the analysis according to the need of each correlation matrix. However, in the present work, only constant window sizes will be applied. Figure 3.62 shows the POD spectrum normalized by the sum of singular values for the mean Fourier mode z^0 for norms p-3D e k-3D. As expected, the combined Fourier-SPOD flatters the POD spectrum increasing the mode coupling and, therefore, improving the identification of coherent structures.

The spectral content of the mode amplitudes for z^0, z^1 and z^2, obtained using the Gaussian periodic spectral filtering and the k-3D norm is shown in Fig. 3.63. One may notice that the spectral content is more well defined and the frequencies which are away from the main narrowband associated with the specific POD mode have reduced amplitudes. In the same way as for the 3D POD implementation, the spectral filtering cleans the spectral content of POD modes. For the k-3D norm, the range of frequencies of the POD modes is slightly altered from the Fourier-POD results.

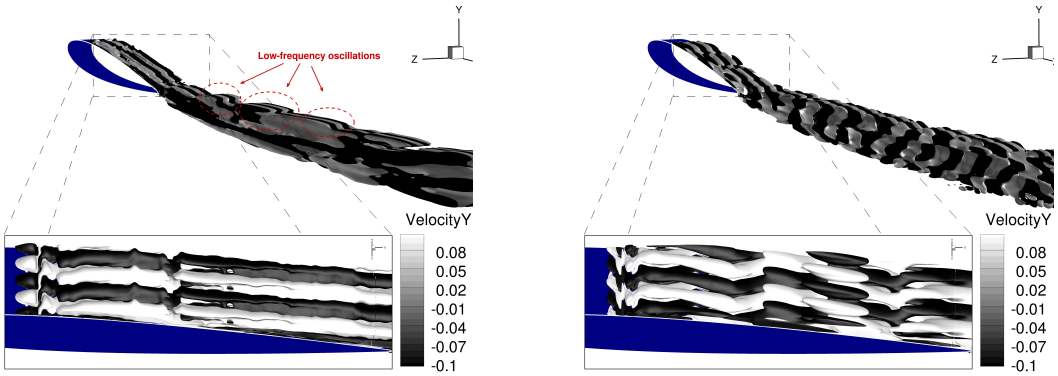

(a) Eigenfunction for λ_1^2. (b) Eigenfunction for λ_3^2.

Figure 3.64: Spatial eigenfunctions for Fourier mode z^2 and k-3D norm highlighting suction side coherent structures aligned with the airfoil chord and oscillating in the vortex wake. Results are obtained by a Gaussian filtering using a periodic time series and window size $N_f = 400$.

As the spectral filtering reduces the noise in the spectral content, only small differences are perceived in the analyses of the spatial eigenfunctions produced with and without the spectral POD. Nevertheless, it is possible to see in Fig. 3.64 that the coherent structures formed over the airfoil for span mode z^2 are cleaner. The presence of large rolls over the suction side along the spanwise direction is more visible for the spectral POD. Also, low frequency oscillations highlighted in Fig. 3.64(a) were not clearly identified in Fig. 3.57(a). These structures are formed in the vortex wake and are clearly visible only in the 1st POD mode λ_1^2 eigenfunction for z^2. They are components of the low frequency

content present in the spectral analysis shown in Fig. 3.65(c). Figure 3.64(b) presents streamwise coherent structures formed along the vortex wake and which were not clearly identified in Fig. 3.57(b).

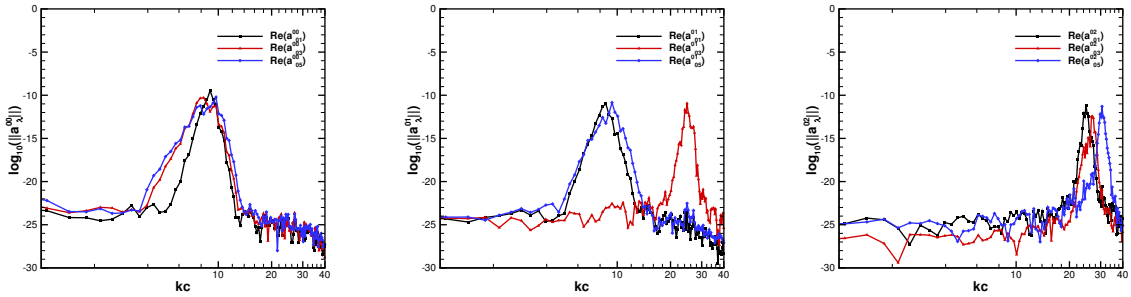

(a) Fourier mode z^0. (b) Fourier mode z^1. (c) Fourier mode z^2.

Figure 3.65: Spectral content of POD temporal modes a_1, a_3 and a_5 obtained by the p-3D norm using a periodic time series and Gaussian filter with window size $N_f = 400$ for different Fourier modes (z).

For the p-3D norm, using the same spectral POD parameters, the flow is mainly decomposed into tonal narrowband spectral content for Fourier modes z^0 and z^1, and high frequency oscillations for z^2, as shown in Fig. 3.65. The 3rd POD mode λ_3^1 obtained for z^1 presents oscillations at higher frequencies and its spectral content is similar to those obtained for z^2. The spectral POD has the clear characteristic of organizing the distributed energy over the spanwise Fourier modes.

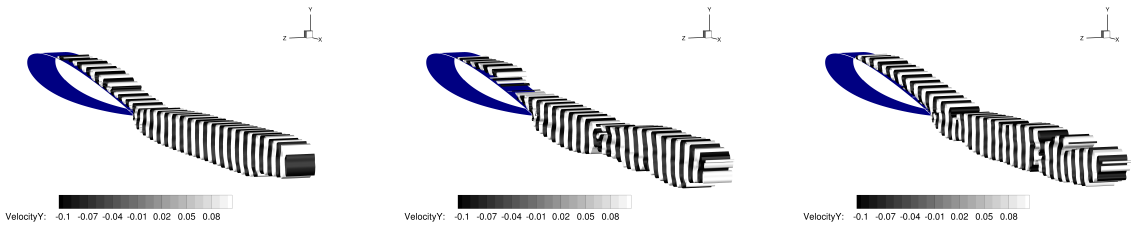

(a) Eigenfunction for λ_1^0. (b) Eigenfunction for λ_3^0. (c) Eigenfunction for λ_5^0.

Figure 3.66: Spatial eigenfunctions for spanwise Fourier mode z^0 obtained by the p-3D norm.

The Fourier mode z^0 computed for the p-3D norm presents spectral content at the same narrowband obtained by the k-3D norm. This is expected since this band is related to the most energy containing portion of the turbulent spectra and as it is associated to the presence of correlated 2D coherent structures on the flowfield, as shown in Fig. 3.66. This figure presents the eigenfunctions for different POD modes and z^0. As the p-3D norm was not able to capture these coherent structures initially, the implementation of Fourier-SPOD combination increased the mode coupling improving the identification of the large coherent structures related to the z^0 mode.

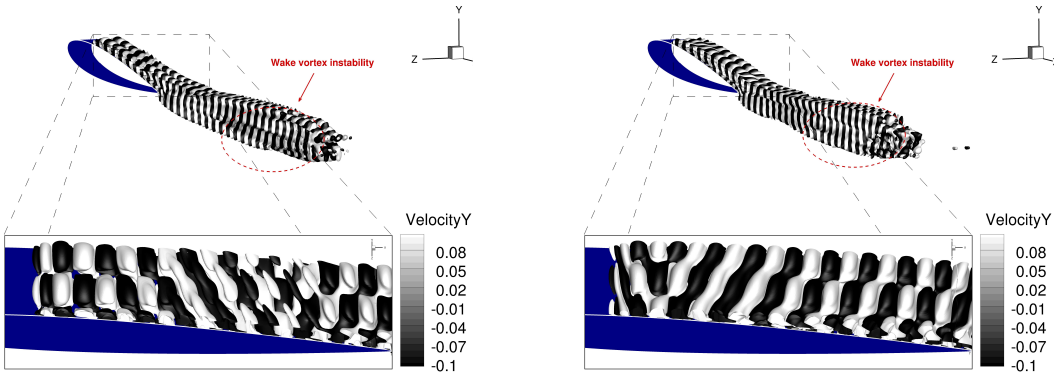

(a) Eigenfunction for λ_1^1. (b) Eigenfunction for λ_5^1.

Figure 3.67: Spatial eigenfunctions for Fourier mode z^1 obtained by the p-3D norm, highlighting suction side coherent structures diagonally aligned with the airfoil span. Results are obtained using a periodic time series and Gaussian filter with window size $N_f = 400$.

For the Fourier mode z^1, the 3rd POD mode λ_3^1 contains spectral information of higher frequencies than for the 1st and the 5th POD modes, λ_3^1 and λ_5^1. Its information is closely related to what is obtained in Fig. 3.68 for Fourier mode z^2. In Fig. 3.67 one can notice that the diagonal coherent structures formed over the suction side are clearly identified. It is possible to see how their dynamics is affected after passing the boundary layer tripping and how small coherent structures are detached from the boundary layer forming smaller structures over the airfoil. Also, as highlighted in red in Fig. 3.67, after passing the trailing edge, these structures collapse together to form larger 2D coherent structures in the vortex wake and that are not aligned with the spanwise direction but are diagonal to it. These coherent structures form a wake instability that breaks the eddies into small parts, before dissipating.

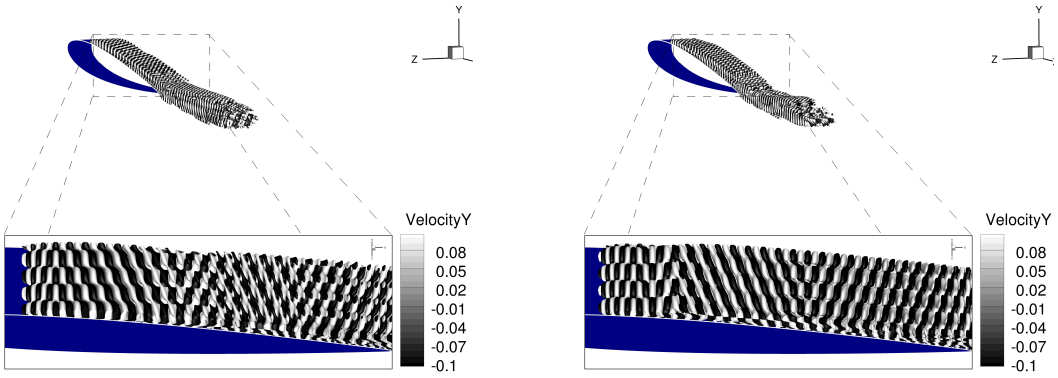

(a) Eigenfunction for λ_1^2. (b) Eigenfunction for λ_3^2.

Figure 3.68: Spatial eigenfunctions for Fourier mode z^2 obtained by the p-3D norm, highlighting suction side coherent structures diagonally aligned with the airfoil span. Results are obtained using a periodic time series and Gaussian filter with window size $N_f = 400$.

The Fourier mode z^2 has a spectral content containing mainly higher frequencies. This results in small coherent structures that are diagonal to the spanwise direction. Figure 3.68 shows how they change in direction quickly and dissipate fast downstream the trailing edge. Such issue is related to the grid stretching which dissipates smaller structures quicker. Also, it is important to notice how these small structures are close to the boundary layer, never detaching from the solid body. The presence of these high frequency oscillations shows how the spectral content of the turbulent boundary layer is formed from a broad range of frequencies.

One can notice how the spatial eigenfunctions are better defined when the spectral filtering is employed together with the POD reconstruction. A quick comparison between the results obtained in Figs. 3.61 and 3.68 shows how the content of the eigenfunctions can now be clearly analyzed, even when they contain lower energy at the Fourier modes. Even for z^1, a comparison of results obtained in Figs. 3.60 and 3.67 shows that the Fourier-SPOD eigenfunctions are better defined than those from the Fourier-POD. The spectral filtering combined with the Fourier-POD analysis presents cleaner results which improves the visualization of coherent structures present in the turbulent flows.

4 Coherent Structures in Wall-Bounded Turbulence

The present section will show results for Proper Orthogonal Decomposition (POD) applying the techniques discussed previously in different flow configurations. All numerical data analyzed in this section are computed using the numerical methodology presented in Section 2.2.

In Section 3, the mathematical basis of POD as well as the application to fully turbulent numerical data showed the benefits of applying the gaussian window filtering in the correlation matrix for coherent structures analysis, resulting in Spectral POD (SPOD) modes. The periodic time series assumption also enhanced the quality of the spatial characterization. Considering the spanwise direction as homogeneous, the flow can be decomposed in spatial Fourier modes, which makes the problem less for computationally expensive.

The POD norms resulted in different spatial and temporal characterization of inner structures of the turbulent flow. The turbulent kinetic energy norm (k-3D) captured the tonal noise in the first mode pair, then presented characteristics of hidden eddies at low frequencies. The pressure fluctuations norm (p-3D) characterized the high-frequency oscillations mainly after capturing the tonal noise in the first mode pair. The discrepancy between the POD norms is related to the characteristics of the oscillations of variables used for computing each norm.

When the homogeneous spanwise direction is considered, the Fourier decomposition gathered POD and SPOD modes with correlated spectral content at approximately the same range of frequencies. This feature was enhanced using the k-3D norm. Using the p-3D norm, for the same spanwise Fourier mode, the most energy containing POD mode pairs could present spectral content at different frequency ranges.

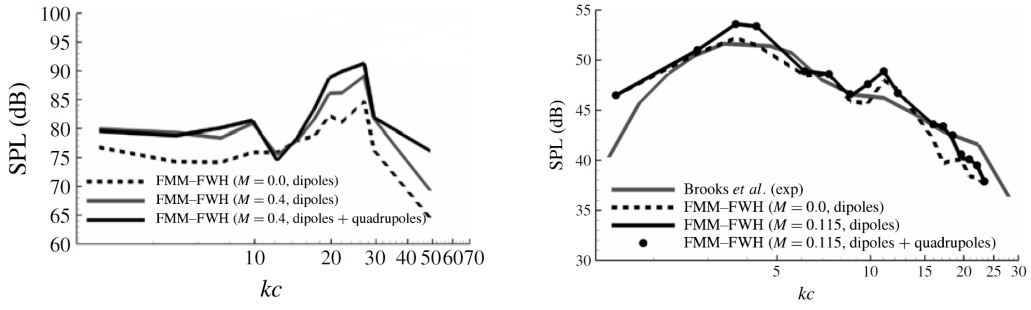

(a) $M_\infty = 0.4$. (b) AoA = 0 degs.

Figure 4.1: Sound pressure level (SPL) for analyzed flow configurations in Section 4 at an observer location $x = c$, $y = 7.9c$ and mid-span originally presented by Wolf *et. al* (2012).

The cases studied in the present section were previously analyzed by Wolf *et. al* (2012) and the sound spectra related to them is shown in Fig. 4.1. The general implementation of POD not considering the spanwise homogeneous direction will be used for the moderate Mach number configuration as an example due to its relation with the case studied in Sections 3.5 and 3.6. For both flow configurations, the combined Fourier-SPOD will be applied to analyze the spatial and temporal content of the coherent structures.

4.1 Moderate Mach Number Flow Configuration

The moderate Mach number flow configuration refers to the simulation database at $M_\infty = 0.4$ whereby the acoustic scattering analysis presented in Fig. 4.1(a) is computed. It is related to a similar case described in Section 3.3. The grid configuration is not changed, the setup is changed in the Mach number applied, from $M_\infty = 0.115$ to $M_\infty = 0.4$. The time discretization is altered to non-dimensional time step $\Delta t = 0.005$ in order to correctly capture the aeroacoustic sources in the turbulent field. The number of frames is greater than the low-Mach number configuration, however, due to the refined time step, the dimensionless total simulation time is 5.125.

Running a POD analysis, at first not considering the homogeneous spanwise direction, the computed singular values (λ) resulted in the POD spectrum presented in Fig. 4.2. One may notice that the p-3D norm gathers almost all the information in the first POD mode.

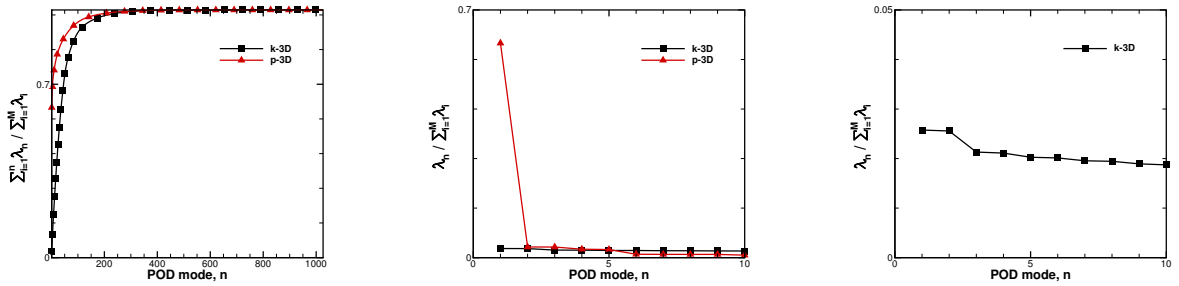

(a) Accumulative singular values. (b) Normalized singular values. (c) k-3D norm close view.

Figure 4.2: Singular values for k-3D and p-3D norms normalized by the sum of singular values presented in (a) single and (b) accumulative representation. (c) presents a close view of k-3D norm.

As shown in Fig. 4.1(a), the present flow configuration has a tonal peak noise at $kc = 27$. The influence of other frequency ranges in the acoustic scattering is smaller. This may be related to the fact that the p-3D norm did not spread the energy along the POD spectrum. In Fig. 4.2 it is possible to see the differences in the correlation matrix when the k-3D norm is applied. The pressure based norm correlation matrix does

not decay completely to zero. Which means that the time frames are not completely uncorrelated. Turbulent flows always present coherent structures, however the temporal and spatial correlation in turbulence decays to zero, due to the dissipation present in real flows.

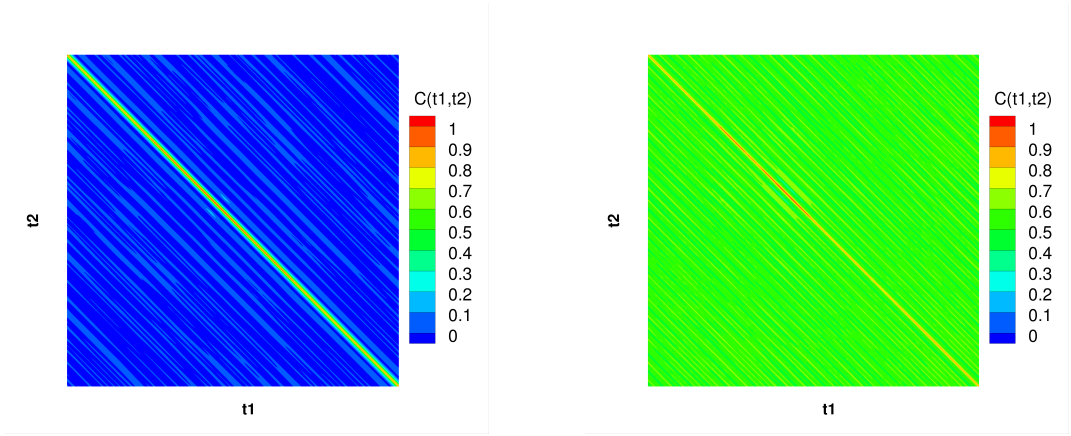

(a) k-3D norm. (b) p-3D norm.

Figure 4.3: Covariance matrix computed for present flow configuration using k-3D and p-3D POD norms without spectral filtering.

Well-correlated information is associated to acoustic propagation in the computational domain. Figure 3.20(c) shows the presence of correlated information in the matrix when the p-acoustic norm is used. The presence of correlated information along the correlation matrix in p-3D norm shows the importance of the acoustic propagation in the domain compared to the pressure fluctuations near the solid body computed in the turbulent flow.

As a result, the p-3D norm does not present a coupled 1st pair of POD modes formed by the POD modes λ_1 and λ_2, but formed by the λ_2 and λ_3. Figure 4.4 shows the spectral content of the POD modes computed in k-3D and p-3D POD norms. Now, the SPOD is applied to perform a enhanced analysis of the POD modes, using a similar window size $N_f = 400$ applied in previous analysis as it shows good results in Section 3.6.2 using a periodic time series assumption and a gaussian window type for the flow configuration presented in Section 3.3. The spectral content of the 1st POD mode λ_1 using the p-3D norm is presented, which differs from the tonal noise range, but contains information related to low-frequency range.

As shown in Fig. 4.4(b), only the 2nd mode pair, represented by λ_5 captures the tonal noise shown in Fig. 4.1(a). The k-3D norm is closely related to the results obtained in Section 3.6.2. The k-3D norm captures the tonal noise at $kc = 27$ in the 1st mode pair and low-frequency information at the subsequent POD mode pairs, as shown in Fig. 4.4(a).

It is important to notice in the 1st POD mode pair the spectral content captures the tonal noise information and contains a small peak at high frequency $kc \approx 70$. This shows that the most energy containing POD modes gathers the information of high frequencies

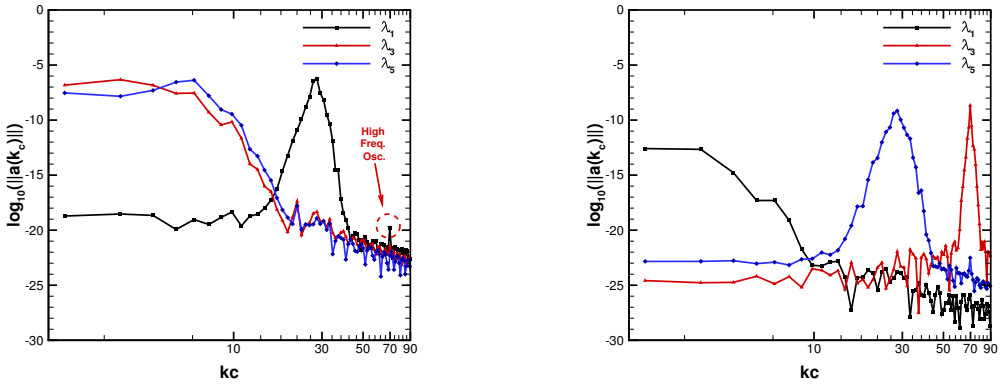

(a) k-3D norm.

(b) p-3D norm.

Figure 4.4: Spectral content for the 3 most energy containing POD mode pairs using periodic time series assumption and spectral POD with gaussian window filtering $N_f = 400$.

as well in a frequency range that is not even present in the acoustic analysis shown in Fig. 4.1(a).

As the flow presents an translational symmetry in spanwise direction, the flow can be decomposed in Fourier modes. The singular values for each POD norm is presented in Fig. 4.5, normalized by the sum of singular values for the mean Fourier mode z^0.

The POD spectrum is well distributed for the k-3D norm, however, the p-3D norm is poorly represented, in the same way as occurs for the general implementation presented in Fig. 4.2(b) when the homogeneous direction is not considered for POD analysis. Again, as presented in Section 3.8, the coupling between Fourier modes in spanwise direction and spectral filtering in the correlation matrix using Fourier-SPOD enhances the coupling between POD modes and the identification of temporal and spatial information related to coherent structures.

As show in Fig. 4.6(a), the spectral content for Fourier mode z^0 captures the tonal noise information, but the most energy containing POD mode, λ_1^0 is related to low-frequency information, as well as the most energy containing POD mode in the general implementation, computed without considering the translational symmetry in spanwise direction.

Figure 4.6(b) and (c) presents spectral content for Fourier modes z^1 and z^2, respectively. Fourier mode z^1 presents information at high-frequency range for the most energy containing mode pair, while the 2nd and 3rd POD mode pairs represented by λ_3^1 and λ_5^1 are related to the tonal noise. The spectrum is different for Fourier mode z^2, when tonal noise range is captured mainly by the 3rd mode pair, λ_5^2 and λ_6^2. This shows how the spectral content is not clearly defined for p-3D norm. For this reason, k-3D norm will be used for analysis of the present flow configuration, due to better results in POD

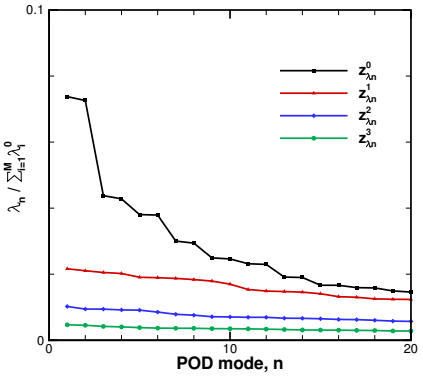

(a) k-3D norm; non-filtered.

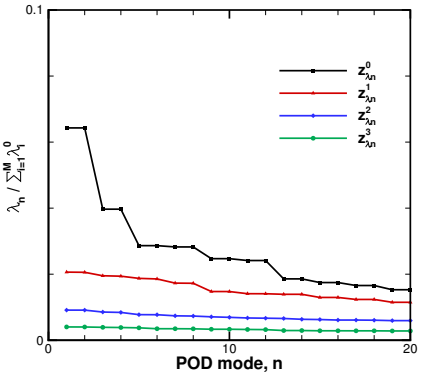

(b) k-3D norm; filtered.

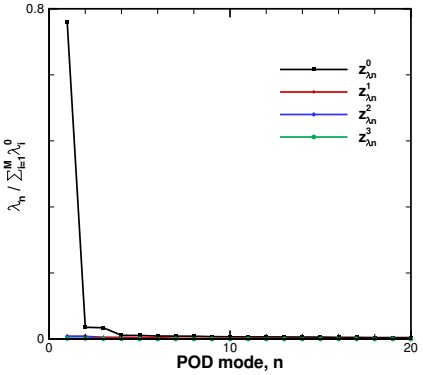

(c) p-3D norm; non-filtered.

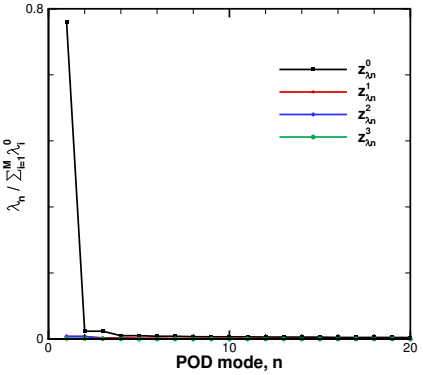

(d) p-3D norm; filtered.

Figure 4.5: Singular values normalized by the sum of singular values for z^0 with and without periodic time series assumption applied to spectral POD filtering with gaussian window with $N_f = 400$.

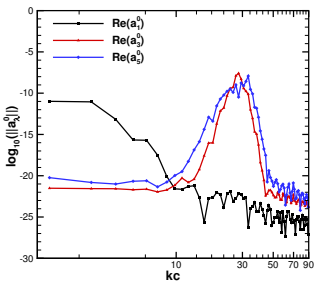

(a) Fourier mode z^0.

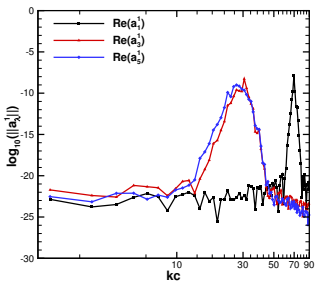

(b) Fourier mode z^1.

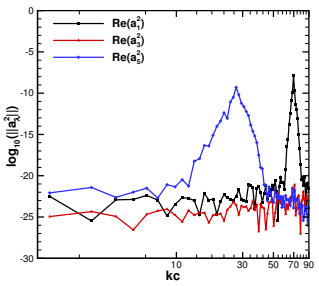

(c) Fourier mode z^2.

Figure 4.6: Spectral content POD modes a_1, a_3 and a_5 for the first 3 spanwise Fourier modes z^0, z^1 and z^2 using p-3D POD norm and periodic time series assumption and spectral POD with gaussian window filtering $N_f = 400$.

spectrum and spectral content, as shown in Fig. 4.7.

Figure 4.7 shows how the spectral content for the z^0, z^1 and z^2 in the 3 most energy

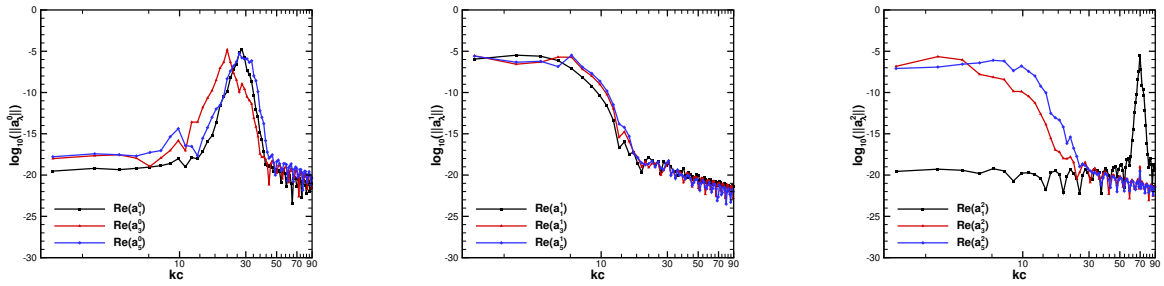

(a) Fourier mode z^0. (b) Fourier mode z^1. (c) Fourier mode z^2.

Figure 4.7: Spectral content POD modes a_1, a_3 and a_5 for the first 3 spanwise Fourier modes z^0, z^1 and z^2 using k-3D POD norm and periodic time series assumption and spectral POD with gaussian window filtering $N_f = 400$.

containing POD mode pairs. Similar to the results obtained in Section 3.8, as shown in Fig. 4.7(a), the first Fourier mode z^0 contains mainly the spectral content related to the tonal noise of the flow configuration presented in Fig. 4.1(a). The Fourier mode z^1 contains information related to oscillations in coherent structures at low-frequency range. Similar behavior is observed in Fig. 3.63, which shows the spectral content for the low Mach number flow configuration presented in Section 3.3.

Nevertheless, for the present flow configuration, as shown in Fig. 4.7(c), the most energy containing mode, λ_1^2 in Fourier mode z^2. The frequency is associated to the wavenumber $kc \approx 70$ which is captured in the POD analysis presented in fig. 4.4(a) for the POD mode pair represented by λ_1. This shows that coherent structures containing a considerable part of the turbulence energy also oscillate in spanwise direction, not being consisted only of structures from Fourier mode z^0.

Figure 4.8 shows that spatial wavenumbers z^4, z^5 and z^6 also have similar behavior presented in Fig. 4.7(c). The spectral content related to the most energy containing mode pairs, λ_1^n and λ_2^n, for these Fourier modes is related to the small peak at $kc \approx 70$ presented in the spectral content for the most energy containing mode pair in Fig. 4.4(a), when homogeneous flow direction is not considered. Despite of the modes λ_1^n being the ones with more energy for these Fourier modes, the energy of the flow they contain is already small. Because they contain little portion of the total turbulence energy of the flow, they appear as a small peak in Fig. 4.4(a) for λ_1 for a full 3D POD.

The spatial characterization of the coherent structures, analyzing the structures formed in spatial eigenfunctions for each POD mode, shows similar results to the ones obtained in Section 3.8 for the k-3D POD norm, as shown in Figs. 4.9, 4.10 and 4.11.

The structures for Fourier mode z^0 shows large coherent structures formed after the forced turbulent transition in the suction side. The elongated structures for POD modes λ_1, λ_3 and λ_5 have approximately the same size, which relates to the spectral content of

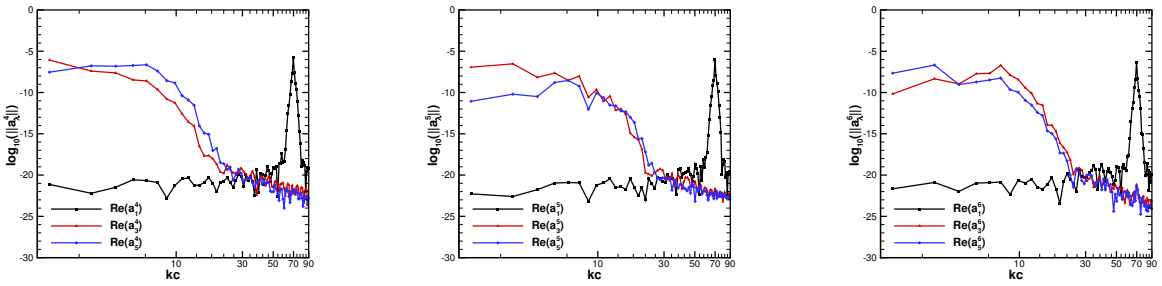

(a) z^4. (b) z^5. (c) z^6.

Figure 4.8: Spectral content POD modes a_1, a_3 and a_5 for the spanwise Fourier modes z^4, z^5 and z^6 using k-3D POD norm and periodic time series assumption and spectral POD with gaussian window filtering $N_f = 400$.

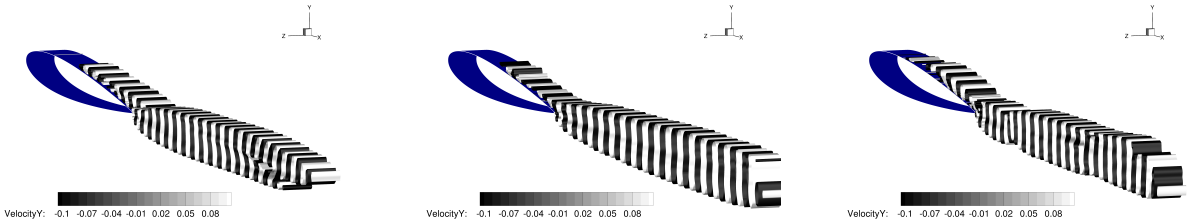

(a) Eigenfunction for λ_1^0. (b) Eigenfunction for λ_3^0. (c) Eigenfunction for λ_5^0.

Figure 4.9: Spatial Eigenfunction for 3 most energy containing POD mode pairs and spanwise Fourier mode z^0 using k-3D POD norm and periodic time series assumption and spectral POD with gaussian window filtering $N_f = 400$.

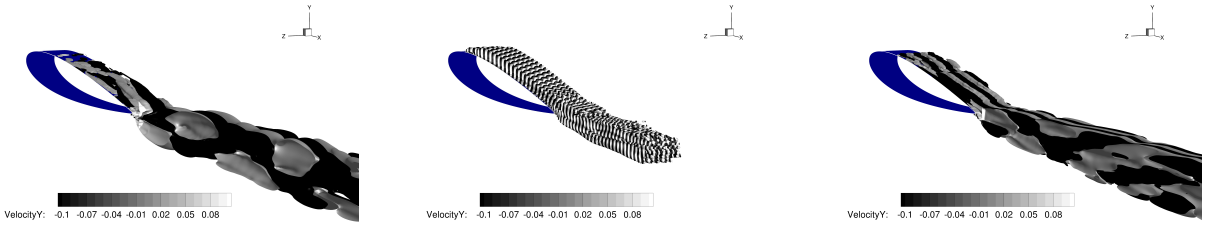

(a) Eigenfunction for λ_1^1. (b) Eigenfunction for λ_1^2. (c) Eigenfunction for λ_3^2.

Figure 4.10: Spatial Eigenfunction for z^1 and z^2 using k-3D POD norm and periodic time series assumption and spectral POD with gaussian window filtering $N_f = 400$.

these structures, shown in Fig. 4.7(a). These coherent structures are the main portion of the tonal noise peak analyzed in acoustic scattering in Fig. 4.1(a).

Figure 4.10 plots the difference between the spatial eigenfunctions that capture low and high frequency information in the k-3D POD norm. POD modes that capture low frequency coherent structures are present in Fig. 4.10(a) and (c). These coherent structures are associated to a frequency band that is not well captured in the acoustic analysis, but the turbulent structures are resolved in the flow and are captured in the POD analysis. The high frequency coherent structures, associated to oscillations at $kc \approx 70$ are associated to the spatial coherent structures shown in Fig. 4.10(b).

Figure 4.11 shows the development of the coherent structures captured in Fourier

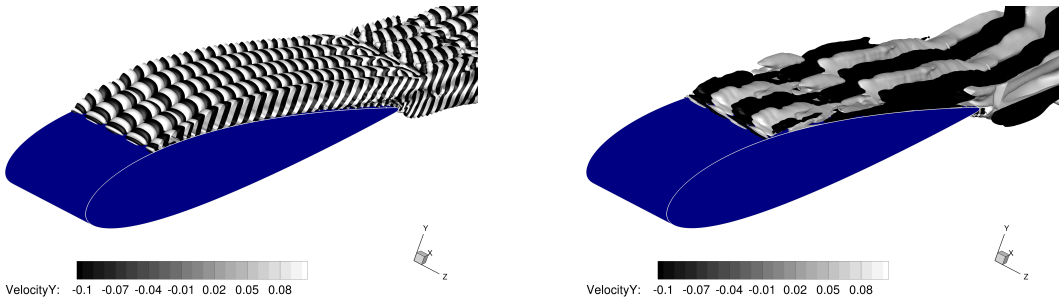

(a) Eigenfunction for λ_1^2.

(b) Eigenfunction for λ_3^2.

Figure 4.11: Closer view on the suction side for spatial eigenfunctions for z^2 using k-3D POD norm and periodic time series assumption and spectral POD with gaussian window filtering $N_f = 400$.

mode z^2 for POD modes λ_1^2 and λ_3^2. The high frequency coherent structures are diagonally aligned and the low-frequency coherent structures are aligned with the airfoil chord in the suction side.

One may notice that the coherent structures are not very different from the ones studied at low Mach number flow configuration. The physics of the coherent structures is not very different in spatial characterization, however, they do behave differently in temporal modes. The increase in the number of frames did not enhanced the analysis in low-frequency eddies, maybe a wider window for temporal simulation data would be necessary to generate better defined global modes in low frequency range.

The major difference to be pointed is the maintained correlation of the matrix for p-3D norm, closely related to p-acoustic norm used for low Mach number analysis. As the numerical data has a tonal peak at $kc = 27$, the acoustic propagation is said to play an important role in the correlation matrix computation. In this way, the pressure oscillations are not uncorrelated in the acoustic field and influence negatively the p-3D norm for POD analysis.

4.2 Zero AoA Flow Configuration

The present flow configuration is analyzed in acoustic scattering in Fig. 4.1(b). The case is set at $M_\infty = 0.115$, at 0 degs. angle of attack (AoA). The suction-blowing technique is used to force transition to turbulence in suction and pressure sides. As a result, the interaction between laminar and turbulent boundary layers presented in the previous cases does not occur in the present one. Near the trailing edge, an interaction between suction side and pressure side turbulent boundary layers is formed. Thus, the elongated turbulent structures formed in the previous cases, responsible for the tonal noise captured in the acoustic scattering, are broken and dissipated near the trailing edge. This results

in a broadband noise scattered along the sound spectra, as analyzed in the experiments performed by Brooks *et. al* (1989). Time discretization is maintained as dimensionless $\Delta t = 0.02$ along a total simulation time equal to 15.98.

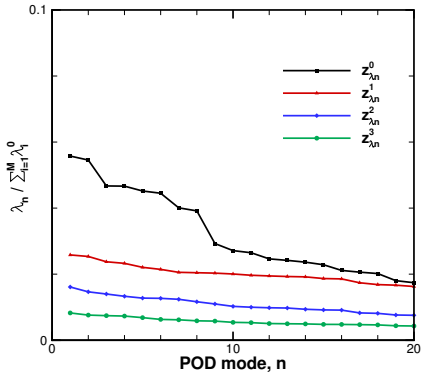

(a) k-3D norm; non-filtered.

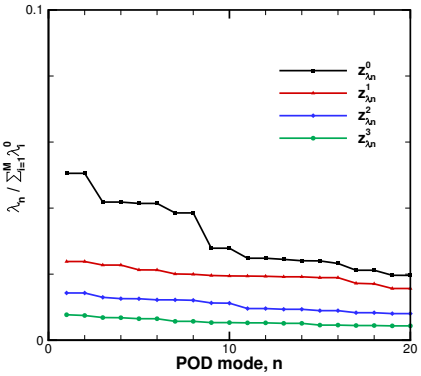

(b) k-3D norm; filtered.

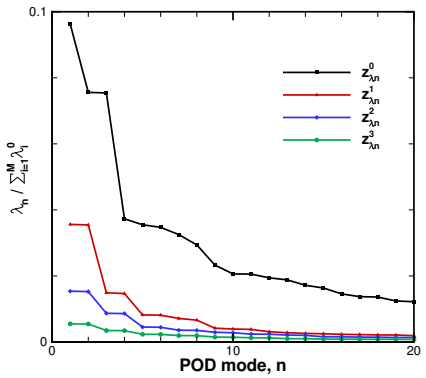

(c) p-3D norm; non-filtered.

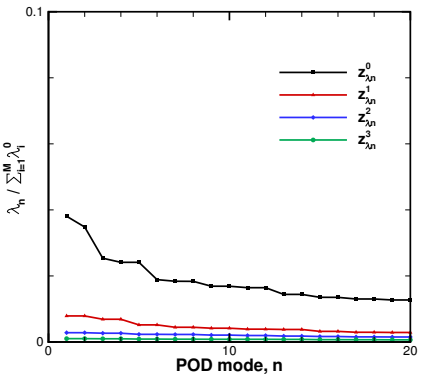

(d) p-3D norm; filtered.

Figure 4.12: Singular values normalized by the sum of singular values for z^0 with and without periodic time series assumption applied to spectral POD filtering with gaussian window with $N_f = 400$.

In order to correctly compute and capture the aeroacoustic sources for this case, the grid is refined near the airfoil in both suction and pressure sides. The structured body-fitted O-grid contains $1536 \times 125 \times 128$ grid points and the background grid contains $896 \times 511 \times 64$ grid points.

It is a low Mach number configuration at 0 degs. AoA. The flow has translational symmetry along the spanwise direction. Only the Fourier-POD will be used in this analysis. A combined Fourier-SPOD with gaussian type filtering using window size $N_f = 400$, which, in this case, corresponds to half the number of snapshots is used for temporal and spatial characterization of the turbulent flow.

Figure 4.12 shows the POD spectrum for the present numerical data normalized by the sum of singular values in the POD spectrum fo Fourier mode z^0. Once again, the spectral filtering enhances the mode coupling flattering the POD spectrum. For the k-3D POD norm the results are good without spectral filtering, even so an improvement can be perceived using spectral filtering as shown in Fig. 4.12(b). The p-3D POD norm once again does not present good results, specially for the Fourier mode z^0 that gathers the largest part of the energy. Without the spectral filtering, the first POD singular value for z^0 is decoupled and gathers a large amount of the turbulent energy of the flow. Using the spectral filtering, the results are improved, however, the first pair is not well coupled and the first pair is represented by λ_4^0 and λ_5^0, as shown in Fig. 4.12(d). For the subsequent Fourier modes, the coupling is achieved using the spectral filtering with $N_f = 400$. Due to the improvements obtained, the spectral filtering with gaussian type filtering and window size of $N_f = 400$ will be used in the following analysis.

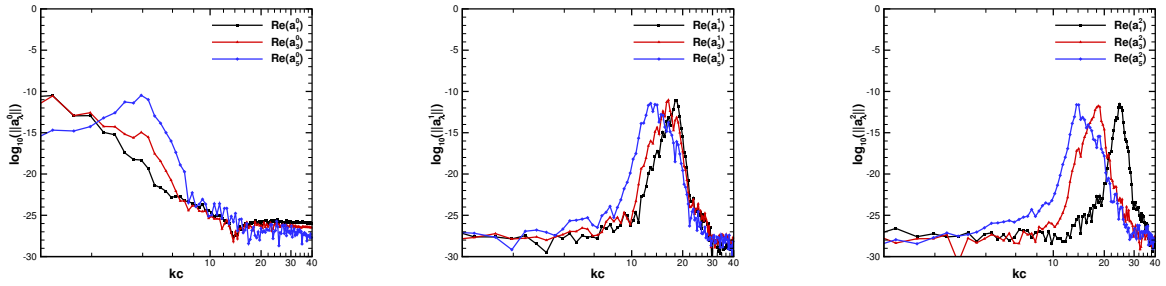

(a) z^0. (b) z^1. (c) z^2.

Figure 4.13: Spectral content POD modes a_1, a_3 and a_5 for the first 3 spanwise Fourier modes z^0, z^1 and z^2 using p-3D POD norm and periodic time series assumption and spectral POD with gaussian window filtering $N_f = 400$.

As the acoustic scattering of the present flow does not present a tonal noise as the previous cases, the spectral content of the flow is dominated by a broadband noise. The p-3D norm presents results for low-frequency content at the Fourier mode z^0, as shown in Fig. 4.13(a). The first coupled mode is represented by the spectral content of the POD mode λ_5^0. The following Fourier modes z^1 and z^2 gather information at high frequency range. This behavior is shown in p-3D norm in other flow configurations.

The spatial characterization of the turbulent structures is presented in Fig. 4.14. As shown in Fig. 4.14(a) and (b), the eddies are distorted as a result from the non-coupling in the POD spectrum. Figure 4.14(c) shows the behavior of the spanwise mean modes. The suction and pressure side structures are mixed in the trailing edge. Growth and decay behavior is formed as the coherent structures split and merge in the turbulent wake.

As shown in Figs. 4.14(d) to (i) the coherent structures captured by the p-3D norm are high frequency eddies. The spatial characteristics of these eddies is very similar. They

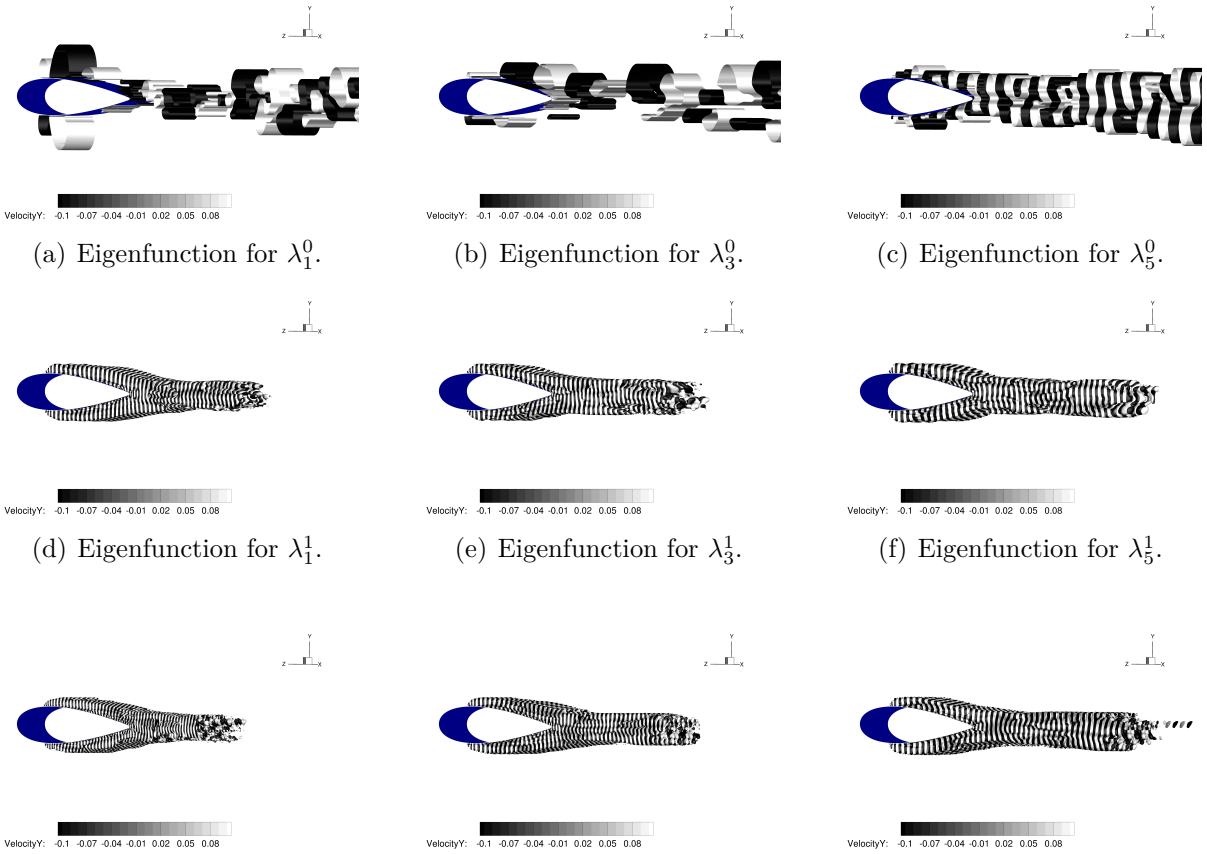

(a) Eigenfunction for λ_1^0. (b) Eigenfunction for λ_3^0. (c) Eigenfunction for λ_5^0.

(d) Eigenfunction for λ_1^1. (e) Eigenfunction for λ_3^1. (f) Eigenfunction for λ_5^1.

(g) Eigenfunction for λ_1^2. (h) Eigenfunction for λ_3^2. (i) Eigenfunction for λ_5^2.

Figure 4.14: Spatial Eigenfunction for 3 most energy containing POD mode pairs and spanwise Fourier modes z^0, z^1 and z^2 using p-3D POD norm and periodic time series assumption and spectral POD with gaussian window filtering $N_f = 400$.

are an important part of the spectral content of the flow that is gathered using the p-3D norm.

The p-3D norm is able to capture coherent structures at high frequency range in Fourier modes different from z^0. For the spanwise mean mode, the POD spectrum is not clearly defined, generating non-coupled modes and making it difficult to understand the behavior of low-to-moderate frequency range in the global modes.

For the k-3D POD norm, a similar behavior to what is present in the previous cases at 5 degs. AoA is obtained. The global modes are mainly dominated by low-to-moderate frequency range at the Fourier modes z^0, z^1 and z^2, as shown in Fig. 4.15. Similarly to what is analyzed in p-3D norm, in Fig. 4.13(a), the spanwise mean mode z^0 in the k-3D norm contains a spectral energy from $kc = 2$ to $kc = 6$, as shown in Fig. 4.15(a). The frequency related to this range is characterized as the range containing most of the energy of the present fluid flow.

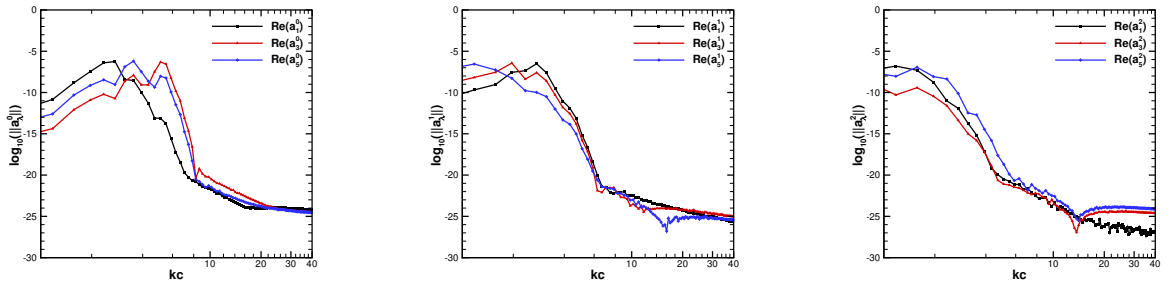

(a) z^0. (b) z^1. (c) z^2.

Figure 4.15: Spectral content POD modes a_1, a_3 and a_5 for the first 3 spanwise Fourier modes z^0, z^1 and z^2 using k-3D POD norm and periodic time series assumption and spectral POD with gaussian window filtering $N_f = 400$.

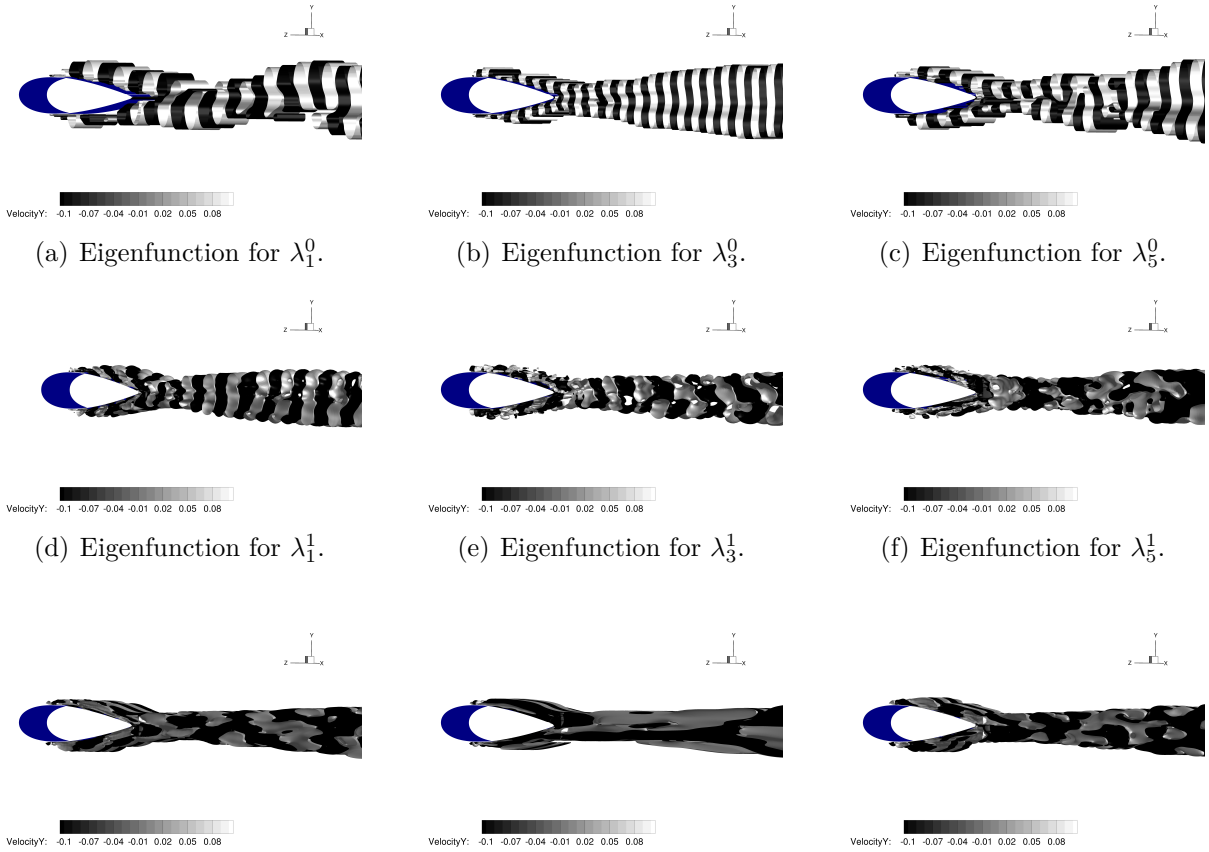

(a) Eigenfunction for λ_1^0. (b) Eigenfunction for λ_3^0. (c) Eigenfunction for λ_5^0.

(d) Eigenfunction for λ_1^1. (e) Eigenfunction for λ_3^1. (f) Eigenfunction for λ_5^1.

(g) Eigenfunction for λ_1^2. (h) Eigenfunction for λ_3^2. (i) Eigenfunction for λ_5^2.

Figure 4.16: Spatial Eigenfunction for 3 most energy containing POD mode pairs and spanwise Fourier modes z^0, z^1 and z^2 using k-3D POD norm and periodic time series assumption and spectral POD with gaussian window filtering $N_f = 400$.

Fourier modes z^1 and z^2 contain spectral energy at low frequencies. As the energy present in the singular values for the 2nd and 3rd mode pairs, the coherent structures captured in the fluid flow region are distorted. The most energy containing POD modes,

presented in Figs. 4.16(d) and (g) are well captured and show the presence of large diagonal structures interacting in the turbulent boundary layer region.

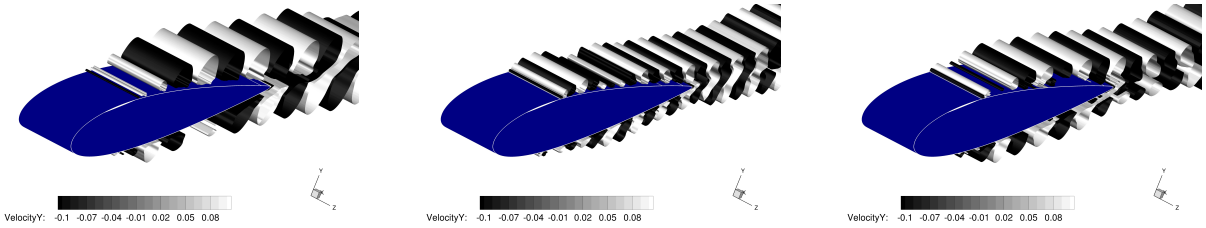

(a) Eigenfunction for λ_1^0. (b) Eigenfunction for λ_3^0. (c) Eigenfunction for $\lambda_5^0 X$.

Figure 4.17: Closer view on the suction side for spatial eigenfunctions for z^0 using k-3D POD norm and periodic time series assumption and spectral POD with gaussian window filtering $N_f = 400$.

Figure 4.17 presents a closer view of the spanwise mean coherent structures, showing the interaction between suction and pressure sides boundary layers. Larger structures are shown in Fig. 4.17(a), presenting spatial eddies rolling over each other until they merge in the turbulent wake.

Smaller coherent structures are present in Fig. 4.17(b) and (c), which are also splitted by the solid body and merging after the flow passes through the trailing edge. This behavior shows that the interaction between turbulent boundary layers in the present case is not only destructive and dissipative but also creates large eddies correlated in spanwise direction at the wake region.

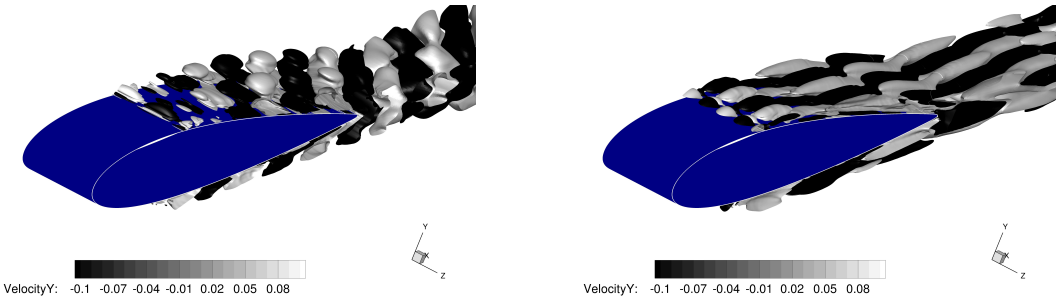

(a) Eigenfunction for λ_1^1. (b) Eigenfunction for λ_1^2.

Figure 4.18: Closer view on the suction side for spatial eigenfunctions for z^1 and z^2 POD modes λ_1 using k-3D POD norm and periodic time series assumption and spectral POD with gaussian window filtering $N_f = 400$.

Figure 4.18 show the spatial behavior of the structures which spectral content is presented in Figs. 4.15(b) and (c). The eddies characterized by the Fourier mode z^1 are diagonally aligned and contain a low frequency range spectral content. Small structures are also detached from the boundary layer and merge over the flow after passing the trailing edge. The structures are well characterized and contain a spatial behavior similar to what is observed in the low Mach number case at 5 degs. AoA for Fourier modes z^1

using the p-3D norm in Fig. 3.67. The difference, as stated, is the spectral content of the global modes being composed of low-frequency range energy, resulting in larger and thicker coherent structures.

The presence of these large diagonal coherent structures for the flow at 0 degs. AoA can be related to the weaker pressure gradient caused by the airfoil curvature at 0 degs. AoA. At 5 degs. AoA the airfoil curvature and the AoA combine to generate a stronger pressure gradient, as shown by the mean flow in Fig. 4.19(a). The stronger pressure gradient generates a higher local Reynolds number. As a result, in the adverse pressure gradient, the flow at 5 degs. AoA contains smaller coherent structures at high frequencies containing a considerable energy. At 0 degs. AoA the pressure gradient is weaker in the suction side, due only to the airfoil curvature, as shown in Fig. 4.19(b). As a result, local Reynolds number flow in the adverse pressure gradient is low, generating larger coherent structures.

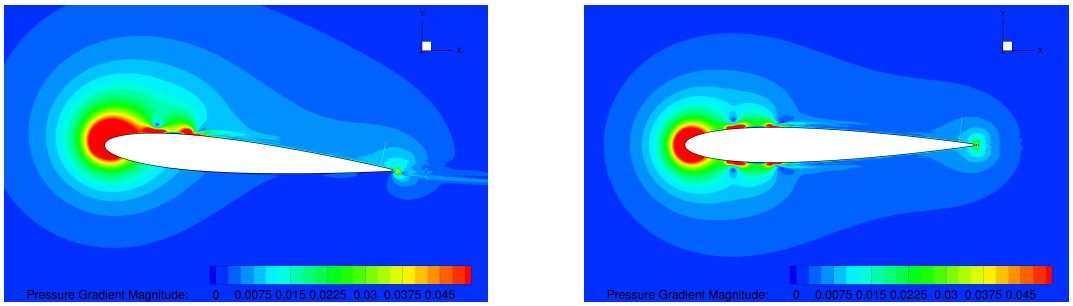

(a) 5 degs. AoA. (b) 0 degs. AoA.

Figure 4.19: Gradient pressure magnitude for the mean flow for the two different numerical databases at low Mach number $M_\infty = 0.115$ configuration.

The coherent structures for z^2 presented in Fig. 4.18(b) are similar to coherent structures obtained in cases with 5 degs. AoA for Fourier mode z^2, as shown in Figs. 3.64 and 4.11(b). These eddies are aligned with the stream and perpendicular to the trailing edge, so they have low-efficiency in noise propagation. It is proved by the spectral content of the POD modes for Fourier mode z^2 that oscillate at $kc \leq 2$, a low-frequency behavior that is not well-captured in the acoustic scattering analysis.

5 Final Remarks

Proper orthogonal decomposition is used to identify coherent structures in turbulent flows past a NACA0012 airfoil at different conditions. The turbulent flow is obtained by compressible large eddy simulation of the NACA0012 airfoil at 0 and 5 degs. angle of attack for Mach numbers $M_\infty = 0.1$ and 0.4 at Reynolds number $Re_c = 408000$ based on the airfoil chord. For the 5 degs. angle of attack numerical simulations, a turbulent boundary layer develops along the suction side of the airfoil due to boundary layer tripping and, in the pressure side, a laminar boundary layer develops due to the favorable pressure gradient. Previous work has shown that the current flow configuration leads to noise generation at a narrowband tonal peak associated to spanwise coherent structures. For the 0 degs. angle of attack case, turbulent boundary layers are formed in suction and pressure sides due to boundary layer tripping. The interaction between the turbulent boundary layers dissipates the tonal noise presented in the 5 degs. angle of attack cases. As a result, a broad band tonal noise is formed. An investigation of the coherent structures formed in the present wall-bounded turbulent cases is provided via an analysis of different POD techniques including a fully three-dimensional implementation of the standard snapshot method, the recently proposed spectral POD method (SPOD) and the combination of Fourier decomposition and SPOD.

5.1 Proper Orthogonal Decomposition Techniques

A POD analysis of the low Mach number 5 degs. angle of attack case is presented for different vector norms in the construction of the correlation matrix. Both kinetic energy and pressure norms tested are able to couple the first pair of POD modes which are related to coherent structures responsible for the airfoil tonal noise generation. However, higher order modes are uncoupled making it difficult to distinguish further coherent structures. For these higher POD modes, the kinetic energy norm tends to reconstruct low-frequency structures in the flow field while the pressure norm reconstructs high-frequency structures. This distinction is associated to the physical behavior of low-frequency large scale structures propagating in the streamwise direction and pressure oscillations that dissipate faster downstream the trailing edge, resulting in moderate to high-frequency fluctuations.

The SPOD method presents a better coupling of the modes, redistributing the energy

among the POD spectrum and leading to an improved identification of coherent structures. Square box and Gaussian filters are applied to the correlation matrix assuming periodical and non-periodical temporal signals. The application of the Gaussian filter allows an enhanced control in the response of the SPOD when compared to the square box filter. The assumption of periodic temporal signals in the construction of the correlation matrix provides a considerable improvement in the coupling of POD modes. In this case, phase diagrams show that low-frequency coherent structures obtained by the kinetic energy norm become coupled when temporal signal periodicity is enforced. The SPOD method is also able to improve the phase correlation of already coupled modes. The SPOD technique presents the best results in terms of mode coupling when employed together with the pressure norm. In this case, it is able to provide well resolved spatial eigenfunctions even for high-frequency structures. Spectra of the temporal modes obtained by the SPOD show that the filtering operation is able to reduce noise, focusing on energetic coherent structures at specific narrowband frequencies.

The combination of Fourier decomposition along the airfoil span and the spectral POD method allows a clear identification of coherent structures for the specific Fourier modes. The spectral content of the POD modes has a characteristic behavior for each Fourier mode in the kinetic energy norm. The pressure norm presents modes with more than one narrowband dominant frequency. Both norms recover the most energetic two-dimensional coherent structures associated to Fourier mode zero. The kinetic energy norm is able to identify large turbulent structures aligned with the airfoil chord. On the other hand, results obtained by the pressure norm show smaller scale turbulent structures diagonally aligned with the airfoil span. For the Fourier POD method, the SPOD also shows a considerable improvement in the identification of tonal narrowband and high-frequency coherent structures, especially when the correlation matrix is computed using a pressure norm. The filtering reduces the noise contained in the POD modes and results in enhanced spatial characterization of coherent structures in the eigenfunctions and also an improved identification of the spectral content related to them.

5.2 Coherent Structures in Turbulent Flows Past a NACA0012 Airfoil

The low Mach number case at 5 degs. angle of attack presented large coherent structures aligned with span, oscillating at the tonal range of frequencies characterized by the wavenumber $kc \approx 9$. Passing through the forced tripping to turbulence, on the suction side of the airfoil, streamwise aligned coherent structures are perceived by the

kinetic energy norm in spanwise Fourier modes z^1 and z^2. These coherent structures are captured by POD eigenfunctions at low frequencies, where the acoustic scattering analysis did not perform well due to the necessity to improve results below $kc = 5$ in the numerical simulations. Also, streamwise aligned coherent structures do not propagate efficiently as sound, as they are perpendicular to the trailing edge.

For the pressure norm, high frequency coherent structures are captured in the spanwise Fourier modes z^1 and z^2. These eddies are small and are spatially disposed diagonally along the suction side. The structures associated to these frequencies dissipate faster after passing through the trailing edge. The tonal noise range is mainly captured by the POD modes in spanwise Fourier mode z^0, which proves that correlated modes in the spanwise direction are responsible for the tonal noise presented in the acoustic scattering analysis.

For the moderate Mach number configuration at 5 degs. angle of attack, the tonal noise is shifted to higher frequencies, corresponding to $kc \approx 27$. The pressure norm performs poorly and the kinetic energy norm is used to analyze the coherent structures in the fluid flow. The small changes in the compressibility of the turbulent flow does not affect the characterization of the coherent structures and, as a result, the global modes are very similar to those obtained in the low Mach number configuration.

An investigation of the flow at 0 degs. angle of attack shows that the broadband noise is decomposed into small ranges of the spectral content analyzed via Fourier-SPOD modes. The span mean Fourier mode captures the most energetic coherent structures between $kc = 2$ and $kc = 6$. The kinetic energy norm captures low-frequency eddies with different behavior for the subsequent Fourier modes including global modes diagonally aligned for Fourier mode z^1 and streamwise aligned for Fourier mode z^2.

The diagonally aligned eddies captured in Fourier mode z^1 are larger and thicker than diagonal eddies captured in database from 5 degs. angle of attack. The eddies present in the spanwise Fourier mode z^2 are very similar to those obtained by the kinetic energy norm for the turbulent flow at 5 degs. angle of attack for the same Fourier mode. The coherent structures are equal on the suction and pressure sides. For the pressure norm, high frequency coherent structures are observed diagonally aligned with the flow and these coherent structures are very similar to the high frequency eddies observed for the low Mach number flow at 5 degs. angle of attack also using the pressure norm.

For all cases studied, the coherent structures formed by spanwise Fourier modes z^1 and z^2 increase and gain energy over the adverse pressure gradient on the airfoil. This shows that the pressure gradient formed by the airfoil curvature influences the formation of these larger coherent structures diagonally aligned with the flow for Fourier mode z^1 and aligned with the flow stream for Fourier mode z^2.

Flows at 5 degs. angle of attack present a stronger pressure gradient due to the

airfoil AoA. At $M_\infty = 0.4$, the pressure gradient is stronger, generating high frequency oscillations for spanwise Fourier modes z^1 and z^2 even for the kinetic energy norm. Such high frequency coherent oscillations are not present in the low Mach number case using the same POD norm. One may notice that, at 0 degs. angle of attack, the smaller eddies diagonally aligned with the flow increase in size. Due to the weaker adverse pressure gradient near the trailing edge the fluctuations contain less energy and the coherent eddies may increase in size. The same effect is perceived in turbulent flows at low Reynolds numbers which present larger coherent structures than moderate-to-high Reynolds number flows.

5.3 Future Work

The results obtained in the present work can be extended to different techniques of modal analysis. A dynamic mode decomposition (DMD) analysis could be performed in order to analyze the global instability of the present flow configurations. Such an analysis would also lead to results from the spectral content of the global modes.

As the database analyzed spans a similar parameter space for turbulent flows over a NACA0012 airfoil, a reduced order modeling (ROM) could be performed using the dataset present in the three simulations under the same parameter space using the POD-Galerkin or Petrov-Galerkin methods, or even new ROM-based techniques from advanced machine learning to perform fast analysis of the transient flow under these conditions and flow conditions between the parameter space defined by the LES database to generate new high-fidelity turbulence data. The knowledge generated under the stated parameter space could lead to the development of high-level techniques for flow control of turbulent flow over an airfoil.

Several modal analyses could be performed based on the high-fidelity database presented. This work also provides an insight on the POD modes generated for a general implementation of POD. As a results, the POD analysis here performed could be extended to computational domains where no translational symmetry is present, for example, for more complex geometries typical of aeronautical and mechanical engineering applications.

References

AHUJA, S. and ROWLEY, C.W. Feedback control of unstable steady states of flow past a flat plate using reduced-order estimators. **Journal of fluid mechanics**, vol. 645, 447–478, 2010.

ANDERSON, E.; BAI, Z.; BISCHOF, C.; BLACKFORD, L.S.; DEMMEL, J.; DONGARRA, J.; DU CROZ, J.; GREENBAUM, A.; HAMMARLING, S.; MCKENNEY, A. *et. al.* **LAPACK Users' guide**. SIAM, 1999.

ANDRIANNE, T.; LIGOT, J. and DIMIRIADIS, G. Proper orthogonal decomposition of unsteady aerodynamic flows. Research report, Department of Aerospace and Mechanical Engineering of University of Liege, Liège, Belgium, 2009.

ATWELL, J.A. and KING, B.B. Reduced order controllers for spatially distributed systems via prper orthogonal decomposition. **SIAM J. Sci. Comput.**, vol. 26, 128–151, 2004.

AUBRY, N.; HOLMES, P.; LUMLEY, J.L. and STONE, E. The dynamics of coherent structures in the wall region of a turbulent boundary layer. **Journal of Fluid Mechanics**, vol. 192, 115–173, 1988.

BACKES, B., **Sound Generation in Aerodynamic Flows with Wake Interaction**, Master Thesis, University of Campinas, Campinas, SP, Brazil, 2016.

BEAM, R.M. and WARMING, R.F. An implicit factored scheme for the compressible navier-stokes equations. **AIAA journal**, vol. 16, n. 4, 393–402, 1978.

BHASKARAN, R. and LELE, S.K. Large eddy simulation of free-stream turbulence effects on heat transfer to a high-pressure turbine cascade. **Journal of Turbulence**, , n. 11, N6, 2010.

BROOKS, T.F.; POPE, D.S. and MARCOLINI, M.A. Airfoil self-noise and prediction. Technical report, 1218 NASA Reference Publication, 1989.

BROWN, G.L. and ROSHKO, A. On density effects and large structure in turbulent mixing layers. **Journal of Fluid Mechanics**, vol. 64, n. 04, 775–816, 1974.

CAMPHOUSE, R.C.; MYATT, J.; SCHMIT, R.; GLAUSER, M.; AUSSEUR, J.; ANDINO, M. and WALLACE, R. A snapshot decomposition method for reduced order modeling and boundary feedback control. In **4th Flow control conference**, p. 4195. 2008.

CANTWELL, B. Organized motion in turbulent flow. **Ann. Rev. Fluid Mech**, vol. 13, 457–515, 1981.

COLONIUS, T. and TAIRA, K. A fast immersed boundary method using a nullspace approach and multi-domain far-field boundary conditions. **Computer Methods in Applied Mechanics and Engineering**, vol. 197, n. 25, 2131–2146, 2008.

CORDIER, L. and BERGMANN, M. Proper orthogonal decomposition: An overview. Technical report, Laboratoire d'Energétique et de Mécanique Théorique et Appliquée, Vandoeuvre-lès-Nancy, France, 2003.

CURLE, N. The influence of solid boundaries upon aerodynamic sound. **Proceedings of the Royal Society of London Series A**, vol. 231, 505–514, 1955.

DIAMESSIS, P.J.; GURKA, R. and LIBERZON, A. Spatial characterization of vortical structures and internal waves in a stratified turbulent wake using proper orthogonal decomposition. **Phys. of Fluids**, vol. 22, n. 8, 086601, 2010.

DOWELL, E.H.; HALL, K.C. and ROMANOWSKI, M.C. Eigenmode analysis in unsteady aerodynamics: Reduced order models. **Applied Mechanics Reviews**, vol. 50, n. 6, 371–385, 1998.

DRAZIN, P. On a model of instability of a slowly-varying flow. **Quarterly Journal of Mechanics and Applied Mathematics**, vol. 27, 69–86, 1974.

FFOWCS-WILLIAMS, J.E. and HALL, L.H. Aerodynamic sound generation by turbulent flow in the vicinity of a scattering half plane. **Journal of Fluid Mechanics**, vol. 40, n. 04, 657–670, 1970.

FFOWCS-WILLIAMS, J.E. and HAWKINGS, D.L. Sound generated by turbulence and surfaces in arbitrary motion. **Philosophical Transactions of the Royal Society of London Series A**, vol. 264, 321–342, 1969.

FREUND, J.B. Noise sources in a low-reynolds-number turbulent jet at mach 0.9. **Journal of Fluid Mechanics**, vol. 438, 277–305, 2001.

FREUND, J.B. and COLONIUS, T. Turbulence and sound-field pod analysis of a turbulent jet. **International Journal of Aeroacoustics**, vol. 8, n. 4, 337–354, 2009.

GOLUB, G.H. and VAN LOAN, C.F. **Matrix computations**, vol. 3. JHU Press, 2012.

GORDEYEV, S.; DE LUCCA, N.; JUMPER, E.J.; HIRD, K.; JULIANO, T.J.; GREGORY, J.W.; THORDAHL, J. and WITTICH, D.J. Comparison of unsteady pressure fields on turrets with different surface features using pressure-sensitive paint. **Experiments in fluids**, vol. 55, n. 1, 1661, 2014.

GORDEYEV, S.V. and THOMAS, F.O. A temporal proper decomposition (tpod) for closed-loop flow control. **Experiments in fluids**, vol. 54, n. 3, 1477, 2013.

GURKA, R.; LIBERZON, A. and HETSRONI, G. Pod of vorticity fields: A method for spatial characterization of coherent structures. **International Journal of Heat and Fluid Flow**, vol. 27, n. 3, 416–423, 2006.

HALL, K.C. Eigenanalysis of unsteady flows about airfoils, cascades, and wings. **AIAA Journal**, vol. 32, n. 12, 2426–2432, 1994.

HORN, R.A. and JOHNSON, C.R. **Matrix analysis**. Cambridge university press, 2012.

HUERRE, P. and MONKEWITZ, P.A. Local and global instabilities in spatially developing flows. **Ann. rev. of fluid mechanics**, vol. 22, n. 1, 473–537, 1990.

HUSSAIN, A.K.M.F. Coherent structures and studies of perturbed and unperturbed jets. **Lecure Notes in Physics**, vol. 136, 1980.

HUSSAIN, A.K.M.F. Coherent structures – reality and myth. **Phys. of Fluids**, vol. 26, 2816–2850, 1983.

HUSSAIN, A.K.M.F. Coherent structures and turbulence. **J. Fluid Mech.**, vol. 173, 303–356, 1986.

ILAK, M.; BAGHERI, S.; BRANDT, L.; ROWLEY, C.W. and HENNINGSON, D.S. Model reduction of the nonlinear complex ginzburg–landau equation. **SIAM Journal on Applied Dynamical Systems**, vol. 9, n. 4, 1284–1302, 2010.

ILAK, M. and ROWLEY, C.W. Modeling of transitional channel flow using balanced proper orthogonal decomposition. **Physics of Fluids**, vol. 20, n. 3, 2008.

JUANG, J.N. and PAPPA, R.S. An eigensystem realization algorithm for modal parameter identification and model reduction. **Journal of guidance, control, and dynamics**, vol. 8, n. 5, 620–627, 1985.

KOCHEEMOOLAYIL, J.G. and LELE, S.K. Wall modeled large eddy simulation of airfoil trailing edge noise. In **20th AIAA/CEAS Aeroacoustics Conference**, p. 3304. 2014.

KOCHEEMOOLAYIL, J.G. and LELE, S.K. Large eddy simulation of airfoil self-noise at high reynolds number. In **22nd AIAA/CEAS Aeroacoustics Conference**, p. 2919. 2016.

LALL, S.; MARSDEN, J.E. and GLAVAŠKI, S. A subspace approach to balanced truncation for model reduction of nonlinear control systems. **International journal of robust and nonlinear control**, vol. 12, n. 6, 519–535, 2002.

LELE, S.K. Compact finite difference schemes with spectral-like resolution. **Journal of computational physics**, vol. 103, n. 1, 16–42, 1992.

LELE, S.K. and NICHOLS, J.W. A second golden age of aeroacoustics? **Philosophical Transactions of the Royal Society of London A: Mathematical, Physical and Engineering Sciences**, vol. 372, n. 2022, 20130321, 2014.

LI, N. and LAIZET, S. 2decomp & fft-a highly scalable 2d decomposition library and fft interface. In **Cray User Group 2010 conference**, pp. 1–13. 2010.

LIBERZON, A.; GURKA, R. and HETSRONI, G. Comparison between two and three-dimensional pod in a turbulent boundary layer using multi-plane stereoscopic piv. In **Journal of Physics: Conference Series**, vol. 318, p. 022010. IOP Publishing, 2011.

LIBERZON, A.; GURKA, R.; TISELJ, I. and HETSRONI, G. Spatial characterization of the numerically simulated vorticity fields of a flow in a flume. **Theoretical and Computational Fluid Dynamics**, vol. 19, n. 2, 115–125, 2005.

LIGHTHILL, M.J. On sound generated aerodynamically, part 1: General theory. **Proceedings of the Royal Society of London Series A**, vol. 211, 564–587, 1952.

LOCKARD, D.P. An efficient, two-dimensional implementation of the ffowcs-williams and hawkings equation. **Journal of Sound and Vibration**, vol. 229, 897–911, 2000.

LOCKARD, D.P. and LILLEY, G.M. The airframe noise reduction challenge. Tech. report 213013, NASA Report, 2004.

LUMLEY, J.L. The structure of inhomogeneous turbulent flows. **Atmospheric turbulence and radio wave propagation**, pp. 166–178, 1967.

LUMLEY, J.L. **Stochastic Tools in Turbulence**. Academic Press, New York, 1970.

MASSAROTI, M. and WOLF, W. Comparison of experimental methods to measure the aeroacoustic noise of automotive roof crossbars. In **16th Brazilian Congress of Thermal Sciences and Engineering**. 2016.

MEZIĆ, I. Spectral properties of dynamical systems, model reduction and decompositions. **Nonlinear Dynamics**, vol. 41, n. 1, 309–325, 2005.

MEZIĆ, I. Analysis of fluid flows via spectral properties of the koopman operator. **Annual Review of Fluid Mechanics**, vol. 45, 357–378, 2013.

MIOTTO, R.F.; WOLF, W. and DE SANTANA, L.D. Numerical computation of gust aerodynamic response for realistic airfoils: Application of amiet's theory. In **22nd AIAA/CEAS Aeroacoustics Conference**, p. 2737. 2016.

NAGARAJAN, K.K.; CORDIER, L.; AIRIAU, C. and KOURTA, A. Pod based reduced order modelling of a compressible forced cavity flow. In **Proceedings of the 19th French Congress on Mechanics**. 2009.

NAGARAJAN, S.; LELE, S. and FERZIGER, J. Leading-edge effects in bypass transition. **Journal of Fluid Mechanics**, vol. 572, 471–504, 2007.

NAGARAJAN, S.; LELE, S.K. and FERZIGER, J.H. A robust high-order compact method for large eddy simulation. **Journal of Computational Physics**, vol. 191, n. 2, 392–419, 2003.

PODVIN, B. A proper-orthogonal-decomposition–based model for the wall layer of a turbulent channel flow. **Physics of Fluids**, vol. 21, n. 1, 015111, 2009.

PODVIN, B.; FRAIGNEAU, Y.; JOUANGUY, J. and LAVAL, J.P. On self-similarity in the inner wall layer of a turbulent channel flow. **Journal of Fluids Engineering**, vol. 132, n. 4, 041202, 2010.

PODVIN, B. and SERGENT, A. Proper orthogonal decomposition investigation of turbulent rayleigh-bénard convection in a rectangular cavity. **Physics of Fluids**, vol. 24, n. 10, 105106, 2012.

POPE, S.B. Turbulent flows. 2001.

ROWLEY, C.W., **Modeling, Simulation and Control of Cavity Flow Oscillations**, PhD Thesis, California Institute of Technology, 2002.

ROWLEY, C.W. Model reduction for fluids, using balanced proper orthogonal decomposition. **International Journal of Bifurcation and Chaos**, vol. 15, n. 03, 997–1013, 2005.

ROWLEY, C.W. and DAWSON, S.T. Model reduction for flow analysis and control. **Annual Review of Fluid Mechanics**, vol. 49, 387–417, 2017.

ROWLEY, C.W.; MEZIĆ, I.; BAGHERI, S.; SCHLATTER, P. and HENNINGSON, D.S. Spectral analysis of nonlinear flows. **Journal of fluid mechanics**, vol. 641, 115–127, 2009.

SAAD, Y. **Numerical methods for large eigenvalue problems**. Manchester University Press, 1992.

SCHMID, P.J. Dynamic mode decomposition of numerical and experimental data. **Journal of fluid mechanics**, vol. 656, 5–28, 2010.

SCHMID, P.J.; MEYER, K.E. and PUST, O. Dynamic mode decomposition and proper orthogonal decomposition of flow in a lid-driven cylindrical cavity. In **8th international symposium on particle image velocimetry-PIV09**, 3, pp. 1–4. 2009.

SCHMID, P.J. and SESTERHENN, J. Dynamic mode decomposition of numerical and experimental data. In **Bull. Am. Phys. Soc**, 53, p. 102. 2008.

SIEBER, M.; ; PASCHEREI, C.O. and OBERLEITHNER, K. Spectral proper orthogonal decomposition. **Journal of Fluid Mechanics**, vol. 792, 798–828, 2016.

SIROVICH, L. Turbulence and the dynamics of coherent structures. Part I: Coherent structures. **Quarterly of Applied Mathematics**, vol. 45, 561–571, 1986.

TAIRA, K. Proper orthogonal decomposition in fluid flow analysis: 1. **Introduction. Jpn. Soc. Fluid Mech. Nagare**, vol. 30, 115–123, 2011.

TAIRA, K. and COLONIUS, T. Three-dimensional flows around low-aspect-ratio flat-plate wings at low reynolds numbers. **Journal of Fluid Mechanics**, vol. 623, 187–207, 2009.

TREFETHEN, L.N. and BAU III, D. **Numerical linear algebra**, vol. 50. Siam, 1997.

TU, J.; ROWLEY, C.; ARAM, E. and MITTAL, R. Koopman spectral analysis of separated flow over a finite-thickness flat plate with elliptical leading edge. In **49th AIAA Aerospace Sciences Meeting including the New Horizons Forum and Aerospace Exposition**, p. 38. 2011.

TU, J.H.; ROWLEY, C.W.; LUCHTENBURG, D.M.; BRUNTON, S.L. and KUTZ, J.N. On dynamic mode decomposition: Theory and applications. **Journal of Computational Dynamics**, vol. 1, n. 2, 391–421, 2014.

WAGNER, C.; HÜTTL, T. and SAGAUT, P. **Large-eddy simulation for acoustics**, vol. 20. Cambridge University Press, 2007.

WANG, M. and MOIN, P. Computation of trailing-edge flow and noise using large-eddy simulation. **AIAA Journal**, vol. 38, n. 12, 2201–2209, 2000.

WOLF, W.R., **Airfoil Aeroacoustics, LES and Acoustic Analogy Predictions**, PhD Thesis, Stanford University, 2011.

WOLF, W.R.; AZEVEDO, J.L.F. and LELE, S.K. Convective effects and the role of quadrupole sources for aerofoil aeroacoustics. **Journal of Fluid Mechanics**, vol. 708, 502–538, 2012.

WOLF, W.R.; AZEVEDO, J.L.F. and LELE, S.K. Effects of mean flow convection, quadrupole sources and vortex shedding on airfoil overall sound pressure level. **Journal of Sound and Vibration**, vol. 332, 6905–6912, 2013.

WOLF, W.R.; KOCHEEMOOLAYIL, J.G. and LELE, S.K. Large eddy simulation of stall noise. In **20th AIAA/CEAS Aeroacoustics Conference**, p. 3182. 2014.

WRAY, A.A. Very low storage time-advancement schemes. **Internal Rep. NASA-Ames Research Center, Moffett Field, CA**, 1986.